Near-Optimal Control of Atomic Force Microscope For Non-contact Mode Applications

Joshua L. Sutton

Thesis submitted to the Faculty of the
Virginia Polytechnic Institute and State University
in partial fulfillment of the requirements for the degree of

Masters of Science
in
Computer Engineering

Almuatazbellah Boker, Chair
Lamine M. Mili
Thinh Doan

May 6, 2022
Blacksburg, Virginia

Keywords: Atomic Force Microscope, Optimal Control, Singular Perturbation.

Near-Optimal Control of Atomic Force Microscope For Non-contact Mode Applications

Joshua L. Sutton

(ABSTRACT)

A compact model representing the dynamics between piezoelectric voltage inputs and cantilever probe positioning, including nonlinear surface interaction forces, for atomic force microscopes (AFM) is considered. By considering a relatively large cantilever stiffness, singular perturbation methods reduce complexity in the model and allows for faster responses to Van der Waals interaction forces experienced by the cantilever's tip and measurement sample. In this study, we outline a nonlinear near-optimal feedback control approach for non-contact mode imaging designed to move the cantilever tip laterally about a desired trajectory and maintain the tip vertically about the equilibrium point of the attraction and repulsion forces. We also consider the universal instance when the tip-sample interaction force is unknown, and we construct cascaded high-gain observers to estimate these forces and multiple AFM dynamics for the purpose of output feedback control. Our proposed output feedback controller is used to accomplish the outlined control objective with only the piezotube position available for state feedback.

Near-Optimal Control of Atomic Force Microscope For Non-contact Mode Applications

Joshua L. Sutton

(GENERAL AUDIENCE ABSTRACT)

In this thesis, the idea of an atomic force microscope, specifically the applications of its non-contact mode, will be discussed. An atomic force microscope (AFM) is a tool that measures the surface height of nanometer sized samples. To improve the speed and precision of the machine under a non-contact mode objective, a controller is designed based on optimality and is applied to the system. The system contains a series of equations designed to steer the system towards a desired trajectory and minimal vibrations. Given the complexity of the system, resulting from nonlinearities, we will apply singular perturbation principles on the system's stiffness property to separate the larger problem into two smaller ones. These two problems are inserted into a near-optimal controller and a series of simulations are conducted to demonstrate performance. Alongside this, we will outline an observer to estimate the unknown dynamics of the system. These estimates are then applied to our controller to demonstrate that only the AFM's piezotube position is to be known in order to estimate and control the remaining dynamics of the system.

Dedication

This thesis is dedicated to the memory of my late mother, Karen Sutton. My pursuit for higher education was inspired by the potential she saw in me from the very beginning.

My father, Lee Sutton, for supporting me through the toughest of times.

My best friend, Michael Richardson, for having always been there for me.

And for my girlfriend, Nikita Vasudevan, for always believing in me and cheering me on.

Acknowledgments

I would like to thank my advisor, Dr. Almuatazbellah Boker, for guiding my research and providing assistance in the control design. Your insight helped make elements of this work possible, and I would like to thank you for continuously working with me through the challenging stages of this research.

I would also like to acknowledge our research partner from Memorial University, Dr. Mohammad Al Janaideh. His atomic force microscope knowledge provided constant reassurance on this research topic, and I would like to thank him graciously for his assistance on this work.

Lastly, I would like to thank my committee members Dr. Lamine M. Mili and Dr. Thinh Doan for supporting this work.

Contents

1 Introduction **1**

1.1 Background 1

1.2 Literature Review 4

1.2.1 AFM Control Review 4

1.2.2 Observer-based Control of AFM Review 6

1.3 Contributions and Outline 9

2 Problem Formulation **11**

2.1 Atomic Force Microscope (AFM) Dynamics 11

2.2 Nonlinear Van der Waals Force 14

2.3 Optimal Control Problem 15

2.4 Singular Perturbation Model 18

3 Linear Near-optimal Feedback Design **20**

3.1 Singular Perturbation Theory 20

3.2 Linear Singular Perturbation Model 21

3.3 Linear Near-optimal Control Design 23
3.3.1 Linear Slow Sub-problem 23
3.3.2 Linear Fast Sub-problem 25
3.3.3 Linear Composite Control 26
3.4 Linear Near-optimal Simulations 27

4 Nonlinear Near-optimal Feedback Design 36

4.1 Addressing Nonlinear Interaction Forces 36
4.2 Nonlinear Near-optimal Control Design 36
4.2.1 Nonlinear Slow Sub-problem 37
4.2.2 Nonlinear Fast Sub-problem 39
4.2.3 Nonlinear Composite Controller 40
4.3 Nonlinear Near-optimal Simulations 42
4.4 Linear, Nonlinear, and PD Controller Comparison 48

5 Nonlinear Observer Design 51

5.1 Cascaded Extended High-Gain Observers 51
5.2 Combined High-Gain Observer 54
5.2.1 Combined Observer Design 54
5.2.2 Output Feedback Control of Combined Observer 56
5.2.3 Combined Observer Simulations 57
5.3 Cascaded Extended High-Gain Observer 64

5.3.1 Cascaded Observer Design 64

5.3.2 Output Feedback Control of Cascaded Observer 67

5.3.3 Cascaded Observer Simulations 70

6 Conclusion **77**

Bibliography **77**

Appendices **85**

Appendix A Theorem 4.2.1 Verification **86**

A.1 A Note About Our Assumption Conditions 86

A.2 Assumption 7.1 87

A.3 Assumption 7.2 89

A.4 Assumption 7.3 92

A.5 Assumption 7.4 95

A.6 $\dot{V}_s < 0$: 99

Appendix B Theorem 4.2.2 Verification **101**

List of Figures

1.1 An NT-MDT Ntegra AFM 2

1.2 Non-contact AFM image of a human chromosome 3

1.3 General AFM tip measurement feedback control process 6

2.1 AFM scanner coordinate frame where (x_{tx}, x_{ty}, x_{tz}) and (x_{px}, x_{py}, x_{pz}) are the tip and piezotube dynamics respectively and z_b is the tip-sample interaction force equilibrium point 13

2.2 Van der Waals force curve highlighting the z_b equilibrium point 14

3.1 Linear near-optimal control x_{1t} performance 30

3.2 Linear near-optimal control x_{2t} performance 31

3.3 Linear near-optimal control x_{1p} performance 31

3.4 Linear near-optimal control x_{2p} performance 32

3.5 Linear near-optimal control z_1 performance 32

3.6 Linear near-optimal control z_2 performance 33

3.7 Linear near-optimal control e_1 performance 33

3.8 Linear near-optimal control e_2 performance 34

3.9 Linear near-optimal control u control effort 34

3.10 Interaction forces affecting the linear near-optimal controller 35

3.11 Linear near-optimal control e_1 performance across varying epsilons 35

4.1 Nonlinear near-optimal control x_{1t} performance 43

4.2 Nonlinear near-optimal control x_{2t} performance 44

4.3 Nonlinear near-optimal control x_{1p} performance 44

4.4 Nonlinear near-optimal control x_{2p} performance 45

4.5 Nonlinear near-optimal control z_1 performance 45

4.6 Nonlinear near-optimal control z_2 performance 46

4.7 Nonlinear near-optimal control e_1 performance 46

4.8 Nonlinear near-optimal control e_2 performance 47

4.9 Nonlinear near-optimal control u control effort 47

4.10 Interaction forces affecting the nonlinear near-optimal controller 48

4.11 Nonlinear near-optimal control e_1 performance across varying epsilon 48

4.12 Controller comparison evaluating x_{1t} performance 49

5.1 Combined observer output feedback control x_{1t} performance 58

5.2 Combined observer output feedback control x_{2t} performance 59

5.3 Combined observer output feedback control x_{1p} performance 59

5.4 Combined observer output feedback control x_{2p} performance 60

5.5 Combined observer output feedback control z_1 performance 60

5.6 Combined observer output feedback control z_2 performance 61

5.7 Combined observer output feedback control e_1 performance 61

5.8 Combined observer output feedback control e_2 performance 62

5.9 Combined observer output feedback control u control effort 62

5.10 Interaction forces affecting the nonlinear near-optimal controller 63

5.11 Combined observer output feedback control σ estimated disturbance 63

5.12 Closed-loop output feedback control system using cascade observer 66

5.13 Cascaded observer output feedback control x_{1t} performance 71

5.14 Cascaded observer output feedback control x_{2t} performance 71

5.15 Cascaded observer output feedback control x_{1p} performance 72

5.16 Cascaded observer output feedback control x_{2p} performance 72

5.17 Cascaded observer output feedback control z_1 performance 73

5.18 Cascaded observer output feedback control z_2 performance 73

5.19 Cascaded observer output feedback control e_1 performance 74

5.20 Cascaded observer output feedback control e_2 performance 74

5.21 Cascaded observer output feedback control u control effort 75

5.22 Interaction forces affecting the nonlinear near-optimal controller 75

5.23 Cascaded observer output feedback control σ_1 estimated x_{1t} position 76

5.24 Cascaded observer output feedback control σ_2 estimated disturbance 76

A.1 Simulated plot demonstrating positive-definite condition $A.1.3$ 88

A.2 Simulated plot demonstrating first condition $A.3.1$ 90

A.3 Simulated plot demonstrating second condition $A.3.1$ 91

A.4 Simulated plot demonstrating third condition $A.3.1$ 92

A.5 Simulated plot demonstrating condition $A.4.1$ 93

A.6 Simulated plot demonstrating condition $A.4.2$ 94

A.7 Simulated plot demonstrating condition $A.5.1$ 96

A.8 Simulated plot demonstrating condition $A.5.2$ 97

A.9 Simulated plot demonstrating condition $A.5.3$ 98

A.10 Simulated plot demonstrating condition $A.5.4$ 99

A.11 Simulated plot demonstrating stability of $\dot{V}_s$ 100

B.1 Simulated plot demonstrating stability of Assumption 4.2.1 102

List of Tables

3.1 Simulation parameters 29

3.2 Simulation initial conditions 29

3.3 Linear near-optimal design parameters 30

4.1 Nonlinear near-optimal design parameters 43

5.1 Combined high-gain observer design parameters 56

5.2 Cascaded high-gain observer design parameters 67

Chapter 1

Introduction

1.1 Background

Topology measurements help characterize cell structures, inspect polymer mechanical properties, analyze semiconductors, and detect other details not visible to the human-eye [1–3]. An atomic force microscope (AFM) is a tool that scans the surface of small samples to perform topology measurements by monitoring the deflections in its cantilever probe (Fig. 1.1). This micro cantilever's sharp tip interacts with samples to detect the Van der Waals molecular attraction and repulsion forces that bend the cantilever. The topology is measured by using a laser deflection system that bounces a laser off the reflective back of the cantilever onto a photo-diode designed to keep the laser deflection either at a desired set-point or set-oscillation [4]. When the laser moves away from these desired conditions from the bending, the AFM is able to attribute these changes to the sudden forces acting on the tip by the sample. Multiple measurements are taken by performing a lateral raster scan over the surface to record the changes in the sample's surface height [5]. To ensure ideal topology depictions for researchers, an AFM should return the sample's true height, measure the topology in a timely manner, and prevent any damage to the sample.

Figure 1.1: An NT-MDT Ntegra AFM

Source: Adapted from [6]

There are three commonly used modes for controlling AFM: contact mode, tapping mode, and non-contact mode [7]. Contact mode AFM forces the cantilever tip onto the sample while the cantilever scans the surface. This mode ensures that the AFM is measuring the exact height of the sample. However, contact mode risks damaging the surface of soft samples and the cantilever tip itself. Tapping-mode AFM oscillates the cantilever at a set frequency and amplitude about the sample surface. This method reduces the impact of the cantilever tip on the surface by detecting frequency or amplitude changes based on the Van der Waals forces. Because the tip touches the surface, tapping-mode also possesses the risk of damaging the sample and tip. Of these three modes, non-contact mode AFM keeps the tip just above the sample without touching the surface. This prevents any risk of damage to the sample and prolongs the lifespan of the cantilever by reducing the long term strain of its tip. Typical non-contact mode applications operate similarly to tapping-mode where the AFM oscillates the tip above the sample surface by approximating the surface's attraction forces. An example of a topology image produced from non-contact mode AFM can be seen in Fig. 1.2 of a human chromosome [8].

Figure 1.2: Non-contact AFM image of a human chromosome

Source: Adapted from [8]

Of the three modes, non-contact mode AFM presents unique challenges for control methods to solve [9]. Compared to other AFM control modes, non-contact mode scans the surface at a slower rate. Relatively quick AFM scanning is important for certain applications such as biological cell identification where the cells might move along the sample, resulting in an inaccurate scan [1]. Similarly, soft structures can also be damaged if an imaging method contacts the sample [10]. As a result, a non-contact mode AFM approach is preferred, but control methods for non-contact mode must handle jump-to-contact. Jump-to-contact occurs when the attraction force acting on the AFM tip becomes too strong and causes the cantilever to bend towards the sample surface. This disrupts the intended Van der Waals behavior of how the interaction forces affect the cantilever by suddenly influencing the rate of change of the cantilever positioning and imposing large repulsion forces onto the cantilever [11]. Preventing this phenomenon allows for ideal non-contact mode behavior. Another problem for non-contact control involves variations in the Van der Waals forces. Various papers that address these nonlinear forces assume estimated Hamaker constants that represent the particle strength between the AFM tip and sample [12–14]. These fairly small values significantly impact how the molecular forces affect the cantilever and vary across samples and are difficult to determine in practice [15]. As a result, non-contact mode AFM behavior should be able to withstand changing unknown attraction and repulsion Hamaker amounts as the tip hovers across the sample.

1.2 Literature Review

1.2.1 AFM Control Review

Recent research into the control of AFM demonstrates progress towards solving these non-contact mode challenges. Fault-tolerant control was developed by [16] for accurate tip-position tracking about an assumed lateral reference trajectory with respect to unknown nonlinear changes imposed on the non-contact AFM system. A State-Dependent Riccati Equation (SDRE) nonlinear regulator was used by [13] to stabilize periodic orbits about a desired setpoint to handle nonlinear chaotic motions in non-contact AFM. Nonlinear model predictive control methods solved through Hamilton optimization were designed by [12] to maintain an oscillation frequency and mitigate tapping mode chaos. [17] presented an AFM cantilever vibration controller to suppress nonlinear excitation forces.

Some commonalities across AFM research focuses on analyzing and designing controllers about the cantilever dynamics over the vertical direction. Inspecting the AFM from this perspective overlooks the lateral dynamics that represent the desired raster scan trajectory and the dynamics attributed by the attached piezotube that directly controls the cantilever. By neglecting these AFM dynamics, optimal control designs for lateral cantilever control have been proposed for AFM [18, 19]. These designs are difficult to implement in practice because of their focus on two-dimensional lateral cantilever control without considering the effects of the attached piezotube and linearity assumptions. Modeling the complete system and how the voltage inputs affect the deformations of the piezotube and onto the cantilever can allow for a more complete representation of the AFM system [20].

Oscillations are commonly used for non-contact mode AFM to allow for better sensing of the Van der Waals forces, but these small interaction forces are always affecting the cantilever when approaching the sample regardless of oscillation [21]. The control methods for non-contact mode have focused on applying extremely fast vibrations at low amplitudes to oscillate the cantilever about the sample. This has allowed for the ability to monitor fre-

quency shifts and amplitude changes to assist in simplifying the control design [22]. However, by characterizing Van der Waals forces, the control design of non-contact mode can be adjusted to maintain the cantilever tip above a set tip-sample height. Research demonstrates that jump-to-contact becomes an issue when this desired height is of a few angstroms away from the sample. This jump-to-contact risk is reduced by applying a relatively stiff cantilever to minimize the effects of the interaction force [23].

It has been shown that stiffer cantilevers reduce the exposure to measurement noise and can allow for faster scanning [24]. This faster imaging is achieved by reducing the vibrations that limit scanning speed with stiff cantilevers [25]. Stiff cantilevers have also been shown to be more resistant to chaotic motions [26]. As a result, it is reasonable to assume that the cantilever can be designed to be relatively stiff to improve the control objective of non-contact mode AFM.

Singular perturbation techniques redefine systems about a small parameter to minimize the complexity of system modeling and analysis. This approach has been applied to multiple applications. Flexible joints were characterized as fast states in [27] to assist the control of vibrations amongst rigid slow state motions. [28] applied singular perturbation about the inductance of permanent magnet stepper motors to simplify nonlinear position control about fast electrical and slow mechanical dynamics. Researchers have also used singular perturbation techniques to assist the control of AFM. [29] applied singular perturbation about a stiff cantilever to prevent vibrations to improve nanomanipulation. [30] used singular perturbation to design a PI controller about vibrational states to address hysteresis.

Most of the mentioned results that deal with the control of AFM either ignore the system's nonlinearities or resort to conventional (non-optimal) control techniques. This work bridges this gap. Inspired by [29], by assuming that the cantilever can be sufficiently stiff, we show that the AFM system model exhibits a two time-scale property, where the tip dynamics evolve in the slow time-scale and the cantilever vibrations evolve in a fast time-scale. This allows for the design of a composite near-optimal controller to drive the system states to

desired trajectories. Following singular perturbation theory [31–33], we show that we can achieve the control objective by solving two relatively simple sub-problems. Ultimately, we achieve a near-optimal performance that improves as the cantilever increases in stiffness.

1.2.2 Observer-based Control of AFM Review

For most AFM applications, only the positions of the piezotube and the cantilever tip are measurable. The measurement of the cantilever tip undergoes an extensive and expensive process that involves the controlling of lasers to maintain focus on the back of the cantilever so they can be deflected onto a photo-diode to assist in pinpointing the exact location of the tip (Fig. 1.3) [4, 34]. This process is the most common AFM tip measurement method used in industry, as it is perceived as the best way to monitor the tip's deformations as a result of the Van der Waals forces and other disturbances for immediate feedback control.

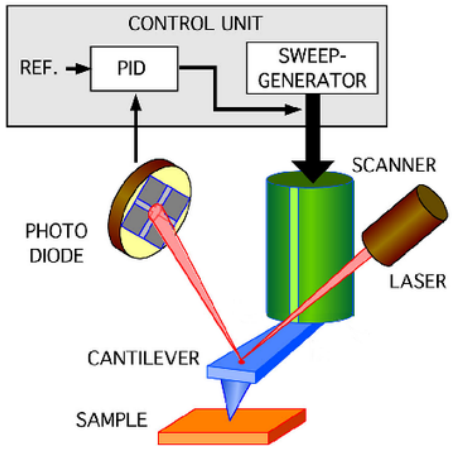

Figure 1.3: General AFM tip measurement feedback control process

Source: Adapted from [35]

With this in mind, one might recognize that the cantilever tip dynamics could be determined from the attached piezotube that controls these dynamics. For AFM however, the position of the piezotube typically goes unmeasured, as the main focus has been on quick sensing of the

cantilever tip. The piezotube's manufacturer typically provides a list of parameters, such as its unique piezoelectric strain constant, which can assist in locating the piezotube's position at given voltages. Unfortunately, the piezoelectric Maxwell capacitance can alter the assumed applied voltage, and the piezotube's structure experiences wear and tear over time causing the parameters to unknowingly change. These occasionally lead to creep, hysteresis, and cross-coupling issues resulting in incomplete or faulty scans [5]. Despite this, recent research and developments on capacitive sensors and other methods for piezotube sensing have shown improvement in verifying the piezotube's dynamics and preventing these issues [36, 37]. For our observer designs, we will assume accurate piezotube displacement measurement sensing.

Observers have be previously used for AFM. Disturbance observers were designed about a simplified AFM model for chaos control about assumed Van der Waals forces acting on the cantilever in [38]. Their work designed Luenberger observers to isolate disturbances and directly counteract them similarity to the work conducted in [39]. Adaptive nonlinear observer parameter estimation for an unknown Van der Waals force was performed in [40] to maintain constant oscillation about a desired position for non-contact mode AFM. By only measuring the tip displacement, their observer was able to identify the Van der Waals parameters used in their simulations. Extended Kalman filters were used to observe nonlinear vibrations of a micro-cantilever beam in [41]. The tip displacement difference with its desired trajectory was monitored to adjust the Kalman gain used in their designed feedback controller. Beam stiffness was also evaluated in their work of which demonstrated reduced vibrations with their controller.

A common application of observers for AFM involve solving for and counteracting the tip-sample interaction forces. Some of these works also assume the Van der Waals model that we've previously also assumed for the design of our near-optimal controllers. We would like to construct an observer that is able to replicate the Van der Waals forces without the need for providing an assumed nonlinear reference equation in our controller, as these forces are not consistent for all sample surfaces and AFM tips. Along with this disturbance, it is not practical to assume that all of the states of the system are known.

The high-gain observer (HGO) is designed to quickly bring state estimates to their measured counterparts. This is appealing for AFM, as their advantages include robustness, recovery of state feedback, fast response time, and they can be simple in design. Most importantly, the design of a HGO satisfies the separation principle which allows us to apply its estimates into an optimal or near-optimal controller [42]. This allows for us to use the estimates produced by a HGO for output feedback. The HGO has evolved over time into the extended high-gain observer (EHGO) and cascaded "full-order" HGO. An EHGO follows that of a regular high-gain observer, but a new state is extended to the system's state vector to represent the system's disturbance. A cascaded observer uses lower-ordered observers to estimate higher derivatives of the system when the order of a system is large [43].

HGO and its variations have been previously applied to optimal and near-optimal controllers for some applications. [44] designed a HGO based optimal controller for an arbitrary discrete nonlinear system where their controller used the HGO to assist in the estimation of disturbances for their controller to counteract. An optimal control based nonlinear model predictive control scheme using estimates from a cascaded EHGO was implemented in [45] to control a flexible joint manipulator. Cascaded observers have been used for various applications. A flexible joint manipulator's link angles and motor dynamics were estimated using only information from the motor angles using a cascaded EHGO observer [46]. A cascade observer was used for a Translating Oscillator with a Rotating Actuator (TORA) design with its state estimates approaching the actual states relatively quickly [47]. An under-actuated inertia wheel pendulum (IWP) system's wheel angle was estimated through a cascaded observer based on the pendulum angle feedback to control the system with a sliding mode controller [48]. Cascaded HGOs were used to estimate the dynamics of a heterogeneous nonlinear multi-agent leader follower system using information about the leader's dynamics with an output feedback controller to drive the follower outputs to that of the leader's [49]. A commonality of most of the work above is that cascaded observers were applied to under-actuated systems, which AFM represents.

In this work, we first solve the state feedback control assuming that all of the states are

available for feedback. This is not practical because in most cases not all of the states are available for feedback or might be costly to measure. To solve this problem, our work outlines and discusses the formulation of cascaded high-gain observers and extended high-gain observers and present two observer designs for our AFM system and apply them for output feedback control. This will provide estimates of all the states that can be fed back to the controller. In addition, we show that, using the proposed HGO design, we can estimate the system nonlinearities. This is very important to make the output feedback robust to modeling uncertainties.

1.3 Contributions and Outline

The work presented in this paper solves a combination of problems for non-contact mode AFM control. Our contributions can be summarized as follows:

1. Inspired by [29], we represent the AFM system in terms of singular perturbation equations for simplified modeling and control design.

2. We follow a singular perturbation approach to design a nonlinear near-optimal tracking controller so that the AFM cantilever tip follows a desired trajectory. This is accomplished by breaking down the control problem down into two simpler problems; one for the slow dynamics and one for the fast dynamics thus making the design procedure systematic and relatively simple.

3. Solve the control problem when only the piezotube position is available for feedback and assuming the system nonlinearities are unknown. This is done through the design of a novel cascade high-gain observer. This output feedback strategy allows for recovery of the near-optimal state feedback controller performance. This is beneficial because it allows for shaping the transient performance of the closed loop system, which is a rarely obtained feature of nonlinear control.

This thesis is organized as followed:

Chapter 2 outlines the AFM control problem by presenting our model and governing equations. We follow this by describing the optimal control problem and how a singular perturbation representation can simplify this problem.

Chapter 3 suggests a singular perturbation based near-optimal feedback control design based on the assumption of linearity. This is presented along with simulations to describe how neglecting the nonlinear interaction forces affects the control performance.

Chapter 4 details our nonlinear near-optimal slow and fast sub-problems and the resulting composite control design. Simulations are presented comparing the performance to PD controllers and our linear near-optimal solution of Chapter 3.

Chapter 5 applies a cascaded high-gain observer design to assist in the monitoring of unknown interaction forces and the velocities of the cantilever and piezotube. These values are then applied to our controller via output feedback.

Chapter 6 concludes our work and provides some extra comments on our findings.

Chapter 2

Problem Formulation

2.1 Atomic Force Microscope (AFM) Dynamics

Scan-by-head AFMs typically feature a vertical piezotube that deforms based on input voltages to move its attached cantilever along the sample surface (Fig. 2.1). The coordinate plane outlined by Fig. 2.1 follows those of [13,34]. It has been shown from existing work that the dynamics representing the piezotube and cantilever each follow a mass spring damper system [12,29,50]. The tip dynamics, (x_{tx}, x_{ty}, x_{tz}), and the center of the piezotube's free-end, (x_{px}, x_{py}, x_{pz}), form the AFM dynamic equations

$$\begin{aligned}
&m_t\ddot{x}_t + c_{tx}\dot{x}_{tx} + k_{tx}(x_{tx} - x_{px}) = 0,\\
&m_t\ddot{y}_t + c_{ty}\dot{x}_{ty} + k_{ty}(x_{ty} - x_{py}) = 0,\\
&m_t\ddot{z}_t + c_{tz}\dot{x}_{tz} + k_{tz}(x_{tz} - x_{pz}) = f_{ts},\\
&m_{px}\ddot{x}_{px} + c_{px}\dot{x}_{px} + k_{px}x_{px} - k_{tx}(x_{tx} - x_{px}) = f_{ux},\\
&m_{py}\ddot{x}_{py} + c_{py}\dot{x}_{py} + k_{py}x_{py} - k_{ty}(x_{ty} - x_{py}) = f_{uy},\\
&m_{pz}\ddot{x}_{pz} + c_{pz}\dot{x}_{pz} + k_{pz}x_{pz} - k_{tz}(x_{tz} - x_{pz}) = f_{uz}.
\end{aligned} \tag{2.1}$$

These dynamics can be represented in terms of vectors and matrices as

$$\begin{aligned} M_t\ddot{x}_t + D_t\dot{x}_t + K_t(x_t - x_p) &= F_{ts}, \\ M_p\ddot{x}_p + D_p\dot{x}_p + K_p x_p - K_t(x_t - x_p) &= Tu, \end{aligned} \tag{2.2}$$

where

$$M_t = \begin{bmatrix} m_t & 0 & 0 \\ 0 & m_t & 0 \\ 0 & 0 & m_t \end{bmatrix}, \quad M_p = \begin{bmatrix} m_{px} & 0 & 0 \\ 0 & m_{py} & 0 \\ 0 & 0 & m_{pz} \end{bmatrix},$$

$$K_t = \begin{bmatrix} k_{tx} & 0 & 0 \\ 0 & k_{ty} & 0 \\ 0 & 0 & k_{tz} \end{bmatrix}, \quad K_p = \begin{bmatrix} k_{px} & 0 & 0 \\ 0 & k_{py} & 0 \\ 0 & 0 & k_{pz} \end{bmatrix},$$

$$D_t = \begin{bmatrix} c_{tx} & 0 & 0 \\ 0 & c_{ty} & 0 \\ 0 & 0 & c_{tz} \end{bmatrix}, \quad D_p = \begin{bmatrix} c_{px} & 0 & 0 \\ 0 & c_{py} & 0 \\ 0 & 0 & c_{pz} \end{bmatrix},$$

$x_t = [x_{tx}, x_{ty}, x_{tz}]^T$, $x_p = [x_{px}, x_{py}, x_{pz}]^T$, $F_{ts} = [0, 0, f_{ts}]^T$, and $u = [u_x, u_y, u_z]^T$. Along each i-axis, m_t is the mass of the tip, c_{ti} is the damping coefficient of the tip, k_{ti} is the spring stiffness of the cantilever, and f_{ts} represents the force caused by the Van der Waals forces from the tip to sample interactions. We are only considering interaction forces along the z-axis because x- and y-axis forces can be neglected in non-contact mode. Along each piezotube electrode pairing, the lumped masses are represented as m_{pi}, stiffness is k_{pi}, and damping is c_{pi}. F_{ts} represents the outside forces enacted on the cantilever. Details about this force will be discussed in the next section. The voltage inputs, (u_x, u_y, u_z), cause small deformations that force movement about the piezotube which translates into cantilever movement by the aforementioned governing equations. The piezotube's transformation ratio T converts the input voltages into these mechanical forces [50]. For the purpose of our work, we will assume the voltage across the piezotube's Maxwell capacitance to be neglected.

To ensure that the AFM cantilever is fixed to resist jump-to-contact, [29] states that force

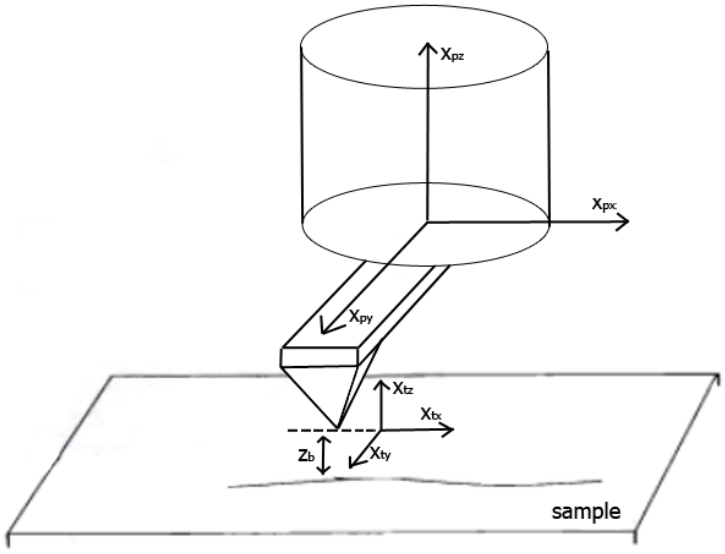

Figure 2.1: AFM scanner coordinate frame where (x_{tx}, x_{ty}, x_{tz}) and (x_{px}, x_{py}, x_{pz}) are the tip and piezotube dynamics respectively and z_b is the tip-sample interaction force equilibrium point

vibrations along the cantilever can be modelled as $z_v = K_t(x_p - x_t)$. This deviation along the cantilever allows for the characterization of its rigidness. By letting $x_t = x_1$, $\dot{x}_t = x_2$, $z_v = z_1$, and $\dot{z}_v = \bar{z}_2$, equation (2.2) is adjusted to represent the vibrations of the cantilever as

$$\begin{aligned} \dot{x}_1 &= x_2, \\ \dot{x}_2 &= M_t^{-1}(-D_t x_2 + z_1 + F_{ts}), \\ \dot{z}_1 &= \bar{z}_2, \\ \dot{\bar{z}}_2 &= -\sigma_{x_1} x_1 + \sigma_{x_2} x_2 - \sigma_{z_1} z_1 - \sigma_{z_2} z_2 + \sigma_u u - \sigma_{F_{ts}} F_{ts}, \end{aligned} \tag{2.3}$$

where $\sigma_{x_1} = M_p^{-1} K_t K_p$, $\sigma_{x_2} = M_p^{-1} K_t (M_p M_t^{-1} D_t - D_p)$, $\sigma_{z_1} = M_p^{-1}(K_t M_p M_t^{-1} + K_t + K_p)$, $\sigma_{z_2} = M_p^{-1} D_p$, $\sigma_u = M_p^{-1} K_t T$, and $\sigma_{F_{ts}} = M_p^{-1} K_t M_p M_t^{-1}$. It can be noted that M_t and M_p are invertible because they are diagonal matrices.

2.2 Nonlinear Van der Waals Force

The forces imposed on the cantilever by the sample follow Lennard-Jones potentials about the Van der Waals force-distance curve. The Van der Waals interaction forces can be described as

$$f_{ts}(x_{1z}) = \frac{R_H r_t}{180(z_b + x_{1z})^8} - \frac{A_H r_t}{6(z_b + x_{1z})^2}, \tag{2.4}$$

where R_H and A_H are the repulsive and attractive Hamaker constants that represent the strength of the molecular particles between the tip and sample, and r_t is the radius of the cantilever tip [15]. These forces as they affect the cantilever tip can be seen in Fig. 2.2. As the cantilever tip approaches the sample, it can be seen that the attractive forces are counteracted by the repulsive forces generated by the sample. The equilibrium point where these interaction forces cancel, where $f_{ts}(x_{1z})$ is zero, is defined as z_b. This nonlinear equation defines our tip height, x_{1z}, origin at z_b such that $f_{1s}(x_{1z}) = 0$ when $x_{1z} = 0$. This is done so we are able to utilize this fact for the application of our control system design in the following chapters.

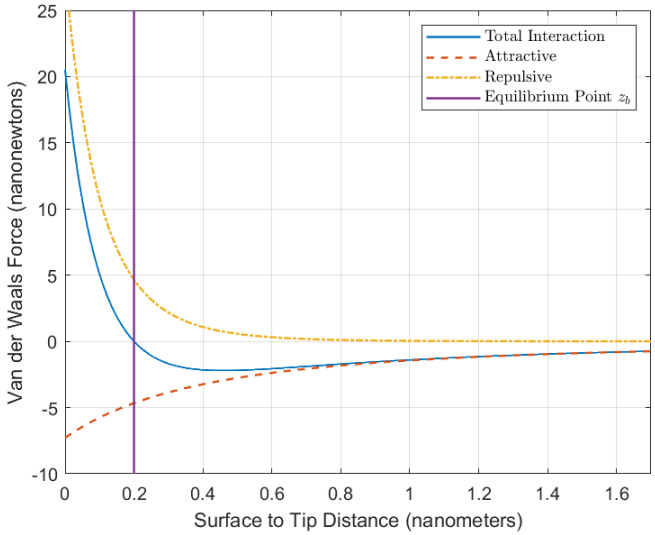

Figure 2.2: Van der Waals force curve highlighting the z_b equilibrium point

With the nonlinear forces defined, our non-contact mode AFM control objective is to maintain the z-axis tip position at the Van der Waals equilibrium point while steering the x- and y-axis about a raster scan desired trajectory.

2.3 Optimal Control Problem

For AFM systems, the non-contact mode control problem revolves around two ideas; maintaining the AFM cantilever tip movement about a desired lateral raster scanning trajectory and keeping the AFM cantilever vertically above a set distance above the sample surface. Raster scanning is performed by driving the states x_{1x} and x_{1y} to desired trajectories x_{1x}^* and x_{1y}^* respectively. Topology scanning is performed by reading the surface height scan of the sample determined by the height of the tip. The conventional way of achieving this is by keeping z-axis tip position x_{1z} at a constant distance above the sample. The closest point at which the tip can be above the sample without imposing significantly large repulsive and attractive forces that would promote vibrational strain is at the Van der Waals force equilibrium point z_b, defined by our system as $x_{1z} = 0$.

Towards this goal, we introduce the error variables $e_1 = x_1 - x_1^*$ and $e_2 = x_2 - x_2^*$ where $x_1^* = [x_{1x}^*, x_{1y}^*, 0]^T$ and $x_2^* = [x_{2x}^*, x_{2y}^*, 0]^T$ represent the desired trajectory. We also require the z states to be driven to equilibrium such that $\bar{z} = 0$. Accordingly, in view of (2.3), the AFM error dynamics can be represented as

$$\begin{aligned} \dot{e} &= a_1(e) + A_1\bar{z} + B_1 u, \\ \dot{\bar{z}} &= \bar{a}_2(e) + \bar{A}_2\bar{z} + \bar{B}_2 u, \end{aligned} \tag{2.5}$$

where $e = [e_1, e_2]^T$, $\bar{z} = [z_1, \bar{z}_2]^T$,

$$a_1(e) = \begin{bmatrix} e_2 \\ -M_t^{-1} D_t e_2 + M_t^{-1} F_{ts}(e_1) \end{bmatrix},$$

$$F_{ts}(e_1) = \begin{bmatrix} 0 & 0 & \dfrac{R_H r_t}{180(z_b + e_{1z})^8} - \dfrac{A_H r_t}{6(z_b + e_{1z})^2} \end{bmatrix}^T,$$

$$A_1 = \begin{bmatrix} 0 & 0 \\ M_t^{-1} & 0 \end{bmatrix}, \quad B_1 = \begin{bmatrix} 0 \\ 0 \end{bmatrix}, \quad \bar{B}_2 = \begin{bmatrix} 0 \\ M_p^{-1} K_t T \end{bmatrix},$$

$$\bar{a}_2(e) = \begin{bmatrix} 0 \\ -\bar{\sigma}_{e_1} e_1 + \bar{\sigma}_{e_2} e_2 - \bar{\sigma}_{F_{ts}} F_{ts}(e_1) \end{bmatrix},$$

$$\bar{A}_2 = \begin{bmatrix} 0 & I \\ -M_p^{-1}(K_t M_p M_t^{-1} + K_t + K_p) & -M_p^{-1} D_p \end{bmatrix},$$

$\bar{\sigma}_{e_1} = M_p^{-1} K_t K_p$, $\bar{\sigma}_{e_2} = M_p^{-1} K_t (M_p M_t^{-1} D_t - D_p)$, and $\bar{\sigma}_{F_{ts}} = M_p^{-1} K_t M_p M_t^{-1}$.

It should be noted that (2.5) has an equilibrium point at the origin. With the error dynamics outlined above, an optimal feedback control design can be implemented to bring the AFM dynamics to follow a desired trajectory by driving the error e and cantilever vibrational force z to zero.

Optimal control is described by the formulation of the Hamilton-Jacobi-Bellman (HJB) equation to solve for the minimal asymptotic solution. The cost function for our system is defined as

$$J = \int_0^\infty \left[p(e) + s^T(e)\bar{z} + \bar{z}^T Q_z \bar{z} + u^T R u \right] dt, \tag{2.6}$$

where

$$Q = \begin{bmatrix} Q_e & 0 \\ 0 & Q_z \end{bmatrix}, \quad Q_e = \begin{bmatrix} q_{e_1} I & 0 \\ 0 & q_{e_2} I \end{bmatrix}, \quad Q_z = \begin{bmatrix} q_{z_1} I & 0 \\ 0 & q_{z_2} I \end{bmatrix}, \quad R = \begin{bmatrix} r_x & 0 & 0 \\ 0 & r_y & 0 \\ 0 & 0 & r_z \end{bmatrix},$$

such that Q, R, and its user adjusted constant gain parameters r_x, r_y, r_z, q_{e1}, q_{e2}, q_{z1}, and q_{z2} remain to be chosen as positive definite. The smooth nonlinear functions $p(e)$ and $s^T(e)$ are designed such that $p(e) + s^T(e)\bar{z} + \bar{z}^T Q_z \bar{z}$ is positive-definite. For our system, we adapt the assumption outlined in [31] to guarantee that the origin is our desired equilibrium.

Assumption 2.3.1. *There exists a domain $D \subset \mathbb{R}^6$, containing the origin as an interior point, such that for all $e \in D$ functions a_1, a_2, A_1, A_2, A_2^{-1}, B_2, p, s, R, and Q_z are differentiable with respect to e; a_1, a_2, and p are zero only at $e = 0$; Q_z and R are positive-definite matrices for all $e \in D$; the scalar $p + s^T\bar{z} + \bar{z}^T Q_z \bar{z}$ is a positive-definite function of its arguments e and $\bar{z}$.*

This assumption is verifiable by design for our application. Because the equilibrium of our system is designed at the origin, a positive-definite function $V(e, \bar{z})$ can be assumed to exist which satisfies the HJB equation

$$0 = \min_u \begin{bmatrix} p(e) + s^T(e)\bar{z} + \bar{z}^T Q_z \bar{z} + u^T R u \\ + \dfrac{\partial V}{\partial e}(a_1(e) + A_1\bar{z} + B_1 u) \\ + \dfrac{\partial V}{\partial z}(a_2(e) + A_2\bar{z} + B_2 u) \end{bmatrix}, \tag{2.7}$$

where $\dfrac{\partial V}{\partial e}$ and $\dfrac{\partial V}{\partial z}$ are the partial derivatives of V with respect to e and $\bar{z}$ respectively [51]. The control u minimizing (2.7) is given by

$$u = -\frac{1}{2} R^{-1}(B_1^T \frac{\partial V}{\partial e} + B_2^T \frac{\partial V}{\partial z}). \tag{2.8}$$

Applying u into (2.8), the HJB equation becomes

$$\begin{aligned} 0 &= p(e) + s^T(e)\bar{z} + \bar{z}^T Q_z \bar{z} \\ &+ \frac{\partial V}{\partial e}(a_1(e) + A_1\bar{z}) + \frac{\partial V}{\partial z}(a_2(e) + A_2\bar{z}) \\ &- \frac{1}{4}(\frac{\partial V}{\partial e}B_1 + \frac{\partial V}{\partial z}B_2) R^{-1}(B_1^T \frac{\partial V}{\partial e}^T + B_2^T \frac{\partial V}{\partial z}^T). \end{aligned} \tag{2.9}$$

Because the HJB expression is a single equation with twelve unknowns across $\dfrac{\partial V}{\partial e}$ and $\dfrac{\partial V}{\partial z}$, solving this equation for $\dfrac{\partial V}{\partial e}$ and $\dfrac{\partial V}{\partial z}$, with the constraint $V(0, 0) = 0$, is a challenging problem that would involve a considerable amount of trial and error.

In this work, we will solve this problem by exploiting the cantilever stiffness as a design parameter. By choosing this design parameter sufficiently high, the system dynamics evolve in two time scales. This, in turn, will allow for a singular perturbation method to be used

to decouple the control problem into two simpler sub-problems. This will be shown in the following section.

2.4 Singular Perturbation Model

By considering the effects of stiffness on the cantilever, as demonstrated by [29], (2.5) can be rewritten to consist of fast and slow subsystems. This can reduce the number of unknowns in the HJB equation and assist our efforts of defining a control system. Assuming the cantilever's stiffness is fairly large of the order $O(1/\epsilon^2)$, we can define a new parameter

$$K_t = \frac{K_t^*}{\epsilon^2} \tag{2.10}$$

where ϵ is a small positive parameter. Along with this, we will define $z_2 = \epsilon \bar{z}_2$ with $z = [z_1, z_2]^T$. This variable change is acceptable as z is going to be driven to zero by the proposed controller. With the variable change and (2.10) in mind, (2.5) can be written as

$$\begin{aligned} \dot{e} &= a_1(e) + A_1 z + B_1 u, \\ \epsilon \dot{z} &= a_2(e) + A_2 z + B_2 u, \end{aligned} \tag{2.11}$$

where

$$a_2(e) = \begin{bmatrix} 0 \\ -\sigma_{e_1} e_1 + \sigma_{e_2} e_2 - \sigma_{F_{ts}} F_{ts}(e_1) \end{bmatrix},$$

$$A_2 = \begin{bmatrix} 0 & I \\ -M_p^{-1}(K_t^* M_p M_t^{-1} + K_t^* + \epsilon^2 K_p) & -\epsilon M_p^{-1} D_p \end{bmatrix},$$

$$B_2 = \begin{bmatrix} 0 \\ M_p^{-1} K_t^* T \end{bmatrix},$$

$\sigma_{e_1} = M_p^{-1} K_t^* K_p$, $\sigma_{e_2} = M_p^{-1} K_t^* (M_p M_t^{-1} D_t - D_p)$, and $\sigma_{F_{ts}} = M_p^{-1} K_t^* M_p M_t^{-1}$. Model (2.11) is in the standard singular perturbation form, where e is the slow state and z is the fast state. A singular perturbation representation of our AFM model allows for a simplification for how the voltage inputs of the piezotube effect the z cantilever vibrational force fast dynamics that directly move the cantilever tip location. This also allows for quick sensing of the force

interactions enacting on the cantilever through the fast vibration states. In the following chapters, the slow and fast subsystems are defined and used to design composite controllers.

Chapter 3

Linear Near-optimal Feedback Design

3.1 Singular Perturbation Theory

To better understand singular perturbation theory, we will design a system about linear variables. Given a linear system comprised of

$$\begin{aligned} \dot{x} &= A_{11}x + A_{12}z + B_1u, \\ \epsilon\dot{z} &= A_{21}x + A_{22}z + B_2u, \end{aligned} \tag{3.1}$$

the system can be seen to consist of the slow state x and fast state z [33]. z is considered a fast state, as ϵ is chosen such that $0 < \epsilon < 1$ which brings z to its isolated roots at a faster rate than x. Singular perturbation theory provides assumptions about the system's performance based on how small ϵ is. The theory presumes that ϵ can be assumed to be zero and the system's model ultimately performs similarly to when ϵ is small. Applying this assumption of $\epsilon = 0$ to our example results in

$$\begin{aligned} \dot{x}_s &= A_0x_s + B_0u_s, \\ z_s &= -A_{22}^{-1}(A_{21}x_s + B_2u_s), \end{aligned} \tag{3.2}$$

where

$$A_0 = A_{11} - A_{12}A_{22}^{-1}A_{21}, \qquad B_0 = B_1 - A_{12}A_{22}^{-1}B_2.$$

This equation represents the quasi-steady-state model for the system consisting of the slow elements of the system where z is brought to its isolated root. The found z_s root replaces z from the original expression to create the slow subsystem above. This slow subsystem represents its own control problem and can be solved by conventional means to produce a u_s.

To reassess the system about the previously made assumption, we must consider the convergence of z as it approaches its isolated root. As a result, the fast subsystem represents the system of $z_f = z - z_s$ to design around the performance of z that was not accounted for in the slow subsystem. This can be represented as

$$\epsilon \dot{z}_f = A_{22} z_f + B_2 u_f, \tag{3.3}$$

where $u_f = u - u_s$.

With both subsystems and their controllers identified, singular perturbation theory states that a near-optimal controller can be constructed for the overall system based on $u_c = u_s + u_f$. This controller is considered near-optimal, as the theory promotes the assumptions of relatively small epsilons bringing the system to the slow state performance. When ϵ approaches 0, the system is designed to approach the solution of the slow subsystem thus promoting optimally about the slow dynamics.

3.2 Linear Singular Perturbation Model

In this section, we will only consider the linear dynamics of the system as a motivation for our main result for control of the nonlinear model (2.11). The controller for this section follows the linear near-optimal regulator formulation presented in [33, 52].

Considering only the linear dynamics of the system, we have

$$\begin{bmatrix} \dot{e} \\ \epsilon\dot{z} \end{bmatrix} = \begin{bmatrix} A_{11} & A_{12} \\ A_{21} & A_{22} \end{bmatrix} \begin{bmatrix} e \\ z \end{bmatrix} + \begin{bmatrix} B_1 \\ B_2 \end{bmatrix} u, \qquad y = \begin{bmatrix} M_1 & M_2 \end{bmatrix} \begin{bmatrix} e \\ z \end{bmatrix} \tag{3.4}$$

where

$$A_{11} = \begin{bmatrix} 0 & I \\ 0 & -M_t^{-1}D_t \end{bmatrix}, \quad A_{12} = \begin{bmatrix} 0 & 0 \\ M_t^{-1} & 0 \end{bmatrix}, \quad A_{21} = \begin{bmatrix} 0 & 0 \\ -\sigma_{e_1} & \sigma_{e_2} \end{bmatrix},$$
$$A_{22} = \begin{bmatrix} 0 & I \\ -\sigma_{z_1} & -\sigma_{z_2} \end{bmatrix}, \quad B_1 = \begin{bmatrix} 0 \\ 0 \end{bmatrix}, \quad B_2 = \begin{bmatrix} 0 \\ M_p^{-1}K_t^*T \end{bmatrix},$$
$$M_1 = \begin{bmatrix} q_{e_1}I & 0 & 0 & 0 \\ 0 & q_{e_2}I & 0 & 0 \\ 0 & 0 & 0 & 0 \\ 0 & 0 & 0 & 0 \end{bmatrix}, \quad M_2 = \begin{bmatrix} 0 & 0 & 0 & 0 \\ 0 & 0 & 0 & 0 \\ 0 & 0 & q_{z_1}I & 0 \\ 0 & 0 & 0 & q_{z_2}I \end{bmatrix},$$

$\sigma_{z_1} = M_p^{-1}(K_t^*M_pM_t^{-1} + K_t^* + \epsilon^2K_p)$, and $\sigma_{z_2} = \epsilon M_p^{-1}D_p$. q_{e_1}, q_{e_2}, q_{z_1}, and q_{z_2} represent chosen constant gains to adjust the weight of the output of each state for the controller. The output expression y is assumed to have the complete knowledge about each of the states.

Resulting from the above linear expression, the optimal control problem previously described by solving the cost function (2.6) changes to become the cost function

$$J = \frac{1}{2}\int_0^\infty (y^Ty + u^TRu)dt, \tag{3.5}$$

where R is to be chosen as positive definite. [52] defines the solution to this problem as

$$u = -R^{-1}B^TK \begin{bmatrix} e \\ z \end{bmatrix}, \tag{3.6}$$

where K is the solution to the Riccati equation

$$0 = -KA - A^TK + KBR^{-1}B^TK - M^TM. \tag{3.7}$$

Despite the reduced complexity compared to (2.6), this problem also attempts to solve for a controller of a forth-order system. Because we are able to represent the AFM dynamics as a singular perturbation equation, we are able to separate the linear system dynamics into slow and fast sub-problems to simplify the forth-order system into two second-order systems.

3.3 Linear Near-optimal Control Design

With the defined linear AFM dynamics, the slow state e and fast state z can be decomposed into two second-order sub-problems.

3.3.1 Linear Slow Sub-problem

The slow sub-problem is achieved by setting $\epsilon = 0$ and solving for a converged root of z to represent the system in-terms of e. This allows us to construct a quasi-state model representation of the slow states under the condition that, with a relatively small ϵ, z will swiftly converge to its root. Setting $\epsilon = 0$ for (3.4) produces

$$\begin{aligned} \begin{bmatrix} \dot{e_s} \\ 0 \end{bmatrix} &= \begin{bmatrix} A_{11} & A_{12} \\ A_{21} & A_{22s} \end{bmatrix} \begin{bmatrix} e_s \\ z_s \end{bmatrix} + \begin{bmatrix} B_1 \\ B_2 \end{bmatrix} u_s, \\ y_s &= \begin{bmatrix} M_1 & M_2 \end{bmatrix} \begin{bmatrix} e_s \\ z_s \end{bmatrix}, \end{aligned} \tag{3.8}$$

where

$$A_{22s} = \begin{bmatrix} 0 & I \\ -M_p^{-1}(K_t^* M_p M_t^{-1} + K_t^*) & 0 \end{bmatrix}.$$

It is noted that A_{22s} is invertible. Note that we use subscript s to emphasize the fact the states are evolving according to the slow time-scale. Solving for z_s in (3.8) results in

$$z_s = -A_{22s}^{-1}(A_{21} e_s + B_2 u_s). \tag{3.9}$$

Substituting (3.9) into (3.8) and reorganizing the system about e_s results in

$$\begin{aligned} \dot{e}_s &= A_0 e_s + B_0 u_s, \\ y_s &= M_0 e_s + N_0 u_s, \end{aligned} \tag{3.10}$$

where

$$A_0 = A_{11} - A_{12}A_{22s}^{-1}A_{21} = \begin{bmatrix} 0 & I \\ -K_p(M_p + M_t)^{-1} & -(D_p + D_t)(M_p + M_t)^{-1} \end{bmatrix},$$

$$B_0 = B_1 - A_{12}A_{22s}^{-1}B_2 = \begin{bmatrix} 0 \\ T(M_p + M_t)^{-1} \end{bmatrix},$$

$$M_0 = M_1 - M_2 A_{22s}^{-1} A_{21}$$

$$N_0 = -M_2 A_{22s}^{-1} B_2$$

The linear regulator cost function of (3.5) is now transformed into the slow linear regulator problem

$$J_s = \frac{1}{2}\int_0^\infty (y_s^T y_s + u_s^T R u_s)dt = \frac{1}{2}\int_0^\infty (e_s^T M_0^T M_0 e_s + 2u_s^T N_0^T e_s + u_s^T R_0 u_s)dt, \tag{3.11}$$

where

$$R_0 = R + N_0^T N_0 \tag{3.12}$$

The slow subsystem (3.10) and cost function (3.11) combine to create the slow HJB equation

$$0 = \min_{u_s}\left[e_s^T M_0^T M_0 e_s + 2u_s^T N_0^T e_s + u_s^T R_0 u_s + \frac{\partial V_s}{\partial e_s}(A_0 e_s + B_0 u_s)\right], \tag{3.13}$$

where $\dfrac{\partial V_s}{\partial e_s}$ is the gradient of V_s with respect to state e_s which represents the Lyapunov stability criteria for (3.11). The goal of (3.11) and (3.13) is to find a u_s which minimizes J_s. For linear quadratic regulator problems, a common choice for V_s that we can apply to our system is

$$V_s = e_s^T P_s e_s, \tag{3.14}$$

where P_s represents a unique real symmetric positive definite matrix. The relationship between the gradient and derivative of (3.14) can be seen as

$$\dot{V}_s = \frac{\partial V_s}{\partial e_s}\dot{e}_s. \tag{3.15}$$

By evaluating (3.14) and (3.15), we can deduce that the gradient is

$$\frac{\partial V_s}{\partial e_s} = e_s^T P_s. \tag{3.16}$$

u_s is identified by taking the partial derivative of (3.13) with respect to u_s and solving for u_s. Applying this along with (3.16) results in

$$u_s = -R_0^{-1}(N_0^T M_0 + B_0^T P_s)e_s = G_0 e_s \tag{3.17}$$

With V_s, $\dfrac{\partial V_s}{\partial e_s}$, and u_s chosen and identified, they can applied back into (3.13) to generate the Riccati equation

$$\begin{aligned} 0 = P_s(A_0 - B_0 R_0^{-1} N_0^T M_0) + (A_0 - B_0 R_0^{-1} N_0^T M_0)^T P_s \\ -P_s B_0 R_0^{-1} B_0^T P_s + M_0^T (I - N_0 R_0^{-1} N_0^T) M_0. \end{aligned} \tag{3.18}$$

Following the work of [33, 53], P_s exists when (M_0, A_0, B_0) is controllable and observable which our system satisfies.

3.3.2 Linear Fast Sub-problem

Because the vibrational forces are expected to resonate to zero significantly faster than the cantilever positioning, the slow variable e can be stretched along a time scale τ and the fast system equilibrium can be shifted to the origin. This results in the fast subsystem to be represented as

$$\begin{aligned} \frac{dz_f}{d\tau} &= A_{22} z_f + B_2 u_f, \\ y_f &= M_2 z_f, \end{aligned} \tag{3.19}$$

where

$$z_f = z - z_s = z + A_{22}^{-1}(A_{21} e_s + B_2 u_s).$$

The fast control problem is designed similarity to (3.11) and is presented as the cost function

$$J_f = \frac{1}{2}\int_0^\infty (y_f^T y_f + u_f^T R u_f) dt = \frac{1}{2}\int_0^\infty (z_f^T M_2^T M_2 z_f + u_f^T R u_f) dt, \tag{3.20}$$

The fast subsystem (3.19) and cost function (3.20) combine to create the fast HJB equation

$$0 = \min_{u_f} \left[z_f^T M_2^T M_2 z_f + u_f^T R u_f + \frac{\partial V_f}{\partial z_f}(A_{22} z_f + B_2 u_f) \right], \tag{3.21}$$

where $\frac{\partial V_f}{\partial z_f}$ is the gradient of V_f with respect to state z_f which represents the Lyapunov stability criteria for (3.20). The goal of (3.20) and (3.21) is to find a u_f which minimizes J_f. Following a similar procedure and reasoning to what was performed in Section 3.3.1, the gradient of V_f with respect to z_f can be set as

$$\frac{\partial V_f}{\partial z_f} = z_f^T P_f. \tag{3.22}$$

where P_f represents a unique real symmetric positive definite matrix. With z_f being a function of e_s and z, its Lyapunov function can be written as

$$V_f(e_s, z) = z_f^T P_f z_f \tag{3.23}$$

u_f is identified by taking the partial derivative of (3.21) with respect to u_f and solving for u_f. Applying this along with (3.22) results in

$$u_f = -R^{-1} B_2^T P_f z_f = G_2 z_f \tag{3.24}$$

With $\frac{\partial V_f}{\partial z_f}$ and u_f chosen and identified, they can applied back into (3.21) to generate the Riccati equation

$$0 = P_f A_{22} + A_{22}^T P_f - P_f B_2 R^{-1} B_2^T P_f + M_2^T M_2 \tag{3.25}$$

Following the work of [33], P_f exists when (M_2, A_{22}, B_2) is controllable and observable which our system satisfies.

3.3.3 Linear Composite Control

According to singular perturbation theory, a composite controller for the system is taken as the summation of slow and fast controllers the represent the solution to their respective slow

and fast sub-problems. For our linearized system, u_s is defined by (3.17) and u_f is defined by (3.24) which combine to create composite controller

$$u_c = u_s + u_f = G_0 e + G_2(z + A_{22}^{-1}(A_{21}e + B_2 G_0 e)) = G_1 e + G_2 z \tag{3.26}$$

where

$$G_1 = (I - G_2 A_{22}^{-1} B_2)G_0 + G_2 A_{22}^{-1} A_{21}$$

This controller is based on feedback of our error states e and vibrational forces z to control their defined slow and fast sub-problems. Instead of solving for the optimal value of u in (3.5), the solutions to the defined slow and fast sub-problems construct near-optimal u_c. This solution is considered to be near-optimal because, as ϵ approaches zero, the cost function (3.5) solution, when applying u_c as u, approaches the solution to the slow sub-problem (3.11). With our controller identified, we can apply it to our model to demonstrate its performance.

3.4 Linear Near-optimal Simulations

The aforementioned controller was designed for our AFM model for the purpose of controlling the cantilever tip about desired trajectories. Simulations were performed to demonstrate the effectiveness of our controller. Although we designed the linear controller about linearized AFM dynamics, the simulations presented here apply the linear controller for the actual system dynamics of (2.11) including its nonlinearities. To be accurate with physical AFM systems, our system parameters represent reasonable values from various AFM literature [15, 29, 50]. These values are provided by Table 3.1. Our applied initial conditions are declared in Table 3.2. Along with these values, our design parameters chosen uniquely for the linear near-optimal controller used to control our system in the simulations are outlined in Table 3.3. Because the cantilever cannot be made infinitely stiff, $\epsilon = 0.1$ for our simulations which references a stiffness of $k_{ti} = 100N/m$. This value for cantilever stiffness is reasonable and has been applied for existing AFM applications [29].

Fig. 3.1 shows the performance of x_{1t} as the cantilever tip approaches and follows the desired trajectory for each axis. For Fig. 3.1a, it can be seen that the controller is able to handle sudden directional changes in the desired trajectory which represent that of raster scanning. For Fig. 3.1c, the tip is able to travel to the Van der Waals equilibrium position, z_b, which demonstrates the optimal position of the cantilever such that it remains in non-contact with the sample before the repulsive and attractive forces are able to sway the cantilever towards or away from the sample. Fig. 3.2 displays how the velocity of the cantilever tip is able to approach the rate of change of the desired trajectory position along each axis. Fig. 3.3 and Fig. 3.4 represent how the movement of the piezotube center of which the cantilever is attached to is adjusted to directly control the cantilever tip. Fig. 3.5 and Fig. 3.6 showcase the vibrational forces and impulses impacting the cantilever along each axis of which the controller is able to bring both of these states to zero. This is ideal as we are able to maintain a sturdy cantilever as it travels along the sample surface. Fig. 3.7 and Fig. 3.8 both show that the error between the desired and actual cantilever tip trajectories successfully approach zero; matching the expected performance of the chosen controller. Fig. 3.9 presents the control effort produced by our designed controller which produces the results from the previously mentioned figures. It can be noted in Fig. 3.9a and Fig. 3.9b that the control effort increases and decreases depending on the desired trajectory. The nonlinear forces affecting our system are represented in Fig. 3.10. The nonlinear forces are able to go to zero due to the strength of the control effort about the vibrational states whose objective to so bring z_1 and z_2 to zero. This relationship can be noted by the similarities in the total interaction forces in Fig. 3.10 and Fig. 3.5c. Fig. 3.11 presents a comparison of the error performance over different epsilon values. The parameters used for Fig. 3.11 were adjusted such that $z_{1i,0} = 0$ N to reduce the noise of smaller epsilons.

Table 3.1: Simulation parameters

Model Parameter	Symbol	Numerical Value
Tip Mass	m_t	2×10^{-12} kg
Piezotube Mass	m_{pi}	3.75×10^{-3} kg
Cantilever Stiffness	k_{ti}^*	1 N/m
Piezotube Stiffness	k_{pi}	6×10^6 N/m
Cantilever Damping	c_{ti}	7×10^{-9} N.s/m
Piezotube Damping	c_{pi}	150 N.s/m
Transformer Ratio	T	10 C/m
Tip Radius	r_t	150×10^{-9} m
Attractive Hamaker Constant	A_H	1.865×10^{-19} J
Repulsive Hamaker Constant	R_H	1.3596×10^{-70} Jm^6

Table 3.2: Simulation initial conditions

Symbol	Numerical Value
$x_{1ti,0}$	3×10^{-9} m
$x_{2ti,0}$	0 m/s
$x_{1pi,0}$	3×10^{-9} m
$x_{2pi,0}$	0 m/s
$z_{1i,0}$	1×10^{-8} N
$z_{2i,0}$	0 N/s

Table 3.3: Linear near-optimal design parameters

Symbol	Numerical Value
ϵ	0.1
q_{e_1}	5×10^6
q_{e_2}	2.75×10^2
q_{z_1}	1×10^2
q_{z_2}	1×10^2
r_i	1×10^{-4}

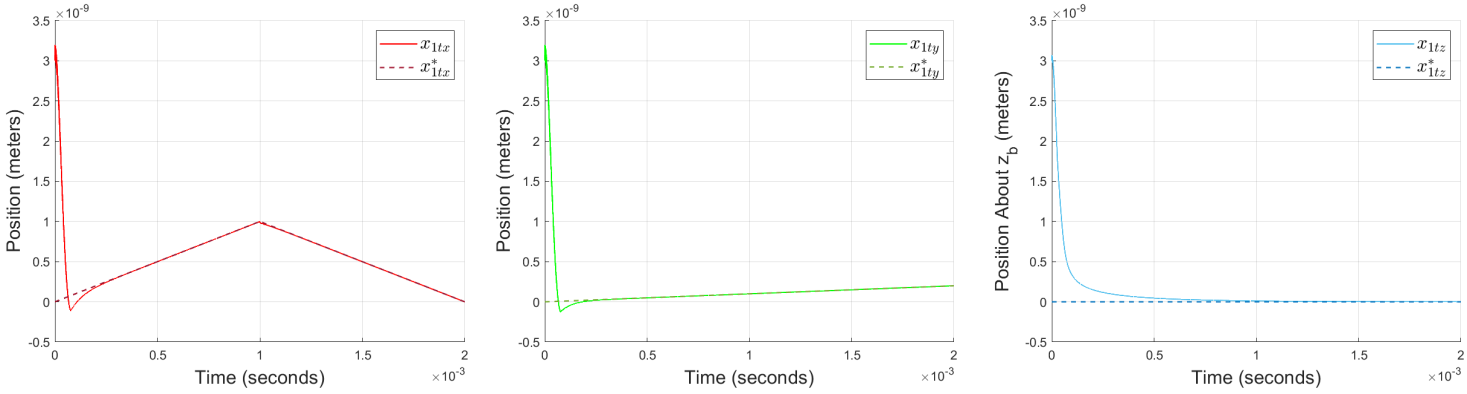

(a) X-axis tip position (b) Y-axis tip position (c) Z-axis tip position

Figure 3.1: Linear near-optimal control x_{1t} performance

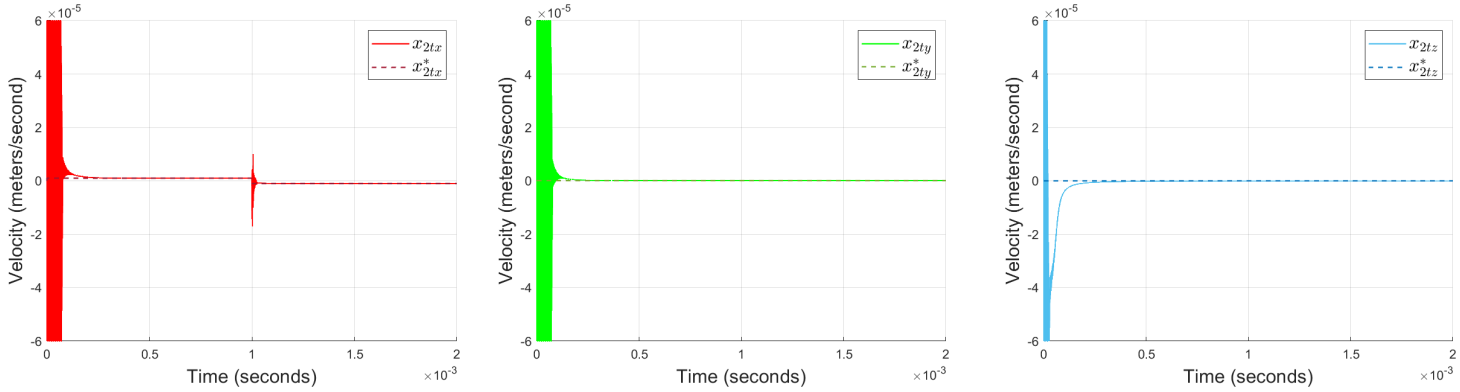

(a) X-axis tip velocity (b) Y-axis tip velocity (c) Z-axis tip velocity

Figure 3.2: Linear near-optimal control x_{2t} performance

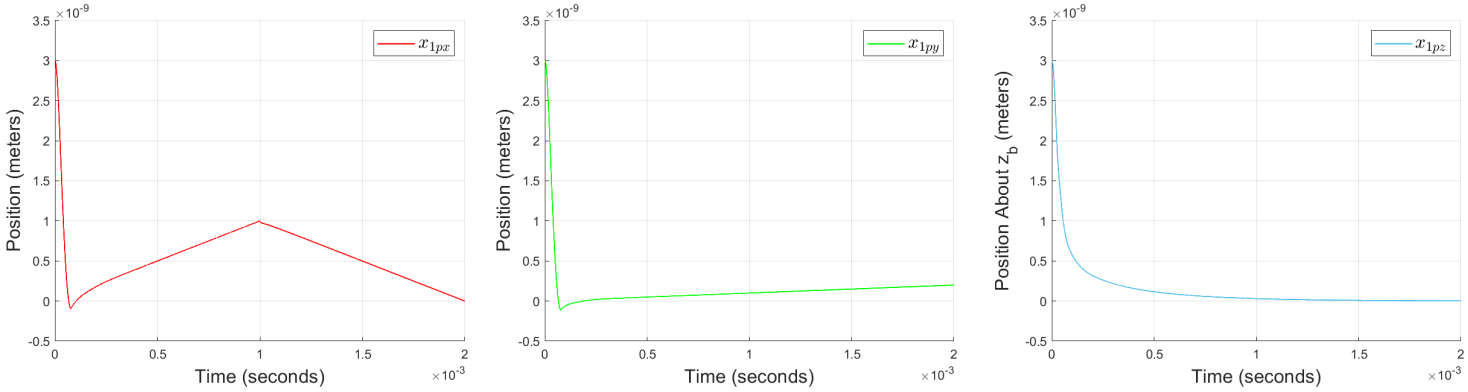

(a) X-axis piezotube position (b) Y-axis piezotube position (c) Z-axis piezotube position

Figure 3.3: Linear near-optimal control x_{1p} performance

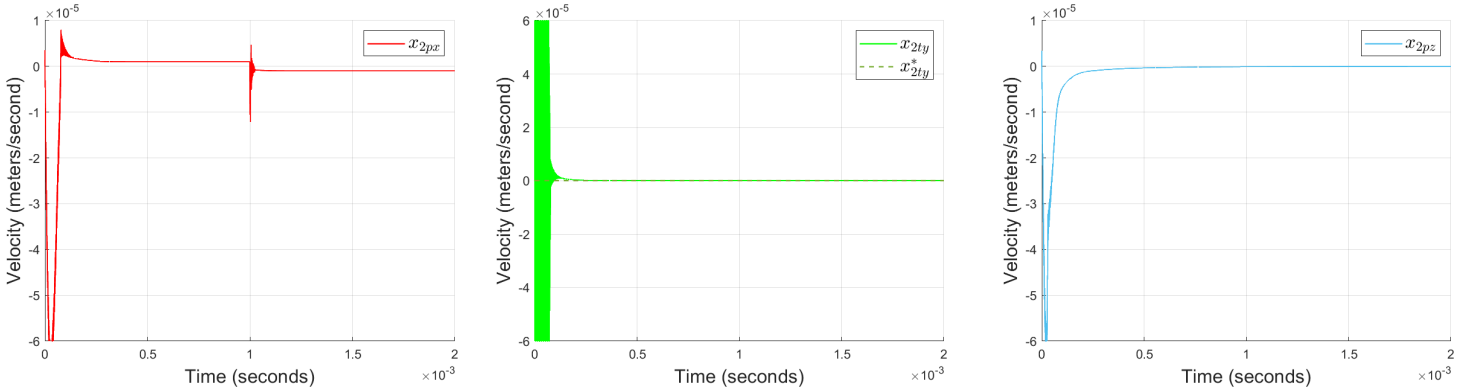

(a) X-axis piezotube velocity (b) Y-axis piezotube velocity (c) Z-axis piezotube velocity

Figure 3.4: Linear near-optimal control x_{2p} performance

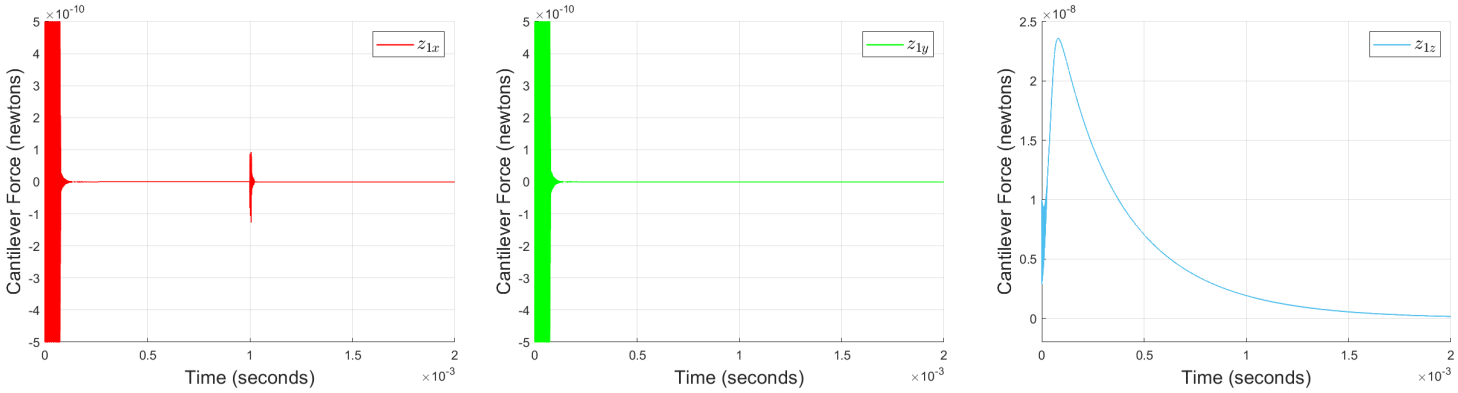

(a) X-axis vibrational force (b) Y-axis vibrational force (c) Z-axis vibrational force

Figure 3.5: Linear near-optimal control z_1 performance

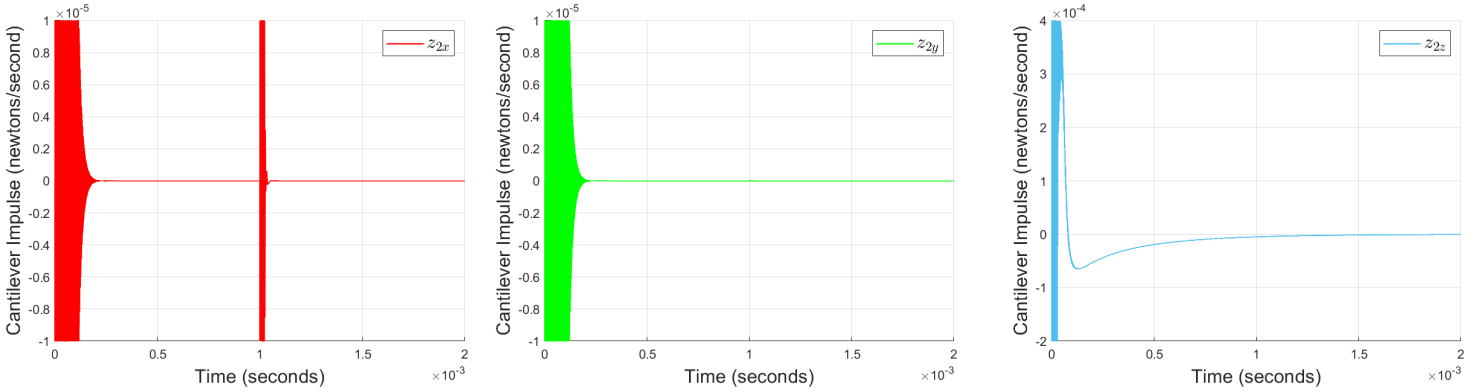

(a) X-axis vibrational impulse (b) Y-axis vibrational impulse (c) Z-axis vibrational impulse

Figure 3.6: Linear near-optimal control z_2 performance

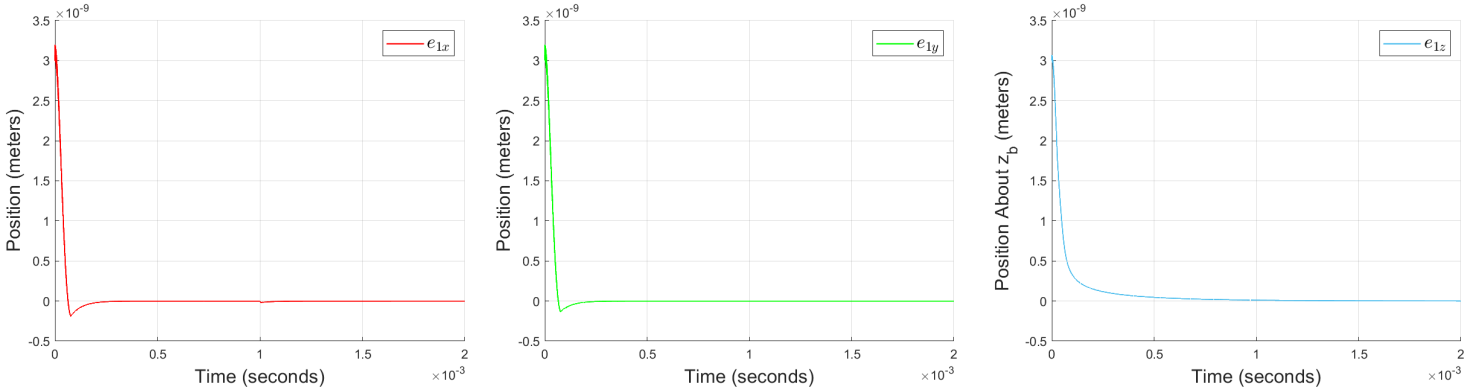

(a) X-axis tip position error (b) Y-axis tip position error (c) Z-axis tip position error

Figure 3.7: Linear near-optimal control e_1 performance

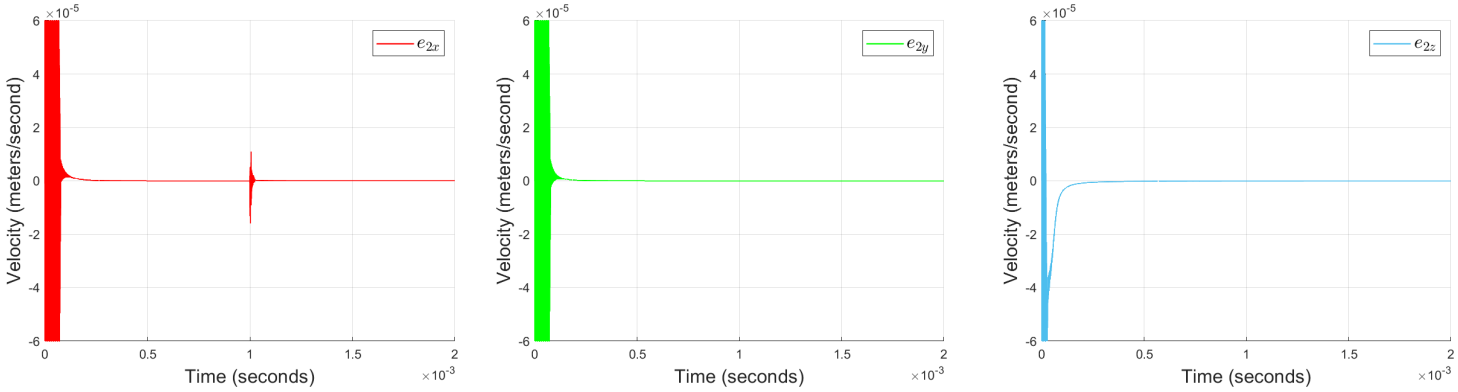

(a) X-axis tip velocity error (b) Y-axis tip velocity error (c) Z-axis tip velocity error

Figure 3.8: Linear near-optimal control e_2 performance

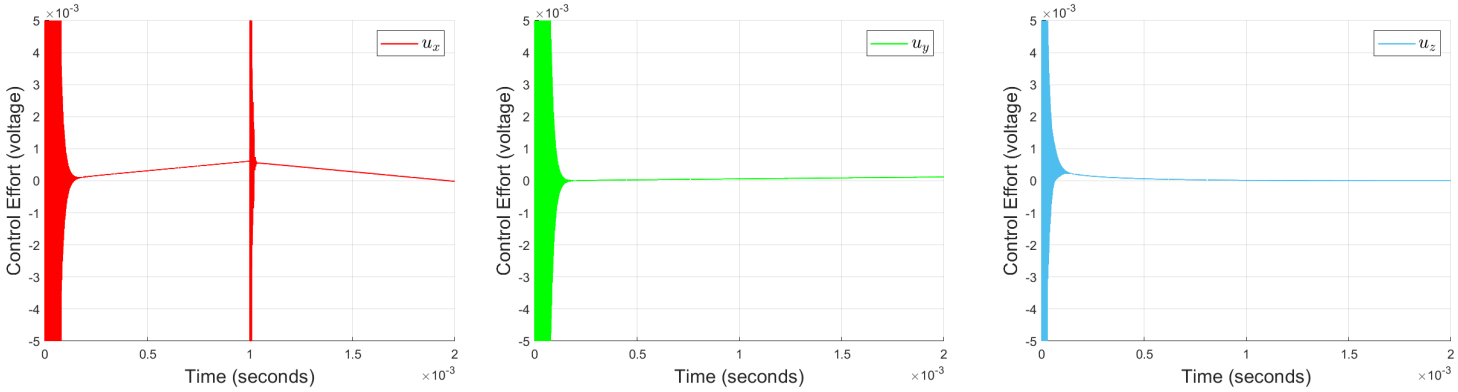

(a) X-axis control effort (b) Y-axis control effort (c) Z-axis control effort

Figure 3.9: Linear near-optimal control u control effort

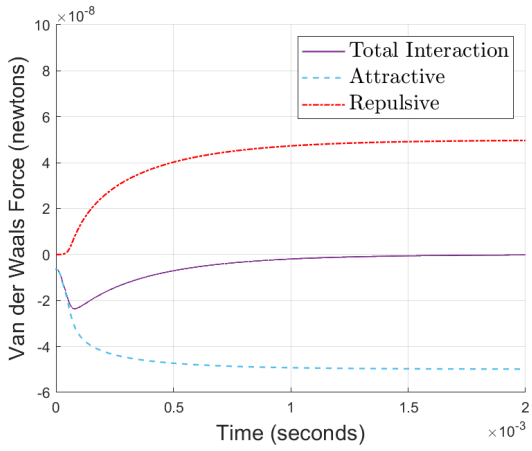

Figure 3.10: Interaction forces affecting the linear near-optimal controller

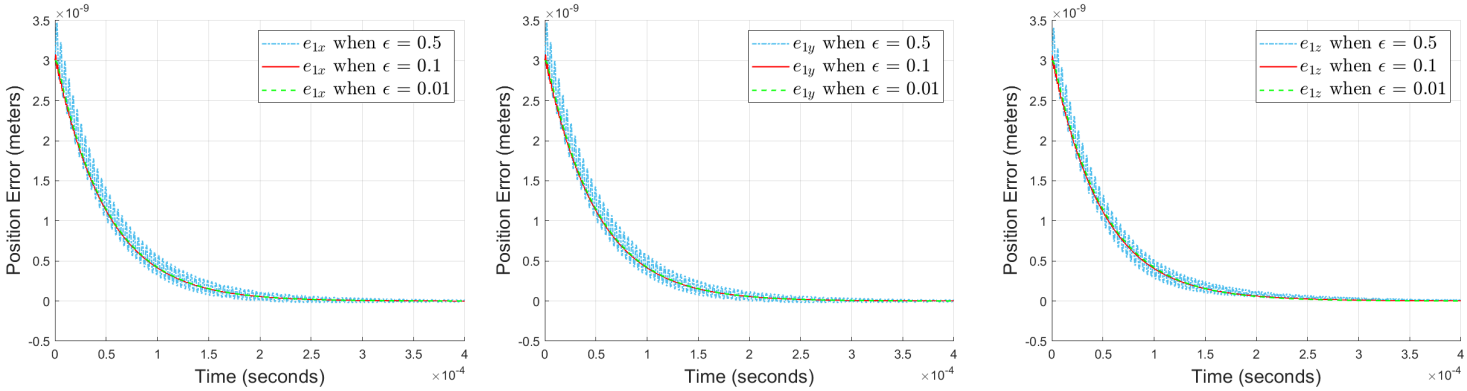

(a) X-axis tip position error (b) Y-axis tip position error (c) Z-axis tip position error

Figure 3.11: Linear near-optimal control e_1 performance across varying epsilons

Despite reasonable performance from our linear near-optimal controller, it can be seen that overshoot and noise are problems in some of the figures. When the initial conditions were raised larger then what was specified in Table 3.2, the system would go unstable with the outlined linear controller. To fix these issues, we wish to focus on the nonlinearities presented by the interaction forces. In the next section, we will continue to apply singular perturbation principles in the design of a nonlinear near-optimal controller.

Chapter 4

Nonlinear Near-optimal Feedback Design

4.1 Addressing Nonlinear Interaction Forces

Because of the potential uncertainties from nonlinearities when applying a linear controller, we wish to define a controller that is equipped to mitigate the exposure to them. For AFM applications, the Van der Waals forces are usually unknown, but they follow the nonlinear structure stated in (2.4). Although we are continuing to assume that the Van der Waals nonlinearity is known, this chapter leads into the following chapter by outlining a nonlinear controller to handle this nonlinearity.

4.2 Nonlinear Near-optimal Control Design

From our AFM singular perturbation model of (2.11), we will design a composite controller consisting of slow and fast controllers to bring the cantilever tip to desired trajectories, minimize the vibrational forces, and reduce the effects of the Van der Waals nonlinearity.

The work demonstrated in this section follows the singular perturbation methods of [31–33] to assist in the design of our AFM controller.

4.2.1 Nonlinear Slow Sub-problem

Because of small parameter ϵ, we are able to apply singular perturbation principles to separate out the fast transient z. Letting $\epsilon = 0$ in (2.11), the fast transient is removed, and the remaining slow system becomes

$$\dot{e}_s = a_1(e_s) + A_1 z_s, \tag{4.1}$$

$$0 = a_2(e_s) + A_{2s} z_s + B_2 u_s, \tag{4.2}$$

where

$$A_{2s} = \begin{bmatrix} 0 & I \\ -M_p^{-1}(K_t^* M_p M_t^{-1} + K_t^*) & 0 \end{bmatrix}.$$

It is noted that A_{2s} is invertible. Note that we use subscript s to emphasize the fact the states are evolving according to the slow time-scale. By solving for z_s in (4.2), z_s becomes

$$z_s = -A_{2s}^{-1}(a_2(e_s) + B_2 u_s) \tag{4.3}$$

Substituting by (4.3) into (4.1) results in the slow subsystem

$$\dot{e}_s = a_0(e_s) + B_0 u_s, \tag{4.4}$$

where

$$a_0(e_s) = a_1(e_s) - A_1 A_{2s}^{-1} a_2(e_s) = \begin{bmatrix} e_2 \\ (M_p + M_t)^{-1}(-K_p e_1 - (D_p + D_t)e_2 + F_{\text{ts}}(e_1)) \end{bmatrix}$$

$$B_0 = -A_1 A_{2s}^{-1} B_2 = \begin{bmatrix} 0 \\ T(M_p + M_t)^{-1} \end{bmatrix}$$

The nonlinear cost function of (2.6) is adjusted based on the defined slow state and (4.3) into

$$J_s = \int_0^\infty \left[p_0(e_s) + 2 s_0^T(e_s) u_s + u_s^T R_0(e_s) u_s \right] dt \tag{4.5}$$

where

$$p_0(e_s) = p(e_s) - s^T A_{2s}^{-1} a_2(e_s) + a_2^T(e_s) A_{2s}^{-T} Q_z A_2^{-1} a_2(e_s),$$
$$s_0(e_s) = B_2^T A_{2s}^{-T}(Q_z A_{2s}^{-1} a_2(e_s) - \frac{1}{2} s(e_s)),$$
$$R_0 = R + B_2^T A_{2s}^{-T} Q_z A_{2s}^{-1} B_2.$$

For our purposes, we will define $s(e_s)$ as a vector of zeros to reduce the number of design parameters of the system. The slow subsystem (4.4) and cost function (4.5) combine to create the slow HJB equation

$$0 = \min_{u_s} \left[p_0(e_s) + 2 s_0^T(e_s) u_s + u_s^T R_0 u_s + \frac{\partial V_s}{\partial e_s}(a_0(e_s) + B_0 u_s) \right]. \tag{4.6}$$

The control u_s minimizing (4.6) is described as

$$u_s = -R_0^{-1}(s_0(e_s) + \frac{1}{2} B_0^T \frac{\partial V_s}{\partial e_s}^T). \tag{4.7}$$

This u_s expression is then used to create the slow subsystem HJB expression of

$$0 = p_0(e_s) - s_0(e_s)^T R_0^{-1} s_0(e_s) + \frac{\partial V_s}{\partial e_s}(a_0(e_s) - B_0 R_0^{-1} s_0(e_s)) - \frac{1}{4} \frac{\partial V_s}{\partial e_s} B_0 R_0^{-1} B_0^T \frac{\partial V_s}{\partial e_s}^T, \tag{4.8}$$

where $V_s(0) = 0$. Thanks to singular perturbation analysis, we can see that (4.8) has six unknown variables compared to the twelve unknowns of (2.9). Towards solving (4.8), we will follow the approach described in [54]. By considering $V_s = e_s^T P_s e_s$ and $\frac{\partial V_s}{\partial e_s} = e_s^T P_s$, we can ultimately construct the Riccati equation

$$P_s A_0 + A_0^T P_s = -Q_e. \tag{4.9}$$

From there, symmetric P_s can be solved for allowing for our slow controller to be represented as

$$u_s = -R_0^{-1}(s_0(e_s) + \frac{1}{2} B_0^T P_s e_s). \tag{4.10}$$

Assumption 4.2.1. *For all $e_s \in D$, (4.6) has a unique differentiable positive-definite solution $V_s(e_s)$ with the property that positive constants k_1, k_2, k_3, k_4 exist such that*

$$\begin{aligned} &k_1 \tfrac{\partial V_s}{\partial e_s} \tfrac{\partial V_s}{\partial e_s}^T \leq -\tfrac{\partial V_s}{\partial e_s} \bar{a}_0 \leq k_2 \tfrac{\partial V_s}{\partial e_s} \tfrac{\partial V_s}{\partial e_s}^T, \\ &k_3 \bar{a}_0^T \bar{a}_0 \leq -\tfrac{\partial V_s}{\partial e_s} \bar{a}_0 \leq k_4 \bar{a}_0^T \bar{a}_0, \end{aligned} \tag{4.11}$$

where

$$\dot{e}_s = a_0(e_s) - B_0 R_0^{-1}(s_0 + \frac{1}{2} B_0^T \frac{\partial V_s}{\partial e_s}^T) = \bar{a}_0(e_s).$$

Adapted from [31], it can be determined that $V_s(e_s)$ can be used as a Lyapunov function guaranteeing asymptotic stability of $e_s = 0$ for the feedback system $\bar{a}_0(e_s)$. We verify this assumption by performing the norm estimation of (4.11) using our simulation parameters in Appendix B.

4.2.2 Nonlinear Fast Sub-problem

Because the vibrational forces are expected to resonate to zero significantly faster than the cantilever positioning, the slow variable e can be stretched along a time scale τ and the fast system equilibrium can be shifted to the origin. This results in the fast subsystem to be represented as

$$\frac{dz_f}{d\tau} = A_2 z_f + B_2 u_f, \tag{4.12}$$

where

$$z_f = z - z_s = z + A_{2s}^{-1}(a_2(e_s) + B_2 u_s) \tag{4.13}$$

The fast control problem follows a linear regulator problem and is presented as the cost function

$$J_f = \int_0^\infty \left[z_f^T Q_z z_f + u_f^T R u_f \right] dt. \tag{4.14}$$

The optimal solution designed to satisfy the above cost function is

$$u_f = -R^{-1} B_2^T P_f z_f, \tag{4.15}$$

where symmetric, positive-definite P_f is the Riccati equation solution of

$$0 = P_f A_2 + A_2^T P_f + Q_z - P_f B_2 R^{-1} B_2^T P_f \tag{4.16}$$

Its Lyapunov function follows that previously mentioned in (3.23). For implementation purposes of the above fast sub-problem, z_f is to be replaced with $z - z_s$. The stability of the fast subsystem can be represented as the controllability expression shown in the following assumption.

Assumption 4.2.2. *For every fixed $e \in D$,*

$$rank[B_2, A_2B_2, \ldots, A_2^5B_2] = 6. \tag{4.17}$$

We verify this assumption using our simulation parameters in Appendix B.

4.2.3 Nonlinear Composite Controller

According to singular perturbation theory, a composite controller consisting of (4.7) and (4.15) for the system is taken as

$$\begin{aligned} u_c = \gamma(e,z) = u_s + u_f = -R_0^{-1}(s_0(e) + \frac{1}{2}B_0^T P_s^T e) \\ -R^{-1}B_2^T P_f(z + A_2^{-1}a_2(e) - A_2^{-1}B_2R_0^{-1}(s_0(e) + \frac{1}{2}B_0^T P_s^T e)). \end{aligned} \tag{4.18}$$

The purpose of this work is to create a composite controller that consists of a combination of a slow and fast controller designed to control each subsystem making up the complete system. This controller is based on feedback of our error states e and vibrational forces z to control their defined slow and fast sub-problems. Instead of solving for the optimal value of u in (2.6), the solutions to the defined slow and fast sub-problems construct near-optimal u_c which defines composite cost function

$$J_c = \int_0^\infty \left[p(e) + s^T(e)z + z^TQz + u_c^TRu_c\right] dt. \tag{4.19}$$

The performance of the composite controller u_c is considered near optimal because it allows for the optimization of the composite cost (4.19) to approach the slow sub-problem cost (4.5) as ϵ approaches zero. To verify this statement, we have the following theorem.

Theorem 4.2.1. *For all initial conditions e_0 and z_0 that belong to a sufficiently small set $D \in \mathbb{R}^{12}$, the near-optimal control* (4.18) *leads to*

$$J_c(e, z) - V_s(e) = 0, \quad as \ \epsilon \to 0, \tag{4.20}$$

This theorem follows that of Corollary 7.1 from Chapter 7 of [33] but is extended to our work. The referenced Corollary and our corresponding theorem is satisfied by verifying a series of assumptions. Assumptions 7.1 through 7.4 of [33] establish a collection of bounds for which our system and corresponding nonlinear controller must be contained by. For our application, our near-optimal feedback design satisfies these assumptions. Equations and graphs validating these assumptions can be viewed in Appendix A.

The system, including its near-optimal feedback controller, is deemed asymptotically stable given the following theorem [31].

Theorem 4.2.2. *If Assumptions 2.3.1, 4.2.1, and 4.2.2 are satisfied, there exists an $\epsilon^* > 0$ such that the equilibrium $e = 0$, $z = 0$ of* (2.11) *is asymptotically stable for all $\epsilon \in (0, \epsilon^*]$.*

Given a system that satisfies stability assumptions across the system's cost function, slow subsystem, and fast subsystem, the theorem states that the system is asymptotically stable if the value of ϵ is within the range of zero to ϵ^*. The value of ϵ^* consists of an expression of which its values are determined by a series of equations [33]. For our application, the verification of Theorem 4.2.1 using our chosen value of ϵ demonstrates that our ϵ is within the range outlined by Theorem 4.2.2.

In discussing our proposed controller (4.18) and near-optimality expression (4.20), near-optimality for our controller refers to how the control objective steers the system towards the solution of the slow subsystem outlined by its cost function 4.5. This is represented by the chosen value of small parameter ϵ and how such a small parameter approaches zero adjusts our system (2.11) to consist of only of the slow subsystem (4.4). However, achieving near-optimal control within Theorems 4.2.1 grantees that the states are bounded.

4.3 Nonlinear Near-optimal Simulations

With the equations and controllers defined, simulations were conducted to demonstrate the system's performances. The goal of this controller is to perform better or similarly to that of the linear near-optimal controller from the previous chapter. The parameters and initial conditions used in our simulation are the same as those seen in Table 3.1 and 3.2 respectively from the linear near-optimal control section. Our design parameters for the nonlinear near-optimal controller are presented in Table 4.1. Because the cantilever cannot be made infinitely stiff, $\epsilon = 0.1$ for the simulations referencing a stiffness of $k_{ti} = 100N/m$.

Fig. 4.1 demonstrates the control performance of the cantilever tip when compared to their desired raster scanning trajectories. Vertical position control of the cantilever tip towards the interaction force equilibrium point z_b is shown in Fig. 4.1c. The tip velocities are shown to approach their desired performance in Fig. 4.2. The center of the piezotube at which is attached to the cantilever is shown to be driven to the same position and velocity trajectories of the cantilever in Fig. 4.3 and Fig. 4.4. The cantilever vibrational forces as the tip moves across the sample is presented in Fig. 4.5. The vibrational overshoot shown in the z-axis of Fig. 4.5c results from the changing interaction forces and is mitigated as these forces approach equilibrium. This is shown in Fig. 4.6 where the vibrations are quickly resolved by being brought to zero. The error dynamics that drive our nonlinear controller are shown to be brought to zero as well in Fig. 4.7 and Fig. 4.8 The control effort of Fig. 4.9 is shown to be reasonably bounded to generate the desired piezotube adjustments to efficiently steer the cantilever. The total nonlinear interaction force impacting our system can be seen to be driven to zero in Fig. 4.10 by bringing the cantilever tip to the equilibrium point. It can be seen from these figures that the controller was successfully able to drive the cantilever to follow desired lateral conditions and bring the cantilever tip to the interaction force equilibrium point. A comparison across reasonably valued epsilons can be seen controlling the tip in Fig. 4.11. By making epsilon immensely small, the cantilever is more resistive to oscillate from inputs and interaction forces.

Table 4.1: Nonlinear near-optimal design parameters

Symbol	Numerical Value
ϵ	0.1
q_{e_1}	1.1988×10^{15}
q_{e_2}	7.5×10^{5}
q_{z_1}	1×10^{16}
q_{z_2}	1×10^{7}
r_i	1

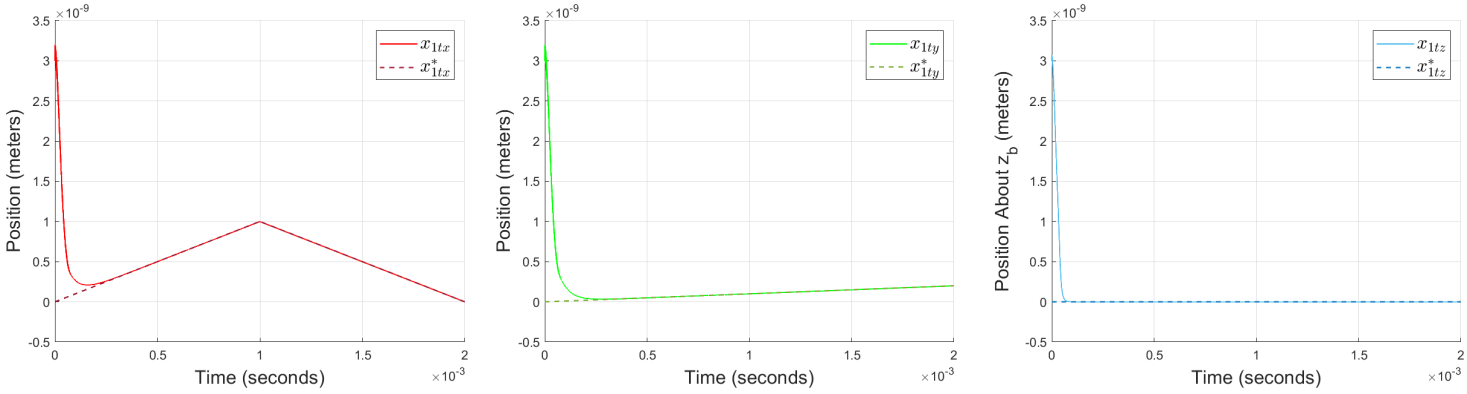

(a) X-axis tip position (b) Y-axis tip position (c) Z-axis tip position

Figure 4.1: Nonlinear near-optimal control x_{1t} performance

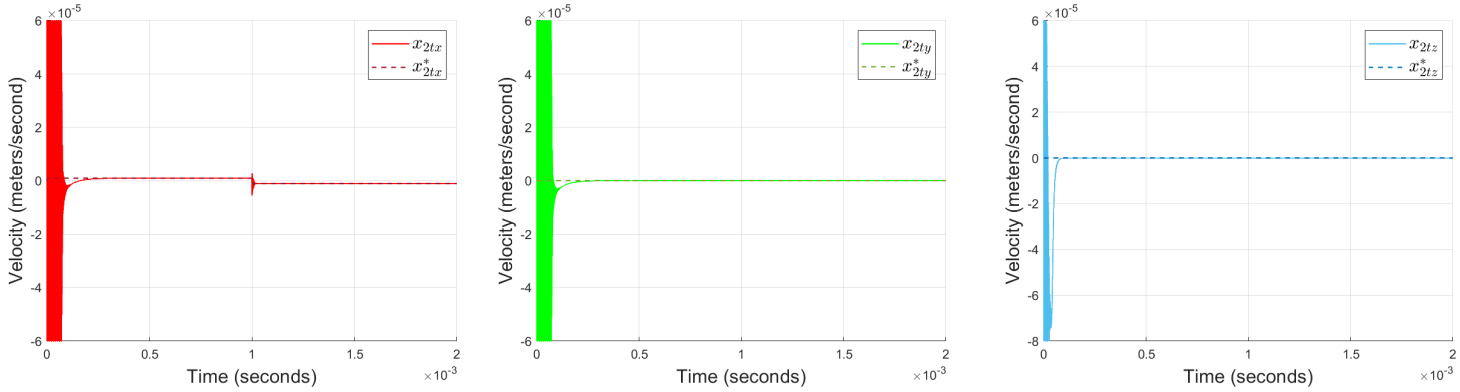

(a) X-axis tip velocity (b) Y-axis tip velocity (c) Z-axis tip velocity

Figure 4.2: Nonlinear near-optimal control x_{2t} performance

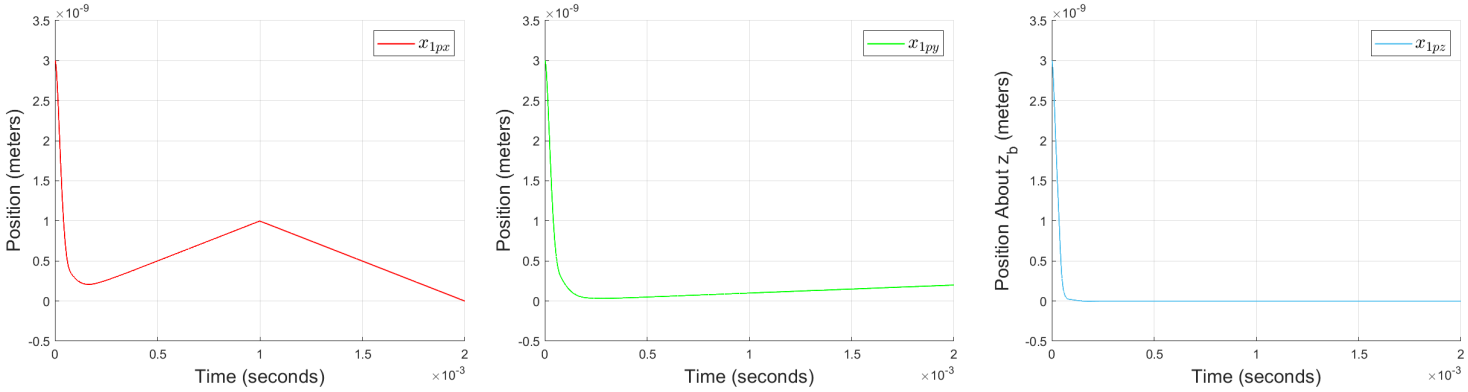

(a) X-axis piezotube position (b) Y-axis piezotube position (c) Z-axis piezotube position

Figure 4.3: Nonlinear near-optimal control x_{1p} performance

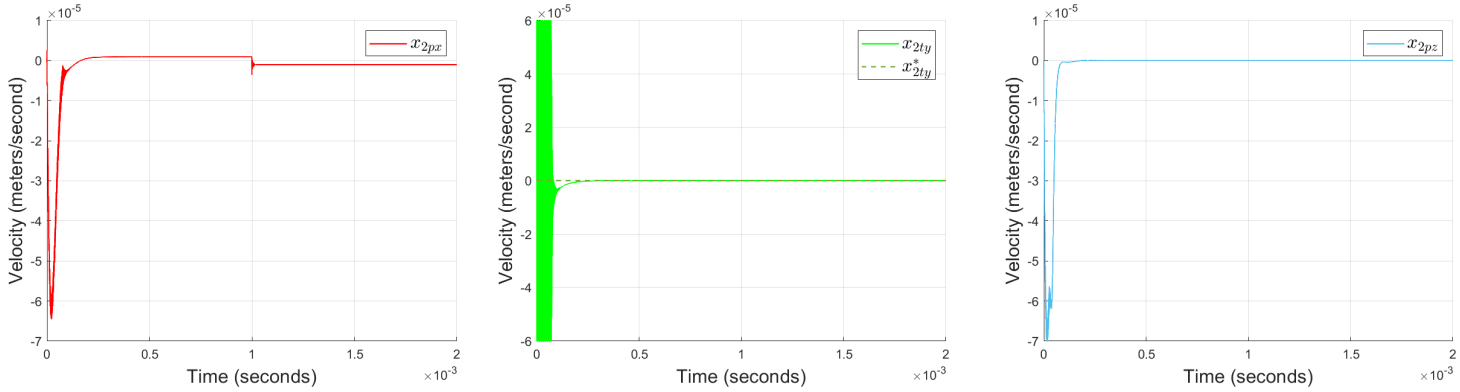

(a) X-axis piezotube velocity (b) Y-axis piezotube velocity (c) Z-axis piezotube velocity

Figure 4.4: Nonlinear near-optimal control x_{2p} performance

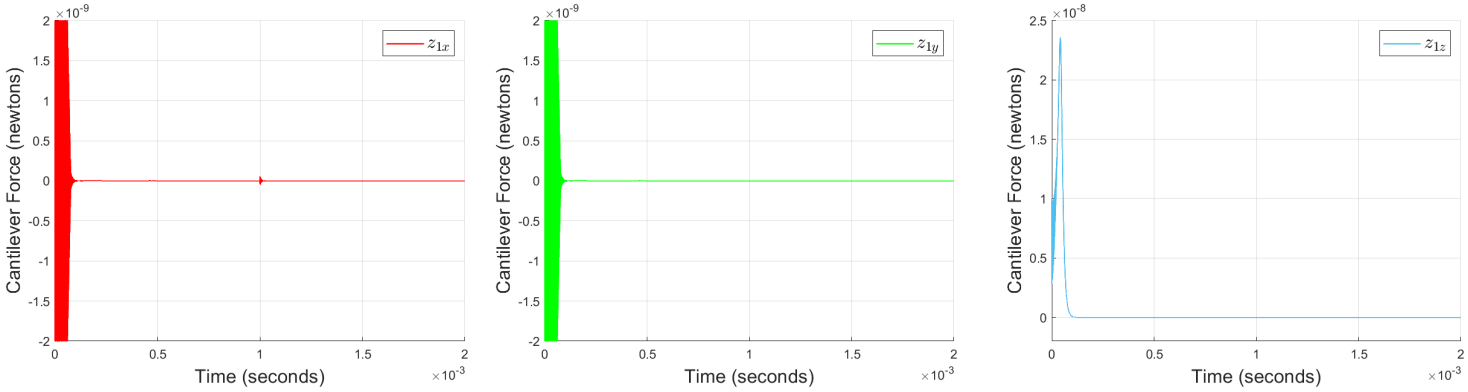

(a) X-axis vibrational force (b) Y-axis vibrational force (c) Z-axis vibrational force

Figure 4.5: Nonlinear near-optimal control z_1 performance

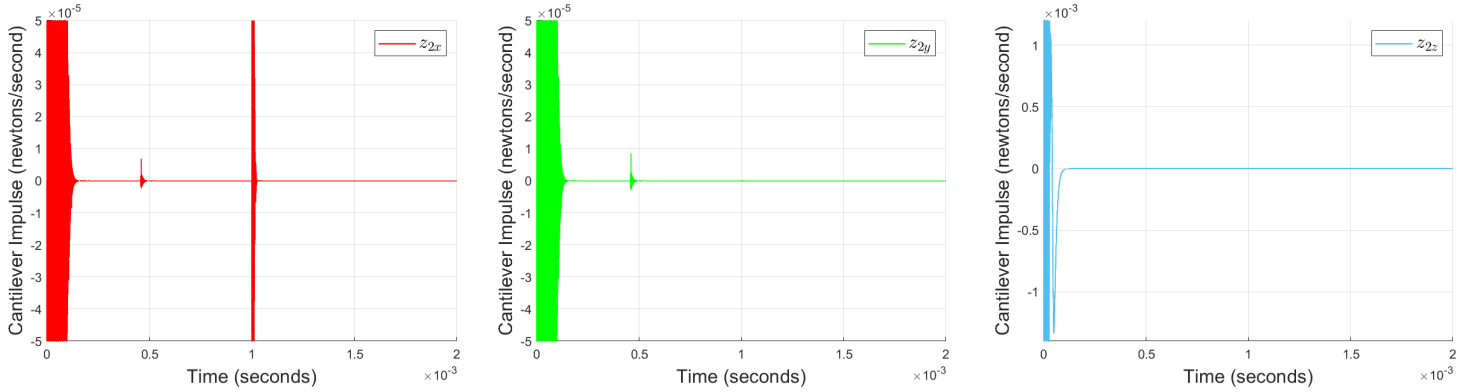

(a) X-axis vibrational impulse (b) Y-axis vibrational impulse (c) Z-axis vibrational impulse

Figure 4.6: Nonlinear near-optimal control z_2 performance

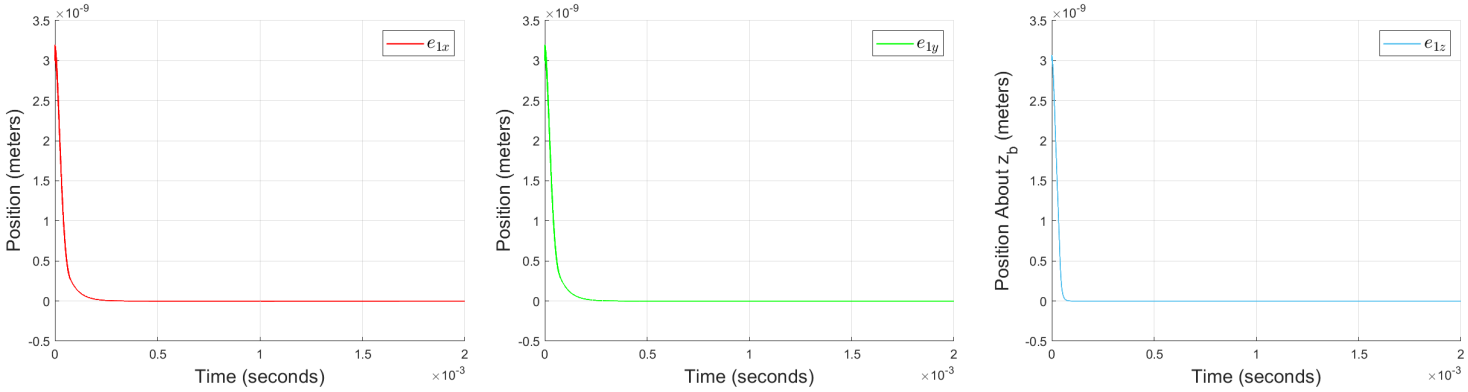

(a) X-axis tip position error (b) Y-axis tip position error (c) Z-axis tip position error

Figure 4.7: Nonlinear near-optimal control e_1 performance

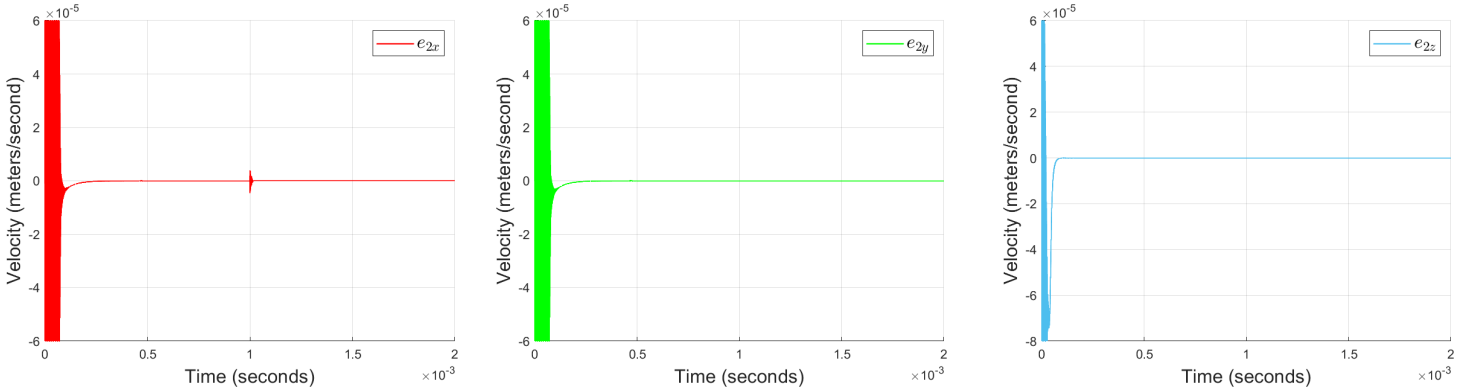

(a) X-axis tip velocity error (b) Y-axis tip velocity error (c) Z-axis tip velocity error

Figure 4.8: Nonlinear near-optimal control e_2 performance

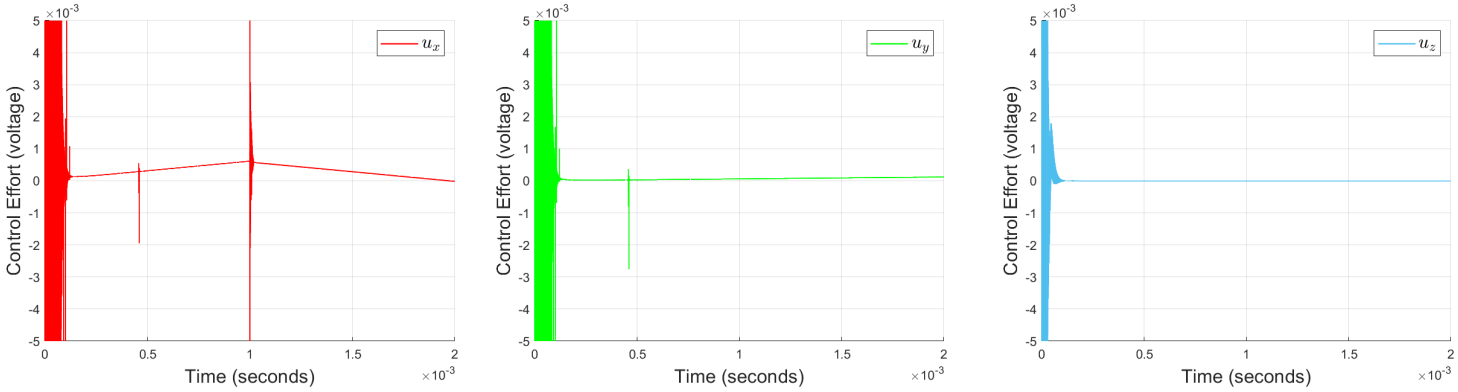

(a) X-axis control effort (b) Y-axis control effort (c) Z-axis control effort

Figure 4.9: Nonlinear near-optimal control u control effort

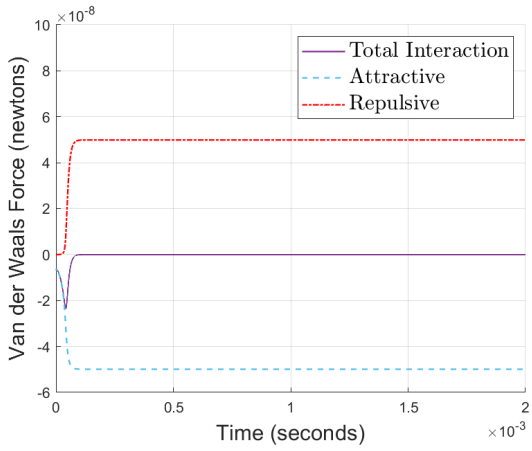

Figure 4.10: Interaction forces affecting the nonlinear near-optimal controller

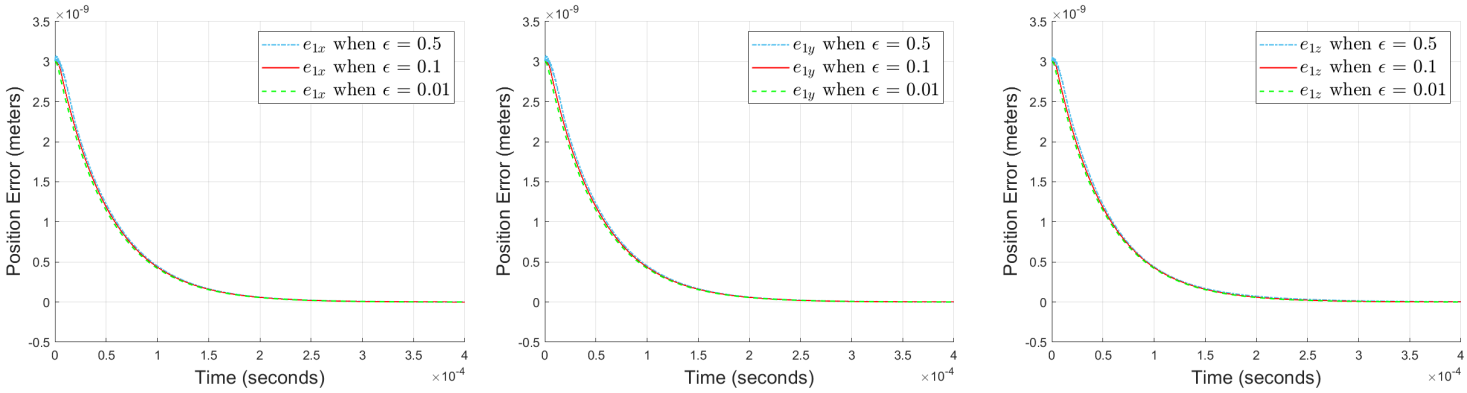

(a) X-axis tip position error (b) Y-axis tip position error (c) Z-axis tip position error

Figure 4.11: Nonlinear near-optimal control e_1 performance across varying epsilon

4.4 Linear, Nonlinear, and PD Controller Comparison

Other works have designed different controllers to solve the general AFM control problem. Proportional Derivative (PD) controllers [29] and approximated optimal linear feedback controllers [13] have been previously constructed and have produced their own results. Our work is different from the results portrayed in these works, as the proposed control system benefits

from the stiff cantilever to simplify the nonlinear control problem into two smaller problems. This simplification prevents the need to assume linearity in the design of a feedback controller.

A comparison between our linear and nonlinear controllers and a PD controller can be seen in Fig. 4.12 to compare the cantilever tip control performance. PD is a commonly used controller in industry, but it can be challenging to implement for systems with dimensions larger than two. The PD controller used in our simulation follows a similar structure to [29] using composite control $u_c = u_s + u_f$ where

$$u_s = K_{p_e} e_1 + K_{d_e} e_2, \quad u_f = K_{p_z} z_1 + K_{d_z} z_2, \tag{4.21}$$

and K_{p_e}, K_{d_e}, K_{d_z}, and K_{d_z} are diagonal gain matrices. The controller gains are tuned so that we can get the best possible performance. It can be seen from Fig. 4.12 that, despite our efforts to tune the PD controller gains for the best performance, the near optimal controller achieves a superior performance without the need for tuning.

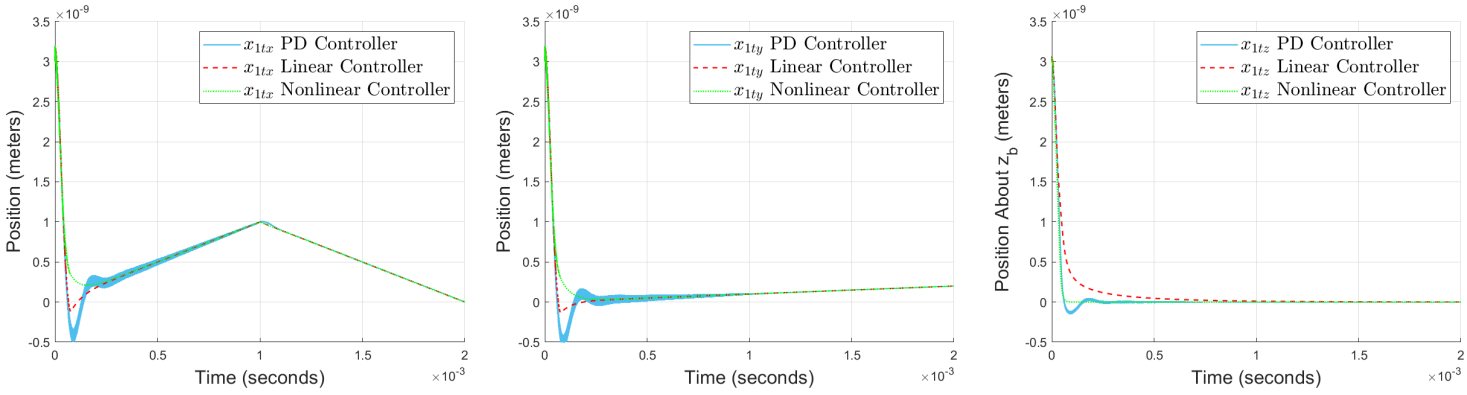

(a) X-axis tip position (b) Y-axis tip position (c) Z-axis tip position

Figure 4.12: Controller comparison evaluating x_{1t} performance

Of the shown figures, it can be recognized that the near-optimal linear and nonlinear controllers both operate and perform similarly. This makes sense for the x-axis and y-axis, as the nonlinearity aspects of the AFM system significantly affect the z-axis. The main differences

between the near-optimal linear and nonlinear controllers come from the z-axis vibration force and impulse mitigation and oscillations found from smaller epsilon comparisons. Another notable difference is in the cantilever tip performance, as the tip encountered overshoot and a longer settling time. The near-optimal nonlinear controller can be demonstrated to be better than the linear controller for these instances because the nonlinear controller was able to smoothly handle the vibrational discrepancies and operate better for smaller, more reasonable, valued epsilons. This conclusion makes sense, as nonlinear controllers are viewed as global controllers because of their ability to handle more aspects of the system. In the next chapter, we will design observers to find state estimates, along with an estimated disturbance, and apply these estimates into our nonlinear controller.

Chapter 5

Nonlinear Observer Design

5.1 Cascaded Extended High-Gain Observers

A high-gain observer (HGO) is designed to quickly bring state estimates to their measured counterparts. We chose to design a HGO because it has a number of advantages that we will show in simulations

- They are robust to system uncertainties.
- They produce fast responses.
- They recover state feedback performance.
- There are no differential equations to solve for their formulations, making them simple to design.

Most importantly, the design of a HGO satisfies the separation principle which allows us to apply its estimates into an optimal or near-optimal controller [42]. This allows for us to use the estimates produced by a HGO for output feedback. These observers are also beneficial for measuring time-varying nonlinear dynamics where disturbances are involved and when a

control scheme is needed that is robust against both a leader's and a followers' heterogeneous uncertain time-varying nonlinear dynamics and external disturbances [49]. Given a system following the formulation of

$$\begin{aligned} \dot{x} &= Ax + g(y, u), \\ y &= Cx, \end{aligned} \tag{5.1}$$

where (A, C) is observable, a HGO can be constructed as the following

$$\dot{\hat{x}} = A\hat{x} + g(y, u) + H(y - C\hat{x}), \tag{5.2}$$

where $\hat{x}$ is the state estimate of x [54]. This HGO's objective is to bring state estimate $\hat{x}$ to the actual state value of x relatively quickly. This quick determination can allow a system to track large sudden variations typically seen in nonlinear functions.

An extended high-gain observer (EHGO) follows that of a regular high-gain observer, but a new state is extended to the system's state vector to represent the system's disturbance. This new state is designed to converge faster than the actual state estimates. When the system is in the canonical form and is observable, an EHGO can be constructed. An EHGO follows the formulation of

$$\begin{aligned} \dot{\hat{x}}_1 &= x_2 + \frac{\alpha_1}{\epsilon_h}(y - \hat{x}), \\ \dot{\hat{x}}_2 &= \hat{\sigma} + \hat{a}(\hat{x}) + \hat{b}(\hat{x})u + \frac{\alpha_2}{\epsilon_h^2}(y - \hat{x}), \\ \dot{\hat{\sigma}} &= \frac{\alpha_3}{\epsilon_h^3}(y - \hat{x}), \end{aligned} \tag{5.3}$$

where σ is designed to represent disturbances imposed onto the system [55]. Design constraints for an EHGO require that ϵ_h is chosen as a small parameter such that $0 < \epsilon_h < 1$ and the chosen α_1 to α_3 allow for polynomial

$$s^3 + \alpha_1 s^2 + \alpha_2 s + \alpha_3,$$

to be Hurwitz [49]. Because ϵ_h is made to be smaller for each increasing derivative state, this allows for relatively quick convergence for each estimated state due to each state's derivative being determined sooner than the state itself.

When the order of a system is large, a cascaded "full-order" observer uses lower-ordered observers to estimate higher derivatives of the system [43]. This can be done if a set of states of a system are dependent linearly on another set of states where both sets are in the chain of integrator form. An example implementation of a cascaded observer is as follows. Given a system of equations represented as

$$\begin{aligned}
\dot{\eta}_1 &= \eta_2, \\
\dot{\eta}_2 &= \phi_2(\eta, \xi), \\
\dot{\xi}_1 &= \xi_2, \\
\dot{\xi}_2 &= \phi_2(\xi) + a_{\eta_1}\eta_1 + a_{\eta_2}\eta_2 + bu, \\
y &= \xi_1,
\end{aligned} \tag{5.4}$$

a cascaded observer for these states would be

$$\begin{aligned}
\dot{\hat{\xi}}_1 &= \hat{\xi}_2 + \frac{\alpha_1}{\epsilon_h^{\rho}}(y - \hat{\xi}_1), \\
\dot{\hat{\xi}}_2 &= \phi_2(\hat{\xi}) + \hat{\sigma} + a_{\eta_2}\hat{\eta}_2 + bu + \frac{\alpha_2}{\epsilon_h^{2\rho}}(y - \hat{\xi}_1), \\
\dot{\hat{\sigma}} &= a_{\eta_1}\hat{\eta}_2 + \frac{\alpha_3}{\epsilon_h^{3\rho}}(y - \hat{\xi}_1), \\
\dot{\hat{\eta}}_1 &= \hat{\eta}_2 + \frac{\beta_1}{\epsilon_h}(\hat{\sigma} - a_{\eta_1}\hat{\eta}_1), \\
\dot{\hat{\eta}}_2 &= \phi_1(\hat{\eta}, \hat{\xi}) + \frac{\beta_2}{\epsilon_h^2}(\hat{\sigma} - a_{\eta_1}\hat{\eta}_1),
\end{aligned} \tag{5.5}$$

where ϵ_h is chosen as a small parameter such that $0 < \epsilon_h < 1$ and the chosen α_1 to α_3 and β_1 to β_2 allow for polynomials

$$s^3 + \alpha_1 s^2 + \alpha_2 s + \alpha_3, \qquad s^2 + \beta_1 s + \beta_2,$$

to be Hurwitz [47]. ρ is to be chosen such that $\rho > 1$ to allow for the EHGO to evolve faster than the HGO to ensure that a reasonable value of σ is provided for the proceeding HGO. This design example allows the observer to use its $\hat{\xi}$ estimate to estimate $\hat{\eta}$ by only requiring state feedback of ξ.

For our application, two different observers are designed. The first proposed design uses state feedback x_p and x_t for a HGO that estimates $\hat{x}_p$ and an EHGO that estimates $\hat{x}_t$ and the

Van der Waals disturbances. The second design only uses state feedback of x_p for an EHGO that estimates $\hat{x}_p$ and a signal that acts as a virtual output that behaves as an input for $\hat{x}_t$ which is cascaded into another EGHO that estimates $\hat{x}_t$ and the Van der Waals disturbances. The goal of these observers is to work with the near-optimal nonlinear controller outlined in Chapter 4 for output feedback control by using the estimated states to produce similar results of that Chapter without full-state feedback knowledge.

5.2 Combined High-Gain Observer

5.2.1 Combined Observer Design

Our AFM dynamics in terms of our mass-spring-damper piezotube and cantilever dynamics are represented as

$$\begin{aligned} M_t\ddot{x}_t + D_t\dot{x}_t + K_t(x_t - x_p) &= F_{ts}(x_{1t}), \\ M_p\ddot{x}_p + D_p\dot{x}_p + K_p x_p - K_t(x_t - x_p) &= Tu. \end{aligned} \tag{5.6}$$

Based on our research, it can be assumed that x_{1p} and x_{1t} are available for state feedback [4, 36]. We wish to design our observer based on the actual AFM dynamics instead of our singular perturbation dynamics for our observer to directly perform the same operations as the actual complete AFM system. With this information in mind, our AFM dynamics can be rewritten into standard normal form as

$$\begin{aligned} \dot{x}_{1t} &= x_{2t}, \\ \dot{x}_{2t} &= M_t^{-1}(-D_t x_{2t} - K_t x_{1t} + K_t x_{1p} + F_{ts}(x_{1t})), \\ y_t &= x_{1t}, \\ \dot{x}_{1p} &= x_{2p}, \\ \dot{x}_{2p} &= M_p^{-1}(-D_p x_{2p} - K_p x_{1p} + K_t x_{1t} - K_t x_{1p} + Tu), \\ y_p &= x_{1p}, \end{aligned} \tag{5.7}$$

where $x_{1t} = x_t$, $x_{2t} = \dot{x}_t$, $x_{1p} = x_p$, and $x_{2p} = \dot{x}_p$. From these equations, it can be seen that our system is under-actuated where the actuation of the piezotube affects the tip and both

of these dynamics are in their own chain of integrator form. Given that the shape of the nonlinear Van der Waals forces $F_{ts}(x_{1t})$ acts as a disturbance, an EHGO can be designed to monitor this disturbance as a new state. For the piezotube, because we do not expect the same level of disturbances as the tip, a standard HGO design can be implemented to track its states. Following the works of [45, 55], our combined observer can be constructed as

$$\begin{aligned}
\dot{\hat{x}}_{1t} &= \hat{x}_{2t} + \frac{\beta_1}{\epsilon_h}(y_t - \hat{x}_{1t}),\\
\dot{\hat{x}}_{2t} &= M_t^{-1}(-D_t\hat{x}_{2t} - K_t\hat{x}_{1t} + K_t\hat{x}_{1p}) + \hat{\sigma} + \frac{\beta_2}{\epsilon_h^2}(y_t - \hat{x}_{1t}),\\
\dot{\hat{\sigma}} &= \frac{\beta_3}{\epsilon_h^3}(y_t - \hat{x}_{1t}),\\
\dot{\hat{x}}_{1p} &= \hat{x}_{2p} + \frac{\alpha_1}{\epsilon_h}(y_p - \hat{x}_{1p}),\\
\dot{\hat{x}}_{2p} &= M_p^{-1}(-D_p\hat{x}_{2p} - K_p\hat{x}_{1p} + K_t\hat{x}_{1t} - K_t\hat{x}_{1p} + Tu) + \frac{\alpha_2}{\epsilon_h^2}(y_p - \hat{x}_{1p}),
\end{aligned} \tag{5.8}$$

where ϵ_h is designed to be $0 < \epsilon_h < 1$ and for α_1 to α_2 and β_1 to β_3 to be chosen such that polynomials

$$s^3 + \beta_1 s^2 + \beta_2 s + \beta_3, \qquad s^2 + \alpha_1 s + \alpha_2,$$

are to be Hurwitz. The observer is designed in such a way that, despite encompassing of a HGO and an EHGO, both the piezotube and tip estimates evolve at that same rates. This is important because the estimates of both of our observers directly contribute to each other. If one observer was designed to operate faster than the other, instability between them may ensue. Following this statement, our α and β design parameters are to be selected such that the eigenvalues from their respective polynomials for α_1 and β_1 and α_2 and β_2 respectively to match. Our chosen design values can be seen in Table 5.1.

Table 5.1: Combined high-gain observer design parameters

Symbol	Numerical Value
ϵ_h	1×10^{-10}
α_1	3
α_2	2
β_1	6
β_2	11
β_3	6

Along with our observer equations, estimated versions of our state error e and singular perturbated vibrational force z need to be created to match the outline of our controller. These estimated versions follow that of their initial formulations but with their estimated counter parts. The resulting expressions are

$$\begin{aligned} \hat{e}_1 &= \hat{x}_{1t} - x^*_{1t} \\ \hat{e}_2 &= \hat{x}_{2t} - x^*_{2t} \\ \hat{z}_1 &= K_t(\hat{x}_{1p} - \hat{x}_{1t}) \\ \hat{z}_2 &= K_t(\hat{x}_{2p} - \hat{x}_{2t}) \end{aligned} \tag{5.9}$$

With our combined observer and these expressions defined, we will create an output feedback controller.

5.2.2 Output Feedback Control of Combined Observer

We will begin our control design by replacing the states of our state feedback near-optimal controller of Chapter 4. With our state estimates of (5.8) and (5.9) defined, our output

feedback controller of (4.18) becomes

$$\begin{aligned}\hat{u}_c = \gamma(\hat{e},\hat{z}) = sat(&-R_0^{-1}(\hat{s}_0 + \frac{1}{2}B_0^T P_s^T \hat{e}) \\ &-R^{-1}B_2^T P_f(\hat{z} + A_2^{-1}\hat{a}_2 - A_2^{-1}B_2 R_0^{-1}(\hat{s}_0 + \frac{1}{2}B_0^T P_s^T \hat{e})))\end{aligned} \tag{5.10}$$

where

$$\hat{a}_2 = \begin{bmatrix} 0 \\ -\sigma_{e_1}\hat{e}_1 + \sigma_{e_2}\hat{e}_2 - \sigma_{F_{ts}}\sigma \end{bmatrix}$$
$$\hat{s}_0(e_s) = B_2^T A_{2s}^{-T} Q_z A_{2s}^{-1}\hat{a}_2,$$

This expression is the same of that formulated for (4.18), but uses the estimates from our combined observer as the provided states. It is also worth noting that the previously known Van der Waals nonlinearity $F_{ts}(x_{1t})$ in the controller is replaced with the observed σ disturbance estimate. This important change allows our observer to estimate this interaction force and thus apply this estimate into our controller. This is a significant contribution, as the Van der Waals forces can be difficult to accurately predict and can continuously change based on overtime wear of the tip [56]. Along with this, our output feedback controller is also saturated to reduce the peaking phenomena commonly occurred in HGOs. The saturation parameters are defined based on the range of input values seen from full state feedback of Chapter 4, namely Fig. 4.9.

Explanation as to how our combined observer maintains near-optimality for our closed-loop system despite using estimated values in output feedback can be explained following similar a similar approach to the more complex cascaded observer design in the following section.

5.2.3 Combined Observer Simulations

The simulations below were conducted using the output feedback controller described by (5.10) of which the combined observer (5.8) produces state estimates from the outputs of the system (5.7) using $\hat{u}_c$ instead of u. The initial conditions of the system match those previously defined by Table 3.2. Our observer's state estimate initial conditions were all set

to 0 for our simulations. The high-gain of our observer allows for our estimated states to quickly find and match their actual state counterparts.

The simulated figures below demonstrate our combined observer and output feedback control's ability to bring state estimates to the actual states of the system. Of the produced figures, some important characteristics can be seen. The control effort generated by (5.10) can be seen to be fairly smooth caused by the high-gain pressuring the observer to keep its states matched with the states of the actual AFM system. The observed disturbance σ_z can be seen in Fig. 5.11c which successfully matches the Van der Waals total interaction force experienced by the system of 5.10.

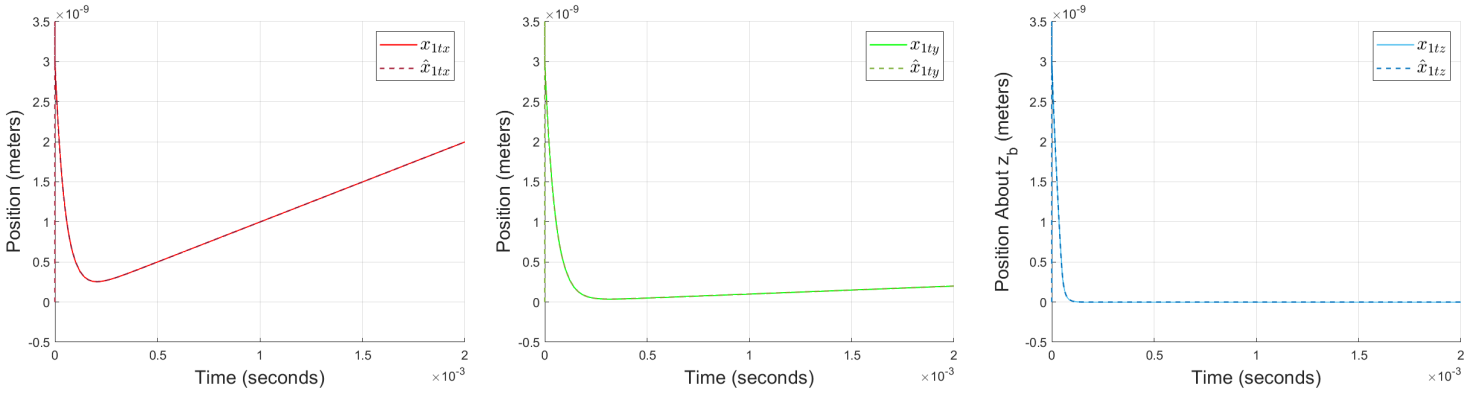

(a) X-axis tip position (b) Y-axis tip position (c) Z-axis tip position

Figure 5.1: Combined observer output feedback control x_{1t} performance

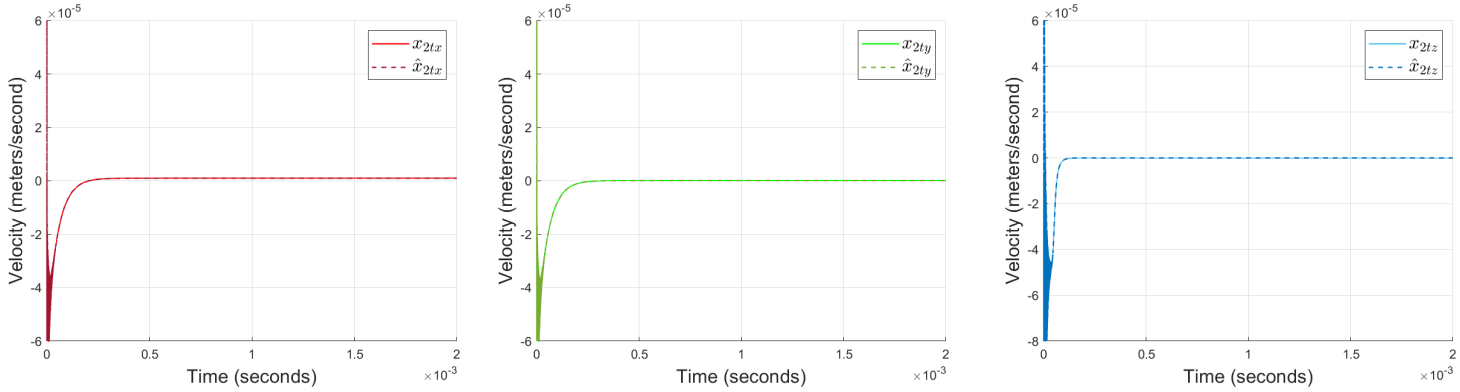

(a) X-axis tip velocity (b) Y-axis tip velocity (c) Z-axis tip velocity

Figure 5.2: Combined observer output feedback control x_{2t} performance

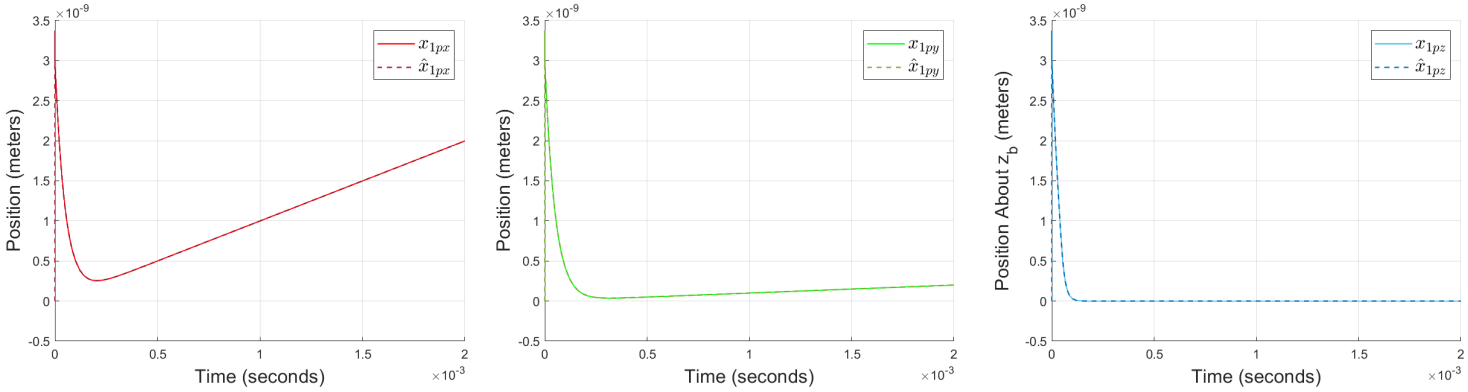

(a) X-axis piezotube position (b) Y-axis piezotube position (c) Z-axis piezotube position

Figure 5.3: Combined observer output feedback control x_{1p} performance

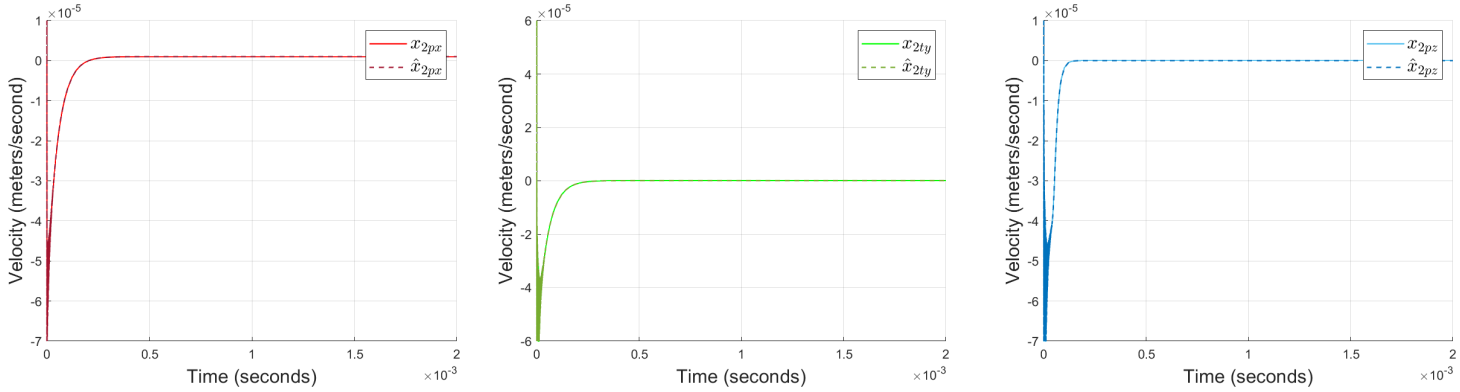

(a) X-axis piezotube velocity (b) Y-axis piezotube velocity (c) Z-axis piezotube velocity

Figure 5.4: Combined observer output feedback control x_{2p} performance

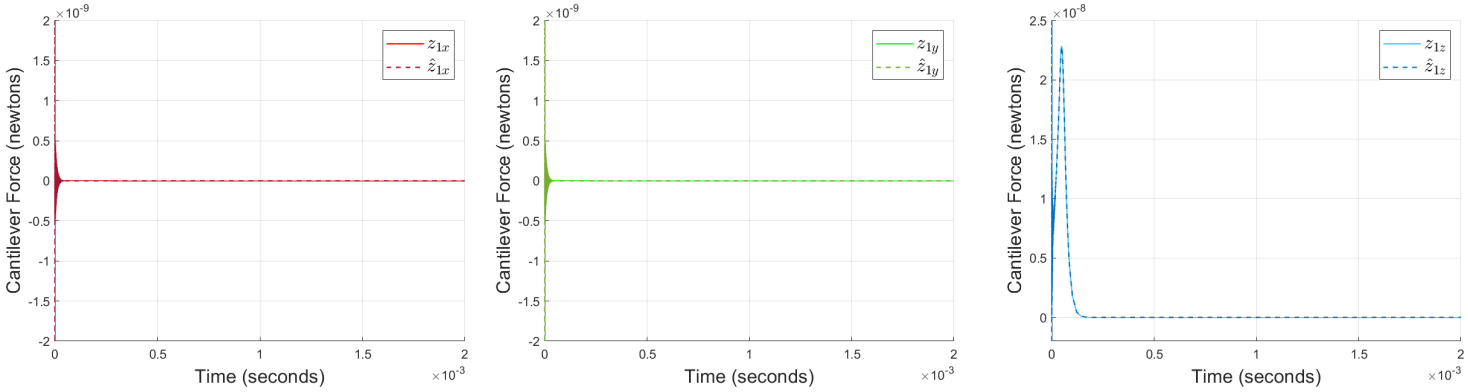

(a) X-axis vibrational force (b) Y-axis vibrational force (c) Z-axis vibrational force

Figure 5.5: Combined observer output feedback control z_1 performance

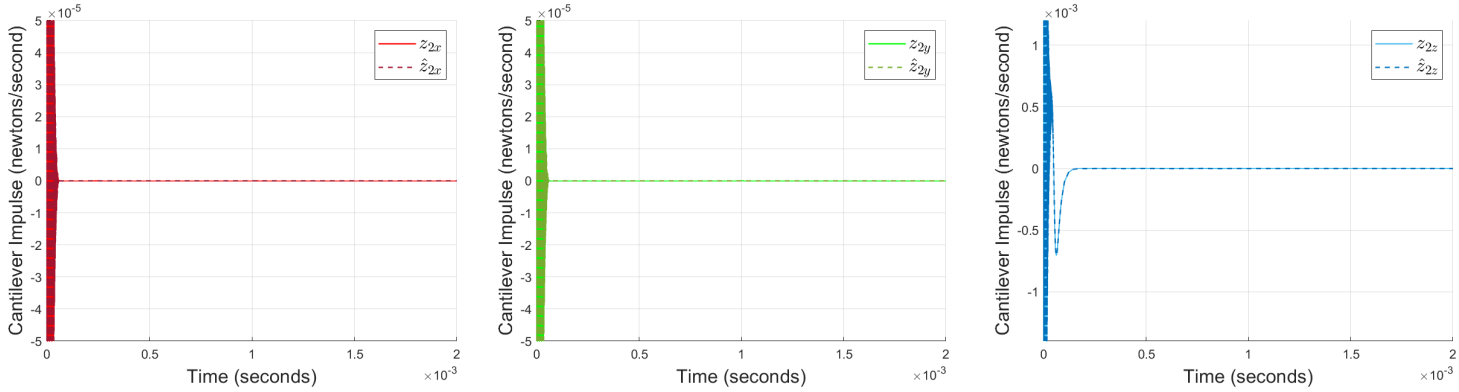

(a) X-axis vibrational impulse (b) Y-axis vibrational impulse (c) Z-axis vibrational impulse

Figure 5.6: Combined observer output feedback control z_2 performance

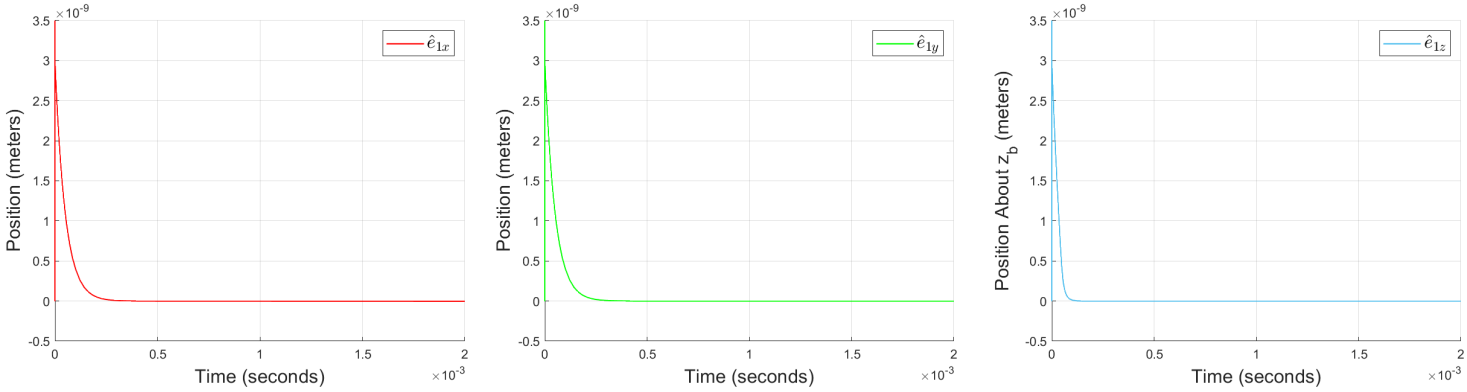

(a) X-axis tip position error (b) Y-axis tip position error (c) Z-axis tip position error

Figure 5.7: Combined observer output feedback control e_1 performance

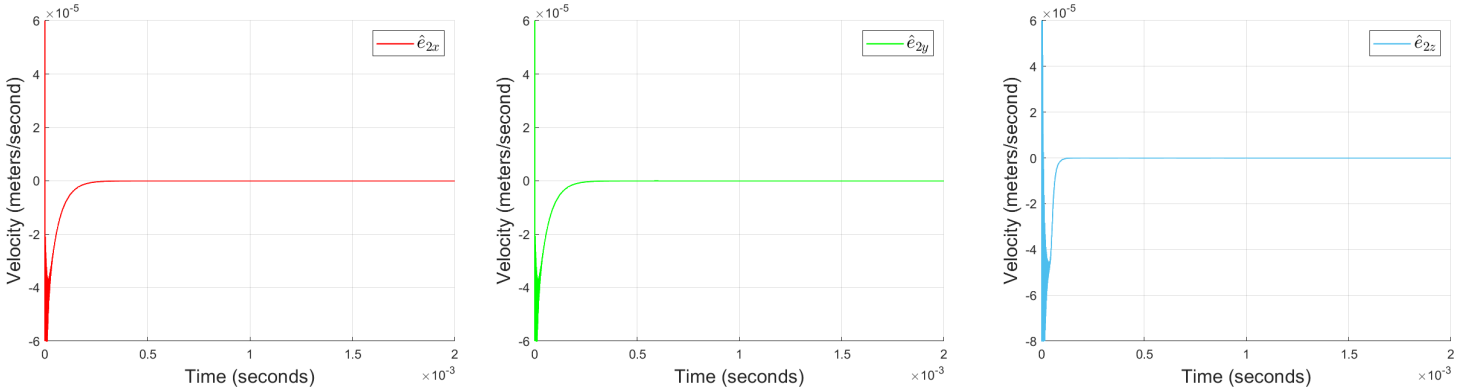

(a) X-axis tip velocity error (b) Y-axis tip velocity error (c) Z-axis tip velocity error

Figure 5.8: Combined observer output feedback control e_2 performance

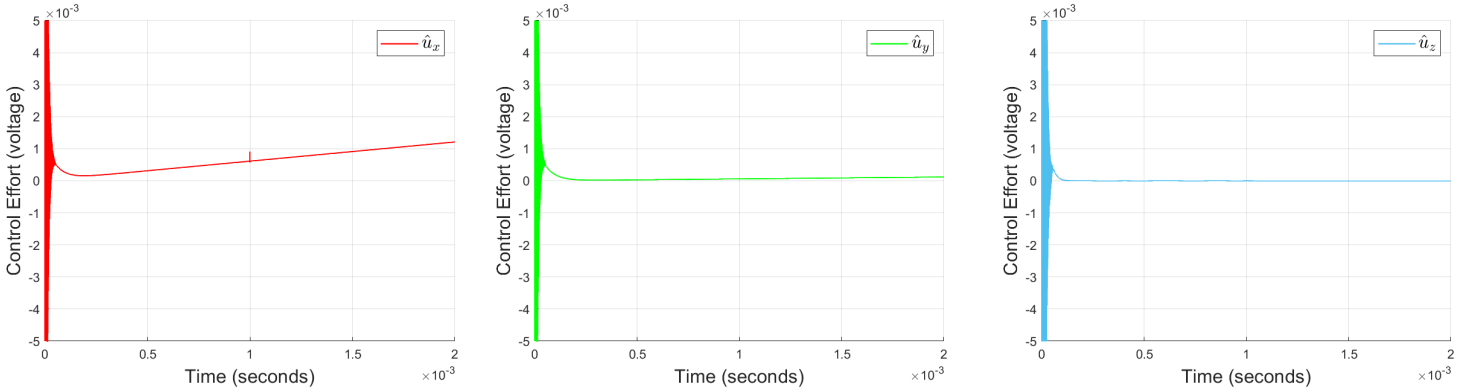

(a) X-axis control effort (b) Y-axis control effort (c) Z-axis control effort

Figure 5.9: Combined observer output feedback control u control effort

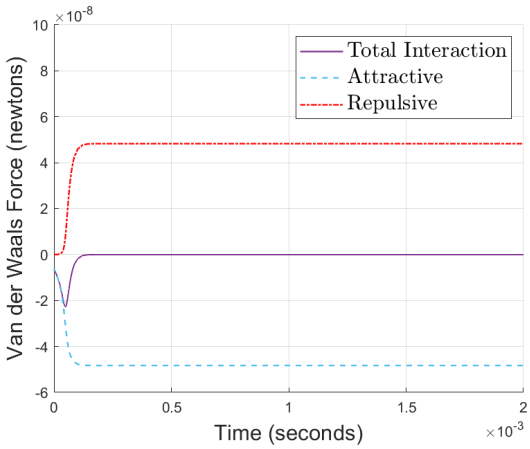

Figure 5.10: Interaction forces affecting the nonlinear near-optimal controller

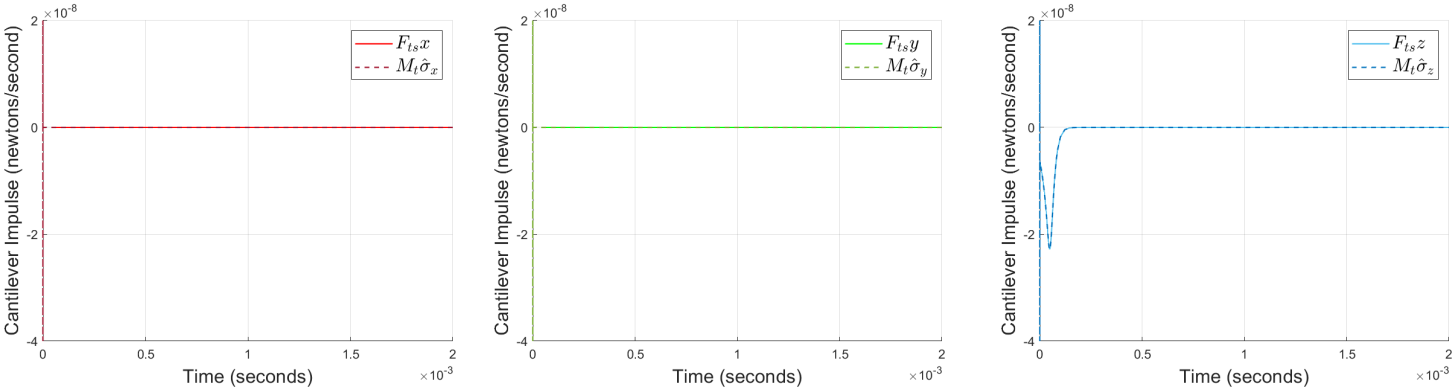

(a) X-axis disturbance (b) Y-axis disturbance (c) Z-axis disturbance

Figure 5.11: Combined observer output feedback control σ estimated disturbance

Despite our combined observer producing satisfactory results, we wish to continue our observer design efforts for reduced number of state feedback parameters. In the next section, we will design a cascaded extended high-gain observer to estimate the AFM dynamics when only x_{1p} is measurable.

5.3 Cascaded Extended High-Gain Observer

5.3.1 Cascaded Observer Design

For the AFM dynamics previously described by (5.6), we can continue improving our observer design to reduce the number of states for state feedback. Because of the amount of equipment and extra control functions needed to maintain the laser deflection measurement system to monitor the position of the AFM cantilever tip x_{1t}, we will design an observer using only the measurements of the piezotube x_{1p}. This design choice will effectively reduce the cost of the AFM and simplify the overall control design, as the AFM tip is difficult to measure with the elaborate laser deflection technology. As a result, our AFM dynamics are rewritten into the standard normal form of

$$\begin{aligned}
\dot{x}_{1t} &= x_{2t}, \\
\dot{x}_{2t} &= M_t^{-1}(-D_t x_{2t} - K_t x_{1t} + K_t x_{1p} + F_{ts}(x_{1t})), \\
\dot{x}_{1p} &= x_{2p}, \\
\dot{x}_{2p} &= M_p^{-1}(-D_p x_{2p} - K_p x_{1p} + K_t x_{1t} - K_t x_{1p} + Tu), \\
y_p &= x_{1p}.
\end{aligned} \tag{5.11}$$

Because our equations represent an under-actuated system where only the state of the actuated piezotube dynamics are available for state feedback, a cascaded observer is ideal. However, the unknown Van der Waals disturbances appear in the under-actuated tip dynamics. It is known from the previous section that an EHGO can monitor the disturbances of a system in canonical form as an extra state. Thus, a cascaded observer of two EHGOs

is formed as

$$
\begin{aligned}
\dot{\hat{x}}_{1p} &= \hat{x}_{2p} + \frac{\alpha_1}{\epsilon_h^{\rho}}(y_p - \hat{x}_{1p}),\\
\dot{\hat{x}}_{2p} &= M_p^{-1}(-D_p\hat{x}_{2p} - K_p\hat{x}_{1p} - K_t\hat{x}_{1p} + Tu) + \hat{\sigma}_1 + \frac{\alpha_2}{\epsilon_h^{2\rho}}(y_p - \hat{x}_{1p}),\\
\dot{\hat{\sigma}}_1 &= M_p^{-1}K_t\hat{x}_{2t} + \frac{\alpha_3}{\epsilon_h^{3\rho}}(y_p - \hat{x}_{1p}),\\
\dot{\hat{x}}_{1t} &= \hat{x}_{2t} + \frac{\beta_1}{\epsilon_h}(\hat{\sigma}_1 - M_p^{-1}K_t\hat{x}_{1t}),\\
\dot{\hat{x}}_{2t} &= M_t^{-1}(-D_t\hat{x}_{2t} - K_t\hat{x}_{1t} + K_t\hat{x}_{1p}) + \hat{\sigma}_2 + \frac{\beta_2}{\epsilon_h^{2}}(\hat{\sigma}_1 - M_p^{-1}K_t\hat{x}_{1t}),\\
\dot{\hat{\sigma}}_2 &= \frac{\beta_3}{\epsilon_h^{3}}(\hat{\sigma}_1 - M_p^{-1}K_t\hat{x}_{1t}),
\end{aligned}
\tag{5.12}
$$

where ϵ_h is designed to be $0 < \epsilon_h < 1$ and for α_1 to α_3 and β_1 to β_3 to be chosen such that polynomials

$$s^3 + \beta_1 s^2 + \beta_2 s + \beta_3, \qquad s^3 + \alpha_1 s^2 + \alpha_2 s + \alpha_3,$$

are to be Hurwitz. ρ is to be chosen such that $\rho > 1$ to allow for the piezotube dynamics with state feedback to evolve faster than the under-actuated tip dynamics to ensure that a reasonable value of σ_1 is provided for the proceeding observer. This formulation consists of the cascade observer design explained in (5.5) but with an EHGO as the second observer. This design can be seen below in the block diagram of Fig. 5.12 where d represents the desired trajectory.

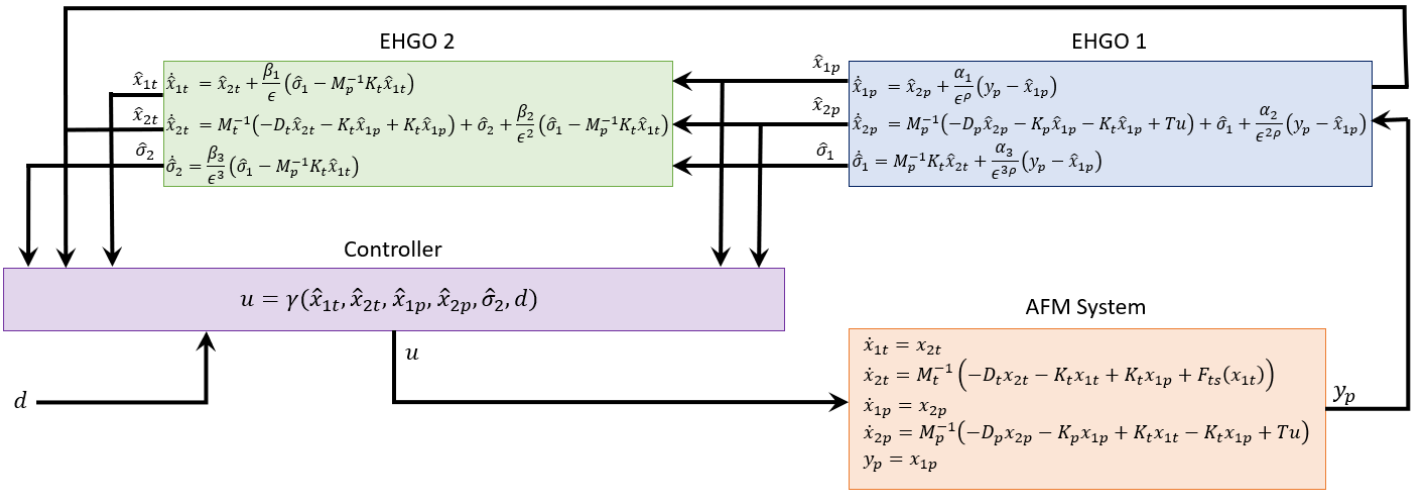

Figure 5.12: Closed-loop output feedback control system using cascade observer

The observer is designed such that the piezotube estimates evolve at a significantly faster rate than the tip estimates. This differs from the previously designed observer. In the combined observer, the tip and piezotube worked together to bring their state estimates to the actual states, but now the piezotube estimates works to bring the tip estimates to their actual states in the cascade observer. To achieve this, the piezotube estimate of $\hat{\sigma}_1$ should be brought immediately to $M_p^{-1}K_t\hat{x}_{1t}$ to prevent the high gain produced by a vastly different $\hat{\sigma}_1$ and $M_p^{-1}K_t\hat{x}_{1t}$ from bringing the tip dynamics to incorrect, potentially unstable, estimates. Following this statement however, our α and β design parameters are to be selected such that the eigenvalues from their respective polynomials for each α_i and β_i to match. This is necessary for the point at which both system converge to to be derivatives of each other. The magnitude of the high-gain at which these estimates converge about is different because of ρ. ρ is chosen such that ϵ_h^ρ allows for the piezotube estimates of the first observer to evolve faster than the tip estimates of the second observer. Our chosen design values can be seen in Table 5.2.

Table 5.2: Cascaded high-gain observer design parameters

Symbol	Numerical Value
ϵ_h	1×10^{-7}
ρ	1.2
α_1	6
α_2	11
α_3	6
β_1	6
β_2	11
β_3	6

Similar to the combined high-gain observer of the previous section, our estimated error and vibrational forces continue to follow the formulations of (5.9). With our cascaded observer and these expressions defined, we will create an output feedback controller.

5.3.2 Output Feedback Control of Cascaded Observer

Following the cascaded output feedback design outline of [57], we will begin our control design by replacing the states of our state feedback near-optimal controller of Chapter 4. With our state estimates of (5.12) and (5.9) defined, our output feedback controller of (4.18) becomes

$$\begin{aligned}\hat{u}_c = \gamma(\hat{e}, \hat{z}) = sat(&-R_0^{-1}(\hat{s}_0 + \frac{1}{2}B_0^T P_s^T \hat{e}) \\ &-R^{-1}B_2^T P_f(\hat{z} + A_2^{-1}\hat{a}_2 - A_2^{-1}B_2 R_0^{-1}(\hat{s}_0 + \frac{1}{2}B_0^T P_s^T \hat{e})))\end{aligned} \tag{5.13}$$

where

$$\hat{a}_2 = \begin{bmatrix} 0 \\ -\sigma_{e_1}\hat{e}_1 + \sigma_{e_2}\hat{e}_2 - \sigma_{F_{ts}}\sigma_2 \end{bmatrix}$$
$$\hat{s}_0(e_s) = B_2^T A_{2s}^{-T} Q_z A_{2s}^{-1} \hat{a}_2,$$

This expression is the same of that formulated for (4.18), but uses the estimates from our cascaded observer as the provided states. The cascaded observer is designed to recover state feedback stability properties. Similarly to that of the combined observer of the previous section, we are able to represent the estimated disturbance σ_2 in our controller and use its information to aid in the control effort. Saturation is also applied to our controller to reduce high-gain peaking.

The performance of the closed-loop system can be analyzed by constructing the scaled estimation error expressions

$$\begin{aligned}
\eta_1 &= (x_{1t} - \hat{x}_{1t}) \\
\eta_2 &= \epsilon_h(x_{2t} - \hat{x}_{2t}) \\
\eta_3 &= \epsilon_h^2(M_t^{-1}F_{ts}(x_{1t}) - \hat{\sigma}_2) \\
\chi_1 &= x_{1p} - \hat{x}_{1p} \\
\chi_2 &= \epsilon_h^{\rho}(x_{2p} - \hat{x}_{2p}) \\
\chi_3 &= \epsilon_h^{2\rho}(M_p^{-1}K_t x_{1t} - \hat{\sigma}_1)
\end{aligned} \tag{5.14}$$

Let

$$\phi = \begin{bmatrix} \chi_1 \\ \chi_2 \end{bmatrix}, \quad \chi = \begin{bmatrix} \phi \\ \chi_3 \end{bmatrix}, \quad \vartheta = \begin{bmatrix} \eta_1 \\ \eta_2 \end{bmatrix}, \quad \eta = \begin{bmatrix} \vartheta \\ \eta_3 \end{bmatrix},$$

$$R(\epsilon_h) = \text{blockdiag}[R_1, R_2, R_3], R_k(\epsilon_h) = \text{diag}[1, \frac{1}{\epsilon_h}],$$

$$N(\epsilon_h) = \text{blockdiag}[N_1, N_2, N_3], N_k(\epsilon_h) = \text{diag}[1, \frac{1}{\epsilon_h}, \frac{1}{\epsilon_h^2}],$$

$$Q(\epsilon_h) = \text{blockdiag}[Q_1, Q_2, Q_3], Q_k(\epsilon_h) = \text{diag}[\epsilon_h^{2\rho-1}, \epsilon_h^{\rho-1}],$$

$$S(\epsilon_h) = \text{blockdiag}[S_1, S_2, S_3], S_k(\epsilon_h) = \text{diag}[\epsilon_h^{2\rho-1}, \epsilon_h^{\rho-1}, \epsilon_h],$$

$k = 1, 2, 3$. Then (5.14) can be written in the compact form

$$\begin{aligned}
R(\epsilon_h)\vartheta &= \begin{bmatrix} x_t - \hat{x}_t \end{bmatrix} \\
N(\epsilon_h)\eta &= \begin{bmatrix} x_t - \hat{x}_t \\ M_p^{-1}K_t x_{1t} - \hat{\sigma}_2 \end{bmatrix} \\
Q(\epsilon_h)\phi &= \begin{bmatrix} x_p - \hat{x}_p \end{bmatrix} \\
S(\epsilon_h)\chi &= \begin{bmatrix} x_p - \hat{x}_p \\ M_p^{-1}K_t x_{1t} - \hat{\sigma}_1 \end{bmatrix}
\end{aligned} \tag{5.15}$$

It is worth noting that the expressions in (5.15) can be rewritten in terms of vibrational force z as

$$\begin{aligned} \tilde{z} &= z - \hat{z}, \\ Z(\epsilon_h) &= K_t(Q(\epsilon_h)\phi - R(\epsilon_h)\vartheta). \end{aligned} \tag{5.16}$$

For the closed loop system, our error states now are of

$$e_c = \begin{bmatrix} x_t - x_t^* \\ x_p - x_p^* \end{bmatrix}, \qquad d = \begin{bmatrix} x_t^* \\ x_p^* \end{bmatrix} \tag{5.17}$$

where $x_t^* = x_p^*$ because we wish to maintain $z^* = 0$, as $z^* = K_t(x_p^* - x_t^*)$, and $x_{1tz}^* = x_{1pz}^* = 0$, as we wish to maintain the cantilever tip at the equilibrium point defined at zero. As a result, the closed-loop system under output feedback takes the form

$$\begin{aligned} \dot{e}_c &= f(e_c, \gamma(x_t - R\vartheta, x_p - Q\phi)) = f(e_c, \gamma(\hat{x}_t, \hat{x}_p)) = f(e_c, \gamma(x_t - R\vartheta - x_t^*, z - Z)) \\ &= \begin{bmatrix} 0 & I & 0 & 0 \\ -M_t^{-1}K_t & -D_tM_t^{-1} & M_t^{-1}K_t & 0 \\ 0 & 0 & 0 & I \\ M_p^{-1}K_t & 0 & M_p^{-1}(K_t - K_p) & -M_p^{-1}D_p \end{bmatrix} e_c + \begin{bmatrix} 0 \\ 0 \\ 0 \\ M_p^{-1}T \end{bmatrix} \gamma(\hat{x}_t, \hat{x}_p) + \begin{bmatrix} 0 \\ M_t^{-1}F_{ts}(x_{1t}) \\ 0 \\ 0 \end{bmatrix} \end{aligned} \tag{5.18}$$

$$\epsilon_h\dot{\eta} = \begin{bmatrix} -\beta_1 & 1 & 0 \\ -\beta_2 & 0 & 1 \\ -\beta_3 & 0 & 0 \end{bmatrix} \eta + \epsilon_h \begin{bmatrix} 0 \\ -\epsilon_h M_t^{-1}K_t\eta_1 - M_t^{-1}D_t\eta_2 + \epsilon_h^2 M_t^{-1}K_t\chi_1 \\ \epsilon_h^2 M_t^{-1}\dot{F}_{ts}(x_{1t}) \end{bmatrix} \tag{5.19}$$

$$\epsilon_h^\rho\dot{\chi} = \begin{bmatrix} -\alpha_1 & 1 & 0 \\ -\alpha_2 & 0 & 1 \\ -\alpha_3 & 0 & 0 \end{bmatrix} \chi + \epsilon_h \begin{bmatrix} 0 \\ -\epsilon_h^{2\rho} M_p^{-1}(K_p + K_t)\chi_1 - \epsilon_h^\rho M_p^{-1}D_p\chi_2 \\ \epsilon_h^{3\rho-1} M_p^{-1}K_t\eta_2 \end{bmatrix} \tag{5.20}$$

It can be seen that (5.19) and (5.20) follow a singular perturbation form where ϵ_h is on the left hand side of the expression implying that these equations evolve at a faster rate than (5.18). By setting $\epsilon_h = 0$ in (5.19) and (5.20), $\eta = 0$ and $\chi = 0$ and we get the reduced system

$$\dot{e}_c = f_r(e_c, \gamma(x_t, x_p)) = f_r(e_c, \gamma(x_t, z)), \tag{5.21}$$

which represents normal state feedback of our closed-loop system. This implies that our cascaded output feedback controller performs near-optimally similarly to that of state feedback (4.18). This is further verified by the Hurwitz design of α and β appearing in the canonical form for η and χ in (5.19) and (5.20). Because of this, we can argue that the near-optimal design achieves the stabilization objective resulting in output feedback being ultimately bounded.

5.3.3 Cascaded Observer Simulations

Like the combined observer section, our simulations were conducted using the output feedback controller described by (5.13) of which the cascaded observer (5.12) produces state estimates from the outputs of the system (5.7) using $\hat{u}_c$ instead of u. The initial conditions of the system match those previously defined by Table 3.2. Our observer's state estimate initial conditions were all set to 0 for our simulations.

It can be seen in the figures that the cascaded output feedback controller was able control our system similarly to state feedback produced by Chapter 4. It is also worth noting how σ_1 was successfully able to track x_{1x} in Fig. 5.23 and σ_2 was able to estimate the nonlinear disturbance in Fig. 5.24.

The simulations produced by the cascaded observer demonstrate promising contributions to cascaded observer applications. Our AFM dynamics were able to follow desired trajectories using output feedback from measuring only the piezotube position and apply these estimates to a near-optimal nonlinear controller. Despite not measuring the AFM cantilever tip position to monitor its changes cased by the nonlinearities, our cascaded observer was able to estimate these changes through the changes of the piezotube. This is possible because of analyzed performance resulting from the high-gain bringing our state estimates to their respective actual state values to replicate state feedback relatively fast.

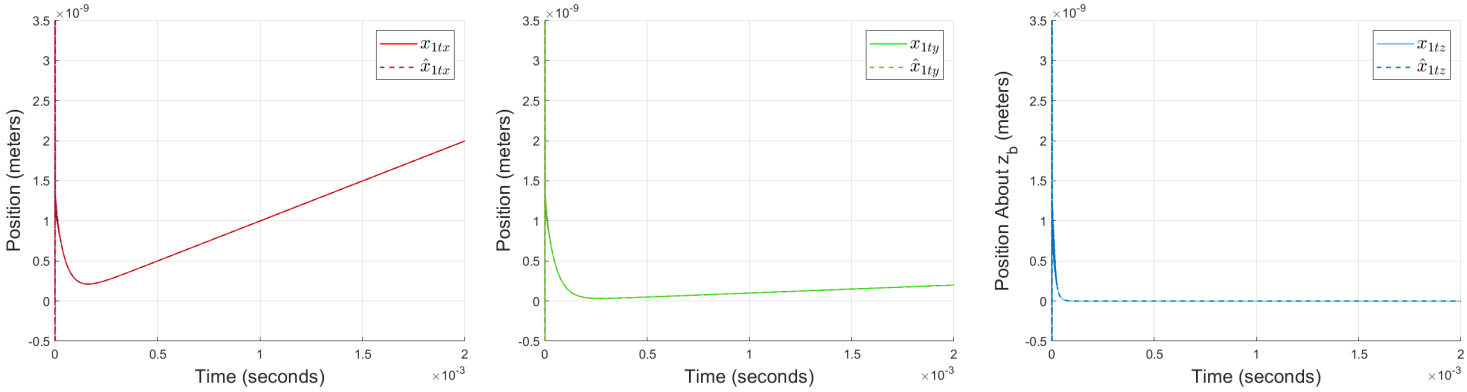

(a) X-axis tip position (b) Y-axis tip position (c) Z-axis tip position

Figure 5.13: Cascaded observer output feedback control x_{1t} performance

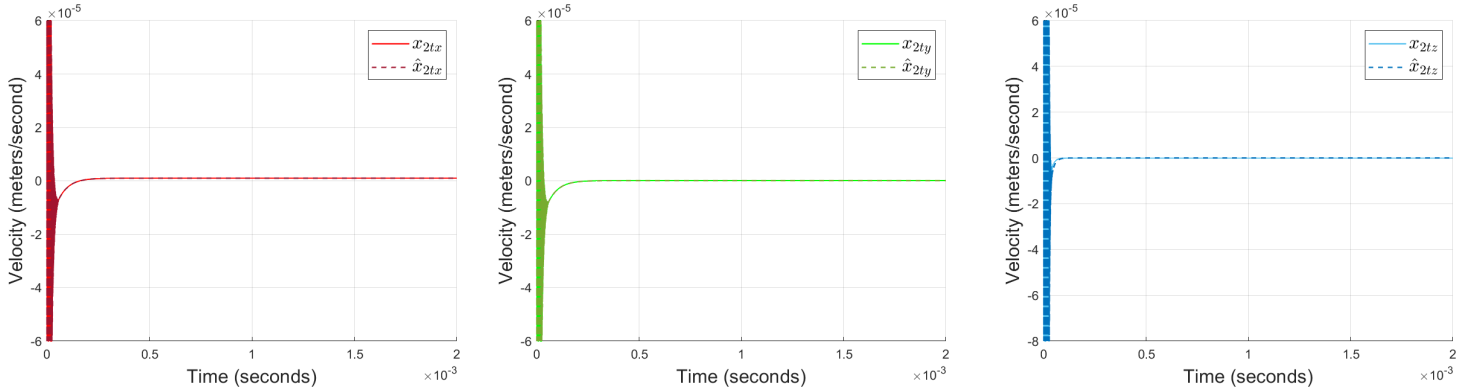

(a) X-axis tip velocity (b) Y-axis tip velocity (c) Z-axis tip velocity

Figure 5.14: Cascaded observer output feedback control x_{2t} performance

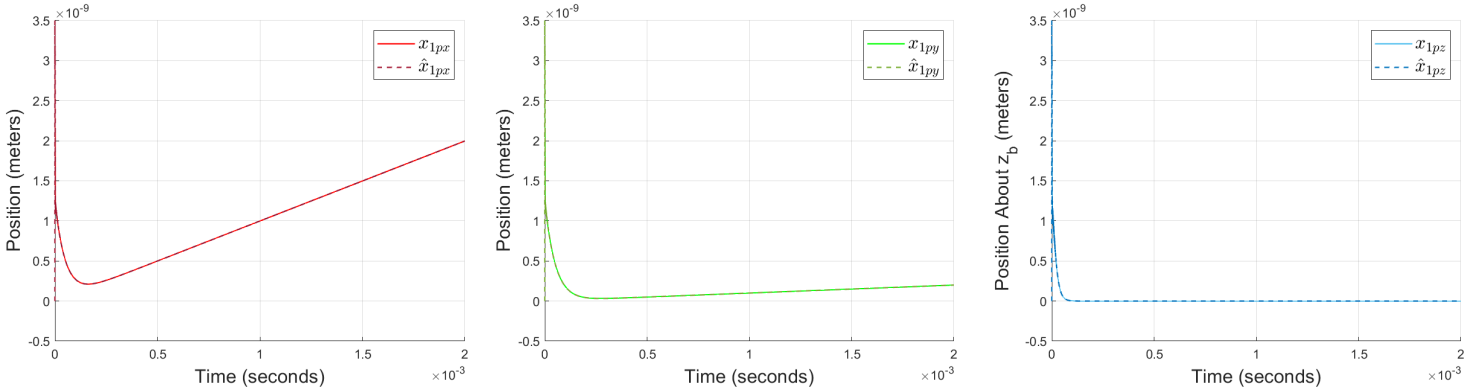

(a) X-axis piezotube position (b) Y-axis piezotube position (c) Z-axis piezotube position

Figure 5.15: Cascaded observer output feedback control x_{1p} performance

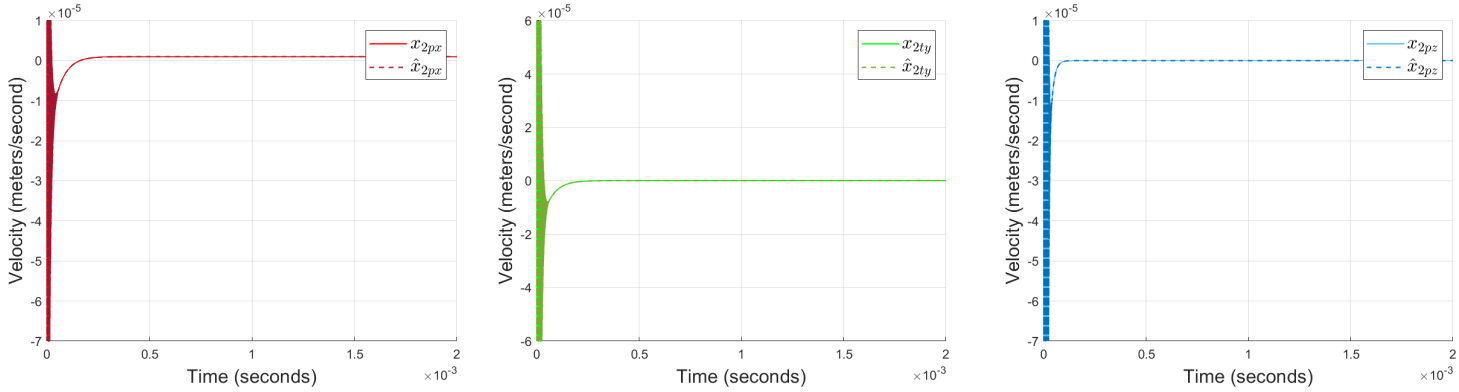

(a) X-axis piezotube velocity (b) Y-axis piezotube velocity (c) Z-axis piezotube velocity

Figure 5.16: Cascaded observer output feedback control x_{2p} performance

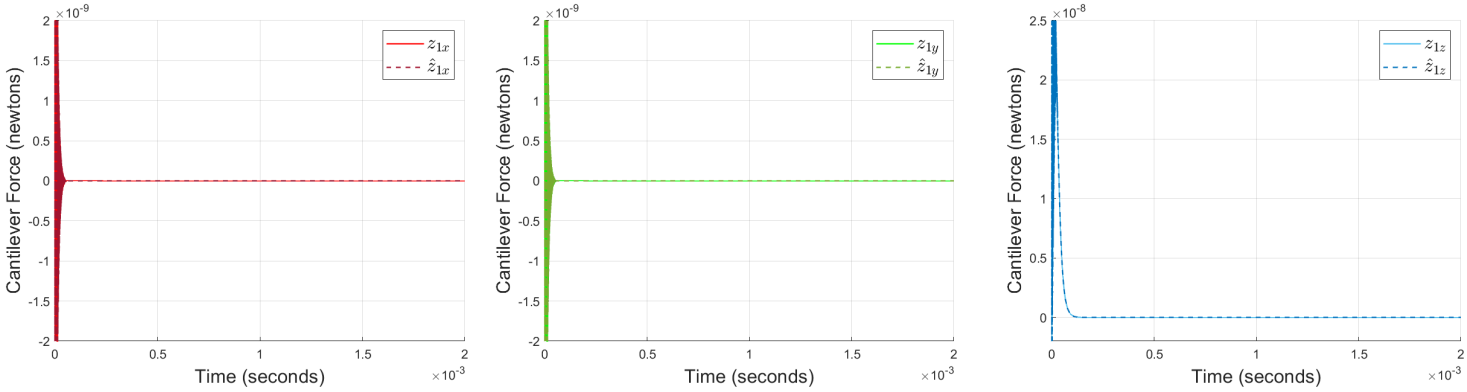

(a) X-axis vibrational force (b) Y-axis vibrational force (c) Z-axis vibrational force

Figure 5.17: Cascaded observer output feedback control z_1 performance

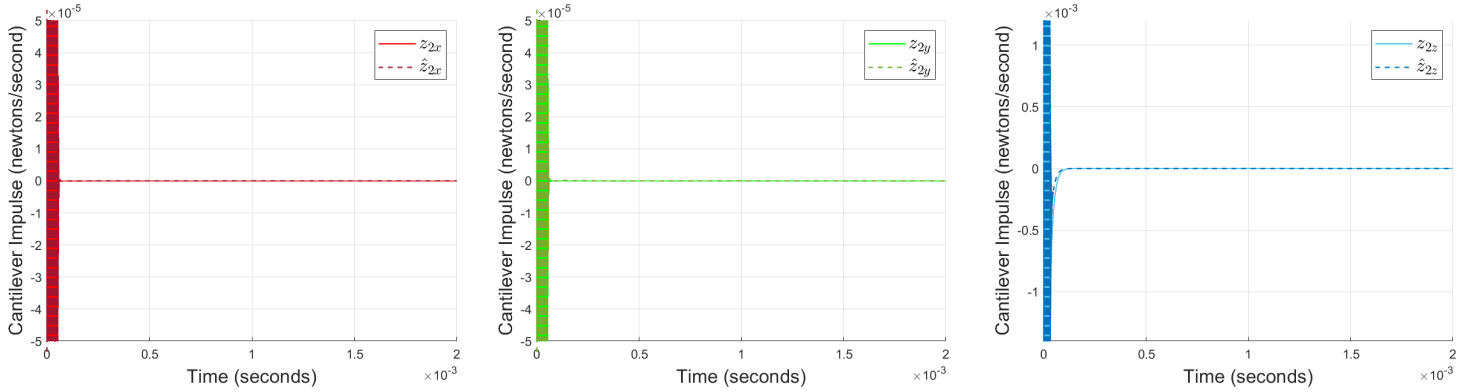

(a) X-axis vibrational impulse (b) Y-axis vibrational impulse (c) Z-axis vibrational impulse

Figure 5.18: Cascaded observer output feedback control z_2 performance

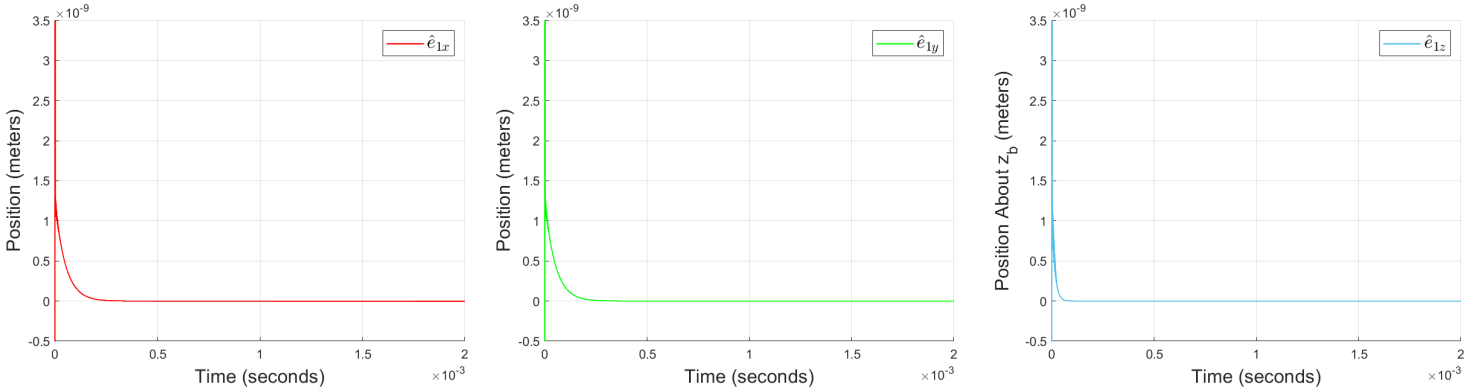

(a) X-axis tip position error (b) Y-axis tip position error (c) Z-axis tip position error

Figure 5.19: Cascaded observer output feedback control e_1 performance

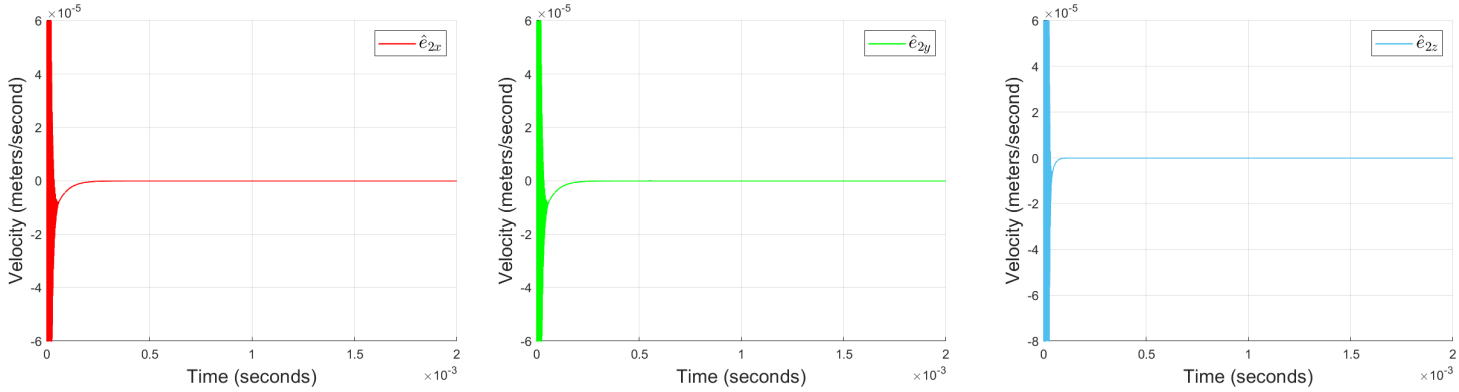

(a) X-axis tip velocity error (b) Y-axis tip velocity error (c) Z-axis tip velocity error

Figure 5.20: Cascaded observer output feedback control e_2 performance

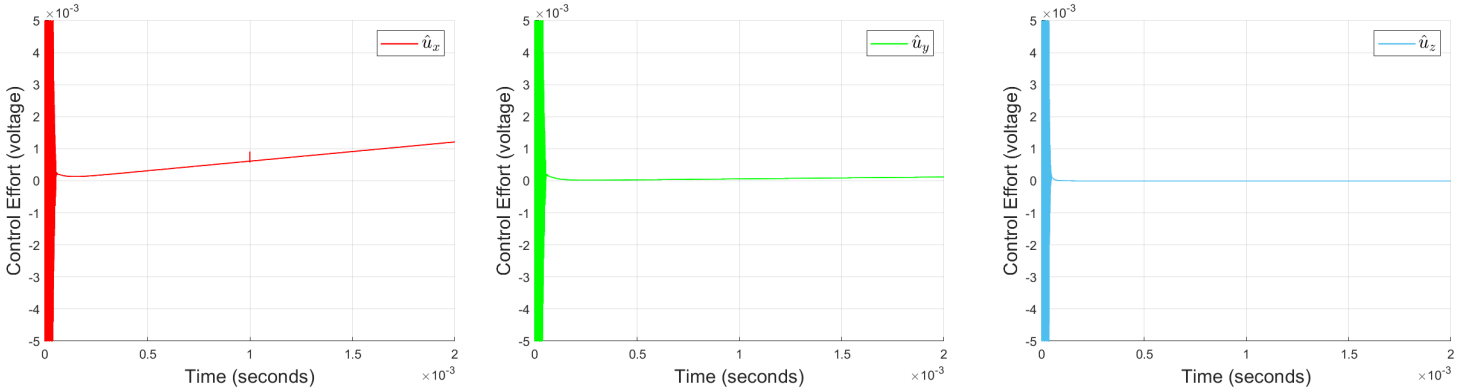

(a) X-axis control effort (b) Y-axis control effort (c) Z-axis control effort

Figure 5.21: Cascaded observer output feedback control u control effort

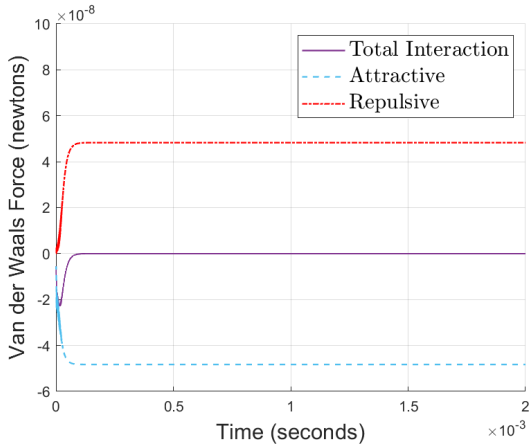

Figure 5.22: Interaction forces affecting the nonlinear near-optimal controller

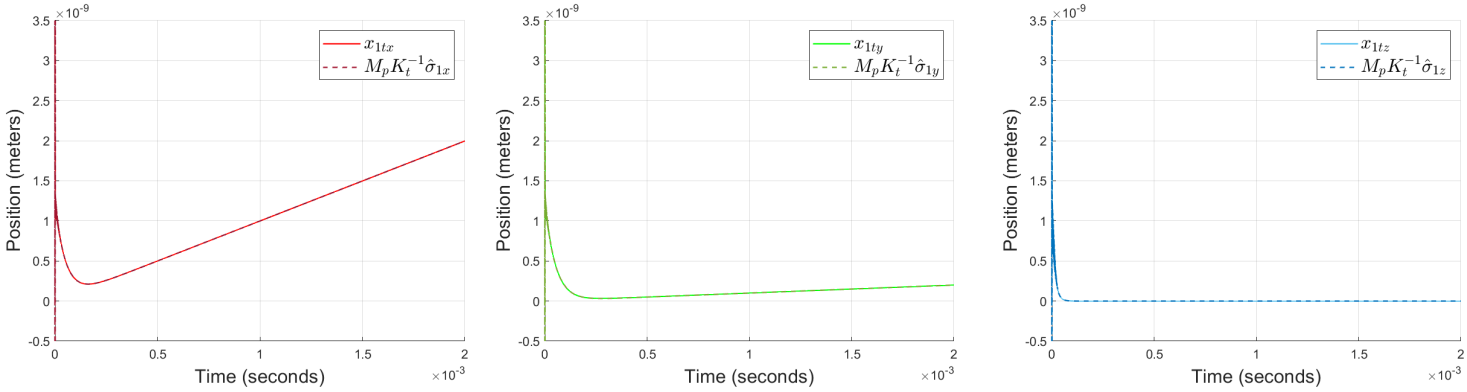

(a) X-axis estimate (b) Y-axis estimate (c) Z-axis estimate

Figure 5.23: Cascaded observer output feedback control σ_1 estimated x_{1t} position

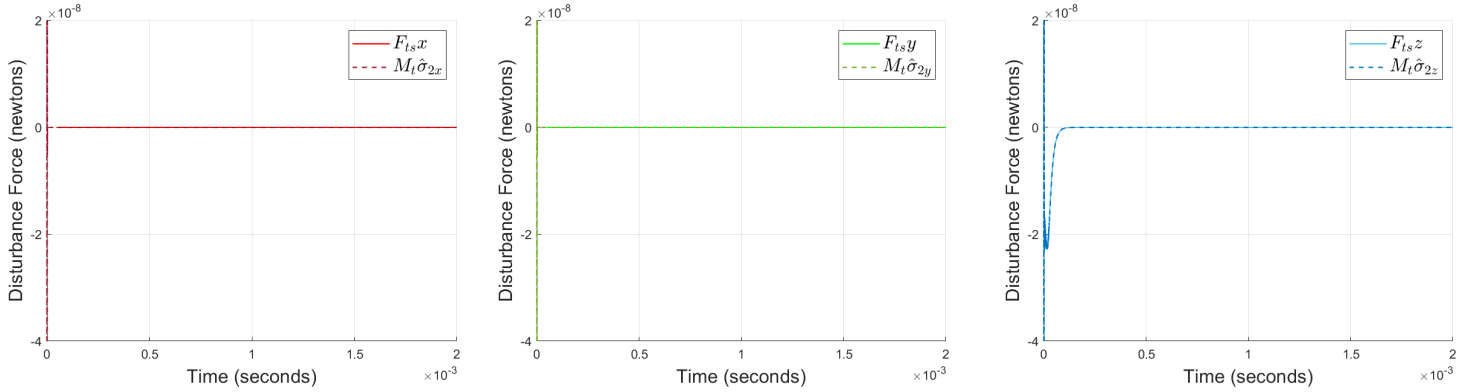

(a) X-axis disturbance (b) Y-axis disturbance (c) Z-axis disturbance

Figure 5.24: Cascaded observer output feedback control σ_2 estimated disturbance

Chapter 6

Conclusion

Our work presented here provides furthering contributions to the work of AFM non-contact mode control. By using the stiffness property of the AFM cantilever, we were able to simplify the control design and improve the system performance. Stiff cantilevers are common for non-contact mode applications, and applying this fact allowed for singular perturbation principles to simplify the control problem regarding nonlinear interaction forces. A nonlinear near-optimal controller was designed based on these singular perturbation principles to allow for global control over the AFM dynamics and Van der Waals forces. Our results demonstrate fast convergence within a few milliseconds to desired trajectories which can improve scanning speed. Cascaded observers were constructed to produce system state estimates using only the measurement of the piezotube position. Because of the cascaded observer's high gain, we were able to apply the estimates for output feedback into our nonlinear near-optimal controller to replicate the responses of full state feedback. We were able to produce estimates of unknown surface interaction forces and use this information to improve our control efforts. The design choice to use only the feedback of the piezotube position in the observer works to reduce the overall complexity of design of the AFM machine by eliminating the laser diode feedback measurement system used to track the AFM tip performance. As a topic of current research, we are continuing our work demonstrating stability for the output feedback control.

Bibliography

[1] T. Ando, "High-speed atomic force microscopy coming of age," *Nanotechnology*, vol. 23, no. 6, p. 062001, 2012.

[2] J. C. Fernandes, V. Mareau, and L. Gonon, "Afm-raman colocalization setup: Advanced characterization technique for polymers," *International Journal of Polymer Analysis and Characterization*, vol. 23, no. 2, pp. 113–119, 2018.

[3] R. A. Oliver, "Advances in afm for the electrical characterization of semiconductors," *Reports on Progress in Physics*, vol. 71, no. 7, p. 076501, 2008.

[4] B. Rogers, L. Manning, T. Sulchek, and J. Adams, "Improving tapping mode atomic force microscopy with piezoelectric cantilevers," *Ultramicroscopy*, vol. 100, no. 3-4, pp. 267–276, 2004.

[5] M. S. Rana, H. R. Pota, and I. R. Petersen, "A survey of methods used to control piezoelectric tube scanners in high-speed afm imaging," *Asian Journal of Control*, vol. 20, no. 4, pp. 1379–1399, 2018.

[6] M. Rana, H. Pota, and I. Petersen, "Performance of sinusoidal scanning with mpc in afm imaging," *IEEE/ASME Transactions on Mechatronics*, vol. 20, no. 1, pp. 73–83, 2014.

[7] M. Rana, H. R. Pota, and I. R. Petersen, "Improvement in the imaging performance of atomic force microscopy: A survey," *IEEE Transactions on Automation Science and Engineering*, vol. 14, no. 2, pp. 1265–1285, 2016.

[8] S. Thalhammer and W. M. Heckl, "Atomic force microscopy as a tool in nanobiology part i: Imaging and manipulation in cytogenetics," *Cancer Genomics & Proteomics*, vol. 1, no. 1, pp. 59–70, 2004.

[9] S. Hornstein and O. Gottlieb, "Nonlinear dynamics, stability and control of the scan process in noncontacting atomic force microscopy," *Nonlinear Dynamics*, vol. 54, no. 1, pp. 93–122, 2008.

[10] L. Chopinet, C. Formosa, M. Rols, R. Duval, and E. Dague, "Imaging living cells surface and quantifying its properties at high resolution using afm in qi™ mode," *Micron*, vol. 48, pp. 26–33, 2013.

[11] Y. Seo and W. Jhe, "Atomic force microscopy and spectroscopy," *Reports on Progress in Physics*, vol. 71, no. 1, p. 016101, 2007.

[12] J. Keighobadi, J. Faraji, and S. Rafatnia, "Chaos control of atomic force microscope system using nonlinear model predictive control," *Journal of Mechanics*, vol. 33, no. 3, pp. 405–415, 2017.

[13] R. Nozaki, J. M. Balthazar, A. M. Tusset, B. R. de Pontes, and Á. M. Bueno, "Nonlinear control system applied to atomic force microscope including parametric errors," *Journal of Control, Automation and Electrical Systems*, vol. 24, no. 3, pp. 223–231, 2013.

[14] I. Kirrou and M. Belhaq, "Control of bistability in non-contact mode atomic force microscopy using modulated time delay," *Nonlinear Dynamics*, vol. 81, no. 1, pp. 607–619, 2015.

[15] S. Rützel, S. I. Lee, and A. Raman, "Nonlinear dynamics of atomic–force–microscope probes driven in lennard–jones potentials," *Proceedings of the Royal Society of London.*

Series A: Mathematical, Physical and Engineering Sciences, vol. 459, no. 2036, pp. 1925–1948, 2003.

[16] M. Cetin and S. Beyhan, "Active fault tolerant control for high-precision positioning of a non-contact mode uncertain atomic force microscopy," *Transactions of the Institute of Measurement and Control*, vol. 42, no. 14, pp. 2632–2644, 2020.

[17] Y. S. Hamed, K. Albogamy, and M. Sayed, "A proportional derivative (pd) controller for suppression the vibrations of a contact-mode afm model," *IEEE Access*, vol. 8, pp. 214 061–214 070, 2020.

[18] A. M. Tusset, J. M. Balthazar, J. Jose de Lima, R. T. Rocha, F. C. Janzen, and P. S. Yamaguchi, "On an optimal control applied in atomic force microscopy (afm) including fractional-order," in *International Design Engineering Technical Conferences and Computers and Information in Engineering Conference*, vol. 58165. American Society of Mechanical Engineers, 2017, p. V004T09A003.

[19] K. Merat, J. A. Chekan, H. Salarieh, and A. Alasty, "Linear optimal control of continuous time chaotic systems," *ISA transactions*, vol. 53, no. 4, pp. 1209–1215, 2014.

[20] K. El Rifai, O. El Rifai, and K. Youcef-Toumi, "Modeling and control of afm-based nanomanipulation systems," in *Proceedings of the 2005 IEEE International Conference on Robotics and Automation.* IEEE, 2005, pp. 157–162.

[21] S. Maghsoudy-Louyeh, M. Kropf, and B. Tittmann, "Review of progress in atomic force microscopy," *The Open Neuroimaging Journal*, vol. 12, no. 1, 2018.

[22] J. Cailliez, M. Boudaoud, S. Liang, and S. Régnier, "Robust hybrid control of an atomic force microscope for the characterization of interaction force regions at the nanoscale," *IEEE Transactions on Control Systems Technology*, vol. 29, no. 4, pp. 1689–1703, 2020.

[23] Y. Seo, H. Choe, and W. Jhe, "Atomic-resolution noncontact atomic force microscopy in air," *Applied physics letters*, vol. 83, no. 9, pp. 1860–1862, 2003.

[24] F. J. Giessibl, H. Bielefeldt, S. Hembacher, and J. Mannhart, "Calculation of the optimal imaging parameters for frequency modulation atomic force microscopy," *Applied Surface Science*, vol. 140, no. 3-4, pp. 352–357, 1999.

[25] E. Guliyev, B. Volland, Y. Sarov, T. Ivanov, M. Klukowski, E. Manske, and I. Rangelow, "Quasi-monolithic integration of silicon-mems with piezoelectric actuators for high-speed non-contact atomic force microscopy," *Measurement Science and Technology*, vol. 23, no. 7, p. 074012, 2012.

[26] S. Hu and A. Raman, "Chaos in atomic force microscopy," *Physical Review Letters*, vol. 96, no. 3, p. 036107, 2006.

[27] J. Lessard, P. Bigras, Z. Liu, and B. Hazel, "Characterization, modeling and vibration control of a flexible joint for a robotic system," *Journal of Vibration and Control*, vol. 20, no. 6, pp. 943–960, 2014.

[28] W. Kim, D. Shin, Y. Lee, and C. C. Chung, "Nonlinear control based on singular perturbation theory for position tracking of permanent magnet stepper motors," in *2012 American Control Conference (ACC)*. IEEE, 2012, pp. 1186–1191.

[29] F. Landolsi and F. Ghorbel, "Design and singular perturbation control of a piezotube-based nanomanipulator," *Nonlinear Dynamics*, vol. 83, no. 1, pp. 971–981, 2016.

[30] S. Messineo, M. R. Ragazzon, F. Busnelli, and J. T. Gravdahl, "Analysis of pi-control for atomic force microscopy in contact mode," *IEEE Transactions on Control Systems Technology*, 2021.

[31] J. Chow and P. Kokotovic, "A two-stage lyapunov-bellman feedback design of a class of nonlinear systems," *IEEE Transactions on Automatic Control*, vol. 26, no. 3, pp. 656–663, 1981.

[32] A. Saberi and H. Khalil, "Stabilization and regulation of nonlinear singularly perturbed systems–composite control," *IEEE Transactions on Automatic Control*, vol. 30, no. 8, pp. 739–747, 1985.

[33] P. Kokotović, H. K. Khalil, and J. O'reilly, *Singular perturbation methods in control: analysis and design*. SIAM, 1999.

[34] Y. Yan, Y. Wu, Q. Zou, and C. Su, "An integrated approach to piezoactuator positioning in high-speed atomic force microscope imaging," *Review of Scientific Instruments*, vol. 79, no. 7, p. 073704, 2008.

[35] K. J. Åström and R. M. Murray, "Feedback systems," in *Feedback Systems*. Princeton university press, 2010.

[36] S. R. Moheimani and Y. K. Yong, "Simultaneous sensing and actuation with a piezoelectric tube scanner," *Review of Scientific Instruments*, vol. 79, no. 7, p. 073702, 2008.

[37] B. Bhikkaji, M. Ratnam, A. J. Fleming, and S. R. Moheimani, "High-performance control of piezoelectric tube scanners," *IEEE Transactions on Control Systems Technology*, vol. 15, no. 5, pp. 853–866, 2007.

[38] W. Wei and G. Lei, "Chaos control in afm via disturbance observer based control," in *2016 35th Chinese Control Conference (CCC)*. IEEE, 2016, pp. 869–872.

[39] W.-H. Chen, D. J. Ballance, P. J. Gawthrop, and J. O'Reilly, "A nonlinear disturbance observer for robotic manipulators," *IEEE Transactions on industrial Electronics*, vol. 47, no. 4, pp. 932–938, 2000.

[40] A. F. Payam, M. Fathipour, and M. J. Yazdanpanah, "High precision imaging for non-contact mode atomic force microscope using an adaptive nonlinear observer and output state feedback controller." *Digest Journal of Nanomaterials & Biostructures (DJNB)*, vol. 4, no. 3, 2009.

[41] R. Vatankhah, F. Karami, and H. Salarieh, "Observer-based vibration control of non-classical microcantilevers using extended kalman filters," *Applied Mathematical Modelling*, vol. 39, no. 19, pp. 5986–5996, 2015.

[42] A. N. Atassi and H. K. Khalil, "A separation principle for the control of a class of nonlinear systems," in *Proceedings of the 37th IEEE Conference on Decision and Control (Cat. No. 98CH36171)*, vol. 1. IEEE, 1998, pp. 855–860.

[43] H. K. Khalil, "Cascade high-gain observers in output feedback control," *Automatica*, vol. 80, pp. 110–118, 2017.

[44] S.-T. Ge, G.-Y. Tang, and C.-M. Zhang, "Optimal disturbance rejection for discrete-time nonlinear systems with time-delays via high-gain observer-based control," in *2010 Chinese Control and Decision Conference*. IEEE, 2010, pp. 870–874.

[45] M. N. Hasan and A. Y. Memon, "Output feedback nonlinear model predictive control for a class of nonlinear systems," in *2017 11th Asian Control Conference (ASCC)*. IEEE, 2017, pp. 2262–2267.

[46] A. M. Boker and H. K. Khalil, "Control of flexible joint manipulators using only motor position feedback: A separation principle approach," in *52nd IEEE Conference on Decision and Control*. IEEE, 2013, pp. 244–249.

[47] ——, "Full-order extended high gain observers for a class of nonlinear systems," in *2012 IEEE 51st IEEE Conference on Decision and Control (CDC)*. IEEE, 2012, pp. 5912–5917.

[48] N. Khalid and A. Y. Memon, "Output feedback control of a class of under-actuated nonlinear systems using extended high gain observer," *Arabian Journal for Science and Engineering*, vol. 41, no. 9, pp. 3531–3542, 2016.

[49] A. Boker and C. Yuan, "High-gain observer-based distributed tracking control of heterogeneous nonlinear multi-agent systems," in *2018 37th Chinese Control Conference (CCC)*. IEEE, 2018, pp. 6639–6644.

[50] M. Goldfarb and N. Celanovic, "Modeling piezoelectric stack actuators for control of micromanipulation," *IEEE Control Systems Magazine*, vol. 17, no. 3, pp. 69–79, 1997.

[51] M. Athans and P. L. Falb, *Optimal control: an introduction to the theory and its applications*. Courier Corporation, 2013.

[52] H. Kwakernaak and R. Sivan, "Linear optimal control systems wiley," *New York*, 1972.

[53] B. D. Anderson and J. B. Moore, *Linear Optimal Control [by] Brian DO Anderson [and] John B. Moore*. Prentice-hall, 1971.

[54] H. K. Khalil, "Nonlinear systems third edition," *Patience Hall*, vol. 115, 2002.

[55] ——, "Extended high-gain observers as disturbance estimators," *SICE Journal of Control, Measurement, and System Integration*, vol. 10, no. 3, pp. 125–134, 2017.

[56] S. G. Fronczak, C. A. Browne, E. C. Krenek, S. P. Beaudoin, and D. S. Corti, "Non-contact afm measurement of the hamaker constants of solids: Calibrating cantilever geometries," *Journal of colloid and interface science*, vol. 517, pp. 213–220, 2018.

[57] A. M. Boker, *Estimation and control of nonlinear systems using extended high-gain observers*. Michigan State University, 2013.

Appendices

Appendix A

Theorem 4.2.1 Verification

A.1 A Note About Our Assumption Conditions

For the below assumptions, we will be listing the following parameters

$$\begin{aligned} p &= \frac{1}{4} e^T P_s B_0 R_0^{-1} B_0^T P_s^T e, \\ s &= [0,0,0,0,0,0]^T, \\ Q_{z1} &= q_{z1} I, \quad Q_{z2} = q_{z2} I, \\ e_1 &= [e_{1x}, e_{1y}, e_{1z}]^T, \quad e_2 = [e_{2x}, e_{2y}, e_{2z}]^T. \end{aligned} \tag{A.1}$$

p was chosen as such to cancel out the $-\frac{1}{4}\frac{\partial V_s}{\partial e_s} B_0 R_0^{-1} B_0^T \frac{\partial V_s}{\partial e_s}^T$ expression seen at the end of the slow HJB expression of (4.6). This simplifies the overall HJB expression to reduce the number of $\frac{\partial V_s}{\partial e_s}$ there were to design around. s was chosen as such to also reduce the number of parameters in the HJB expression and that this is a common choice for s.

Along with matrix coordinates specifications, such as $P_{s(i,j)} \in \mathbb{R}^{3\times 3}$ represents the matrix coordinate segment (i,j) of P_s where

$$P_s = \begin{bmatrix} P_{s(1,1)} & P_{s(1,2)} \\ P_{s(2,1)} & P_{s(2,2)} \end{bmatrix} \in \mathbb{R}^{6\times 6} \tag{A.2}$$

For the slow HJB expression of [33] of which represents

$$0 = (p_0 - s_0^T R_0^{-1} s_0) + \frac{\partial V_s}{\partial e_s}(a_0 - B_0 R_0^{-1} s_0) - \frac{1}{4}\frac{\partial V_s}{\partial e_s} B_0 R_0^{-1} B_0^T (\frac{\partial V_s}{\partial e_s})^T, \tag{A.3}$$

it is defined that p and s are designed such that $\frac{\partial V_s}{\partial e_s}$ could be found such that the above expression is satisfied. In certain instances, this combination of parameters can be difficult to determine. However, Corollary 7.1 of [33] states that $\frac{\partial V_s}{\partial e_s}$ can be previously chosen such that, if the following assumptions are satisfied, it may be used for the implemented control objective. As such, we will go through the listed assumptions to prove that our controller design satisfies them.

A.2 Assumption 7.1

A.2.1 The scalar $p(e)+s(e)^T z+z^T Q_z z$ is a positive-definite function, except for when it equals zero when $e = 0$ and $z = 0$:

By letting $s = [0, 0, 0, 0, 0, 0]^T$ and $p = \frac{1}{4} e^T P_s B_0 R_0^{-1} B_0^T P_s^T e$, it can be recognized that R and Q_z were designed to be positive-definite matrices and thus the expression is positive-definite. It can also be recognized that setting $e = z = 0$, the expression also equals 0.

A.2.2 $a_0(0) = 0$:

By inspecting our a_0 expression,

$$a_0 = \begin{bmatrix} e_2 \\ -\dfrac{D_p e_2 - F_{ts}(e_1) + D_t e_2 + K_p e_1}{M_p + M_t} \end{bmatrix} \tag{A.4}$$

it can be seen that letting $e_1 = e_2 = 0$, where $F_{ts}(e_1)$ was designed to be zero when $e_1 = 0$, results in $a_0 = [0, 0]^T$.

A.2.3 $p_0(e) + 2s_0^T(e)u_s + u_s^T R_0 u_s > 0$ for all $e \neq 0$ and $u_s \neq 0$:

By inspecting the complete expression of this equation using our parameters results in

$$
\begin{aligned}
& p_0(e) + 2s_0^T(e)u_s + u_s^T R_0 u_s \\
& = \frac{1}{4} e^T P_s B_0 R_0^{-1} B_0^T P_s e \\
& +2(a_2^T(e) A_2^{-T} Q_z A_2^{-1} B_2)(-R_0^{-1}(s_0(e) + \tfrac{1}{2} B_0^T P_s e)) \\
& +(s_0(e)^T R_0^{-1} + \tfrac{1}{2} e^T P_s B_0 R_0^{-1}) R_0 (R_0^{-1} s_0(e) + \tfrac{1}{2} R_0^{-1} B_0^T P_s e) \\
& = 0.5(R{M_p}^2 + 2.0 R M_p M_t + Q_{z1} {M_t}^2 T^2 + R{M_t}^2)^{-1} \\
& \cdot(2.0 e_2^T Q_{z1} R {D_p}^2 {M_t}^2 e_2 - 4.0 e_2^T Q_{z1} R D_p D_t M_p M_t e_2 + 4.0 e_2^T Q_{z1} R D_p K_p {M_t}^2 e_1 \\
& +4.0 e_2^T Q_{z1} R D_p M_p M_t F_{ts}(e_1) + 2.0 e_2^T Q_{z1} R {D_t}^2 {M_p}^2 e_2 - 4.0 e_1^T Q_{z1} R D_t K_p M_p M_t e_2 \\
& -4.0 e_2^T Q_{z1} R D_t {M_p}^2 F_{ts}(e_1) + 2.0 e_1^T Q_{z1} R {K_p}^2 {M_t}^2 e_1 + 4.0 e_1^T Q_{z1} R K_p M_p M_t F_{ts}(e_1) \\
& +2.0 F_{ts}(e_1)^T Q_{z1} R {M_p}^2 F_{ts}(e_1) + e_1^T {P_{s(1,2)}}^2 T^2 e_1 + 2.0 e_1^T P_{s(1,2)} P_{s(2,2)} T^2 e_2 + e_2^T {P_{s(2,2)}}^2 T^2 e_2)
\end{aligned}
\tag{A.5}
$$

This expression does not clearly tell us if it is positive-definite for all e. By applying our simulation parameter values into this expression and providing a range of e values from -1 to 1, we get the following graph.

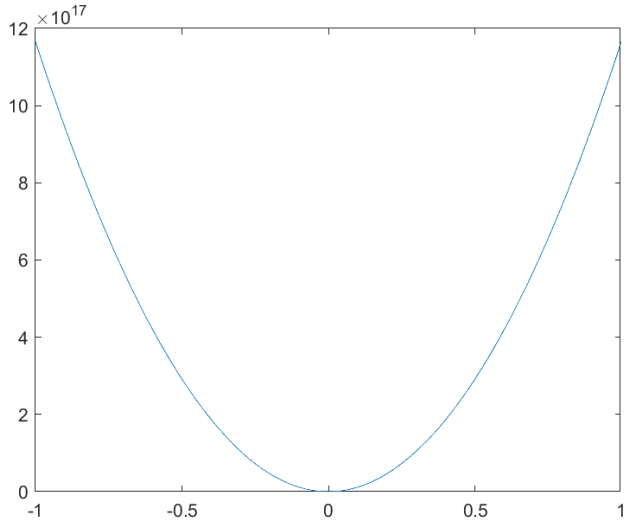

Figure A.1: Simulated plot demonstrating positive-definite condition $A.1.3$

It be be shown that the parabola shape of this expression is positive-definite. Thus, this condition is satisfied for our parameters.

A.3 Assumption 7.2

A.3.1 There exists a scalar positive-definite function $\psi(e)$ such that the following inequalities hold:

- $c_1\psi(e)^2 \leq p_0(e) - s_0^T(e)R_0^{-1}s_0(e) \leq c_2\psi(e)^2$

where $c_1 > 0$ and $c_2 > 0$:

$$
\begin{aligned}
&p_0(e) - s_0^T(e)R_0^{-1}s_0(e) \\
&= \frac{1}{4}e^T P_s B_0 R_0^{-1} B_0^T P_s^T e + a_2^T(e) A_2^{-T} Q_z A_2^{-1} a_2(e) \\
&- a_2^T(e) A_2^{-T} Q_z A_2^{-1} B_2 R_0^{-1} B_2^T A_2^{-T} Q_z A_2^{-1} a_2(e) \\
&= (R(M_p + M_t)^2 + M_t^2 Q_{z1} T^2)^{-1} T^2 (0.25 P_{s(1,2)} e_1 + 0.25 P_{s(2,2)} e_2)(P_{s(1,2)} e_1 + P_{s(2,2)} e_2) \\
&- (R(M_p + M_t)^4 + M_t^2 Q_{z1} T^2 (M_p + M_t)^2)^{-1} {M_t}^2 {Q_{z1}}^2 T^2 (M_p F_{ts}(e_1) + D_p M_t e_2 - D_t M_p e_2 + K_p M_t e_1)^2 \\
&+ ({K_t^*}^2 (M_p + M_t)^2)^{-1} {M_p}^2 {M_t}^2 Q_{z1} (M_t^{-1} K_t^* F_{ts}(e_1) + M_p^{-1} K_p K_t^* e_1 + M_p^{-1} K_t^* e_2 (D_p - M_t^{-1} D_t M_p))^2
\end{aligned}
\tag{A.6}
$$

It is unclear about the nature of the required expression. In terms of norm estimations,

$$
\frac{1}{4}||e||P_s B_0 R_0^{-1} B_0^T P_s^T||e|| + ||a_2(e)||(A_2^{-T} Q_z A_2^{-1} - A_2^{-T} Q_z A_2^{-1} B_2 R_0^{-1} B_2^T A_2^{-T} Q_z A_2^{-1})||a_2(e)||. \tag{A.7}
$$

By applying equivalent values of $||e||$ and $||a_2(e)||$ to our simulation parameters, we can observe the required boundedness by the following graph.

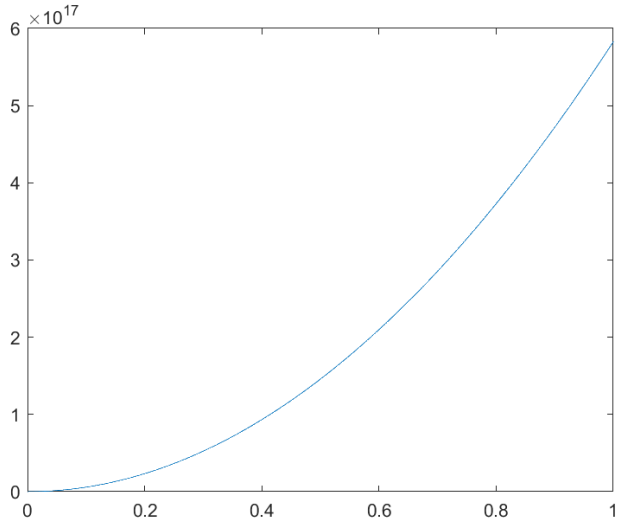

Figure A.2: Simulated plot demonstrating first condition $A.3.1$

- $||a_0(e) - B_0 R_0^{-1} s_0(e)|| \leq c_3 \psi(e)$

where $c_3 > 0$:

$$\begin{aligned} &||a_0(e) - B_0 R_0^{-1} s_0(e)|| \\ &= \sqrt{|e_2|^2 + \left| \begin{matrix} (M_p + M_t)^{-1} D_p e_2 - F_{ts}(e_1) + D_t e_2 + K_p e_1 \\ -(R(M_p + M_t)^3 + {M_t}^2 Q_{z1} T^2 (M_p + M_t))^{-1} \\ \cdot M_t Q_{z1} T^2 (M_p F_{ts}(e_1) + D_p M_t e_2 - D_t M_p e_2 + K_p M_t e_1)^2 \end{matrix} \right|^2} \end{aligned} \tag{A.8}$$

It is unclear about the nature of the required expression. In terms of norm estimations,

$$||||a_1(e)|| - A_1 A_2^{-1} ||a_2(e)|| - B_0 R_0^{-1} B_2^T A_2^{-T} Q_z A_2^{-1} ||a_2(e)||||. \tag{A.9}$$

By applying equivalent values of $||a_1(e)||$ and $||a_2(e)||$ to our simulation parameters, we can observe the required boundedness by the following graph.

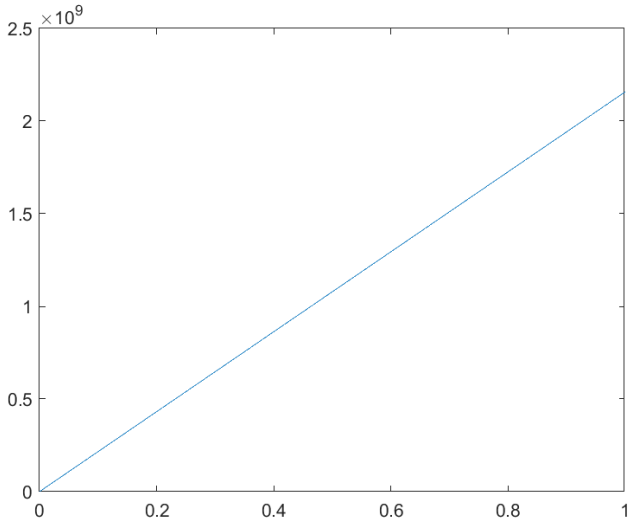

Figure A.3: Simulated plot demonstrating second condition $A.3.1$

- $||s(e) - 2Q_z A_2^{-1} a_2(e)|| \leq c_4 \psi(e)$

where $c_4 > 0$:

$$\begin{aligned} &||s(e) - 2Q_z A_2^{-1} a_2(e)|| \\ &= ||(M_p + M_t)^{-1} Q_{z1}(M_p F_{ts}(e_1) + D_p M_t e_2 - D_t M_p e_2 + K_p M_t e_1)|| \end{aligned} \tag{A.10}$$

It is unclear about the nature of the required expression. In terms of norm estimations,

$$|| - 2Q_z A_2^{-1} ||a_2(e)||||, \tag{A.11}$$

which results in the consideration of

$$c_4 = || - 2Q_z A_2^{-1}||. \tag{A.12}$$

By applying values of $||a_2(e)||$ to our simulation parameters, we can observe the required boundedness by the following graph.

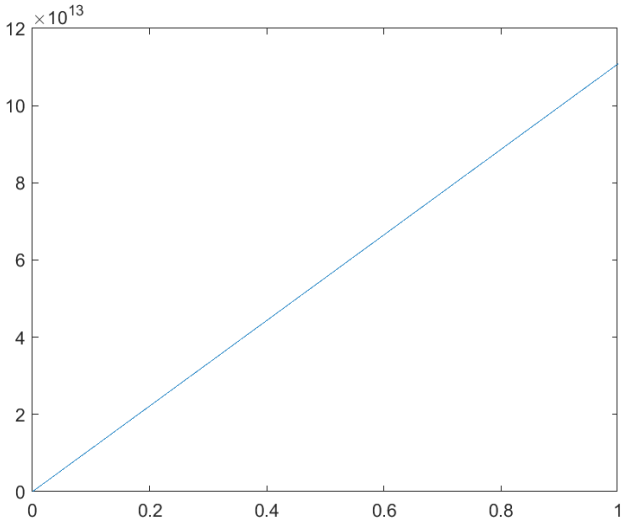

Figure A.4: Simulated plot demonstrating third condition $A.3.1$

A.3.2 $V_s(0) = 0$:

Our V_s expression of (3.14) is $V_s(e) = e^T P_s e$. Applying $e = 0$ results in $V_s(0) = (0)P_s(0) = 0$. Thus, this condition is satisfied.

A.4 Assumption 7.3

A.4.1 $||\frac{\partial V_s}{\partial e_s}|| \leq c\psi(e)$ where $c > 0$:

$$||\frac{\partial V_s}{\partial e_s}|| = ||e^T P_s|| \tag{A.13}$$

It is unclear about the nature of the required expression. In terms of norm estimations,

$$||||e||P_s||, \tag{A.14}$$

which results in the consideration of

$$c = ||P_s||. \tag{A.15}$$

By applying values of $||e||$ to our simulation parameters, we can observe the required boundedness by the following graph.

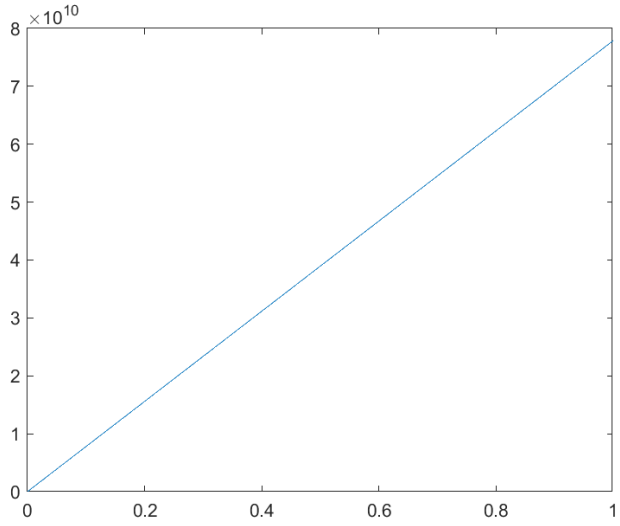

Figure A.5: Simulated plot demonstrating condition $A.4.1$

A.4.2 $-\alpha_0\psi^2(e) \leq \dfrac{\partial V_s}{\partial e_s}\bar{a}_0(e) \leq -\alpha_1\psi^2(e)$

where $\bar{a}_0(e) = a_0(e) + B_0u_s$**,** $\alpha_0 > 0$**, and** $\alpha_1 > 0$**:**

$$\begin{aligned}
&\frac{\partial V_s}{\partial e_s}\bar{a}_0(e) \\
&= e^T P_s(a_0(e) - B_0R_0^{-1}(s_0(e) + \tfrac{1}{2}B_0^T(\frac{\partial V_s}{\partial e_s})^T)) \\
&= e^T P_s a_0(e) - e^T P_s B_0 R_0^{-1} s_0(e) - \tfrac{1}{2}e^T P_s B_0 R_0^{-1} B_0^T P_s e \\
&= -(M_p + M_t)^{-1}(D_p e_2 - F_{ts}(e_1) + D_t e_2 + K_p e_1) \\
&-((M_p + M_t)R + (M_p + M_t)^{-1}M_t{}^2 Q_{z1} T^2)^{-1} \\
&\quad \cdot T(0.5(M_p + M_t)^{-1}T(P_{s(1,2)}e_1 + P_{s(2,2)}e_2) \\
&\qquad -(M_p + M_t)^{-2}(M_t Q_{z1} T(M_p F_{ts}(e_1) + D_p M_t e_2 - D_t M_p e_2 + K_p M_t e_1))
\end{aligned} \tag{A.16}$$

It is unclear about the nature of the required expression. In terms of norm estimations,

$$\begin{aligned} &||e||P_s||a_1(e)|| \\ &-||e||(P_sA_1A_2^{-1} + P_sB_0R_0^{-1}B_2^TA_2^{-T}Q_zA_2^{-1})||a_2(e)|| \\ &-\tfrac{1}{2}||e||P_sB_0R_0^{-1}B_0^TP_s||e|| \end{aligned} \tag{A.17}$$

By applying equivalent values of $||e||$, $||a_1(e)||$, and $||a_2(e)||$ to our simulation parameters, we can observe the required boundedness by the following graph.

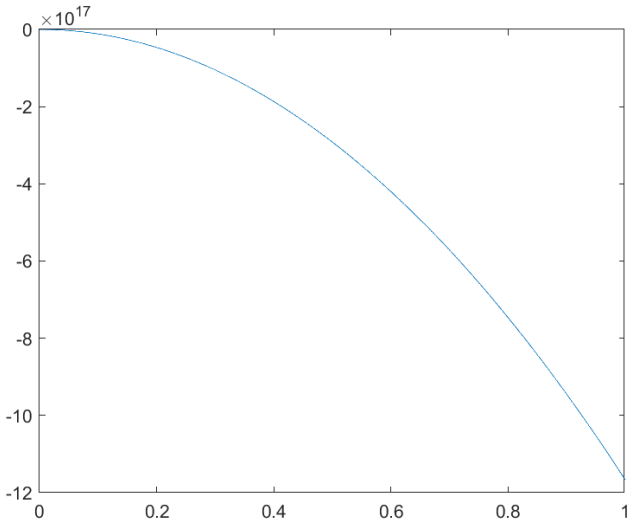

Figure A.6: Simulated plot demonstrating condition $A.4.2$

A.5 Assumption 7.4

A.5.1 $-z_f^T(Q_z + P_f B_2 R^{-1} B_2^T P_f) z_f \leq -\alpha_2 ||z_f||^2$

where $\alpha_2 > 0$:

$$
\begin{aligned}
&-z_f^T(Q_z + P_f B_2 R^{-1} B_2^T P_f) z_f \\
&= -(z + A_{2s}^{-1}(a_2(e) + B_2 u_s))^T (Q_z + P_f B_2 R^{-1} B_2^T P_f)(z + A_{2s}^{-1}(a_2(e) + B_2 u_s)) \\
&= -(z^T + a_2(e)^T A_{2s}^{-T} + u_s^T B_2^T A_{2s}^{-T})(Q_z + P_f B_2 R^{-1} B_2^T P_f)(z + A_{2s}^{-1} a_2(e) + A_{2s}^{-1} B_2 u_s) \\
&= -(z^T + a_2(e)^T A_{2s}^{-T} - s_0(e)^T R_0^{-T} B_2^T A_{2s}^{-T} - \tfrac{1}{2} e^T P_s B_0^T R_0^{-T} B_2^T A_{2s}^{-T}) \\
&\cdot (Q_z + P_f B_2 R^{-1} B_2^T P_f) \\
&\cdot (z + A_{2s}^{-1} a_2(e) - A_{2s}^{-1} B_2 R_0^{-1} s_0(e_s) - \tfrac{1}{2} A_{2s}^{-1} B_2 R_0^{-1} B_0^T P_s e)
\end{aligned}
\tag{A.18}
$$

It is unclear about the nature of the required expression. In terms of norm estimations,

$$
-||z_f|| (Q_z + P_f B_2 R^{-1} B_2^T P_f) ||z_f||, \tag{A.19}
$$

which results in the consideration of

$$
\alpha_2 = (Q_z + P_f B_2 R^{-1} B_2^T P_f). \tag{A.20}
$$

By applying values of and $||z_f||$ to our simulation parameters, we can observe the required boundedness by the following graph.

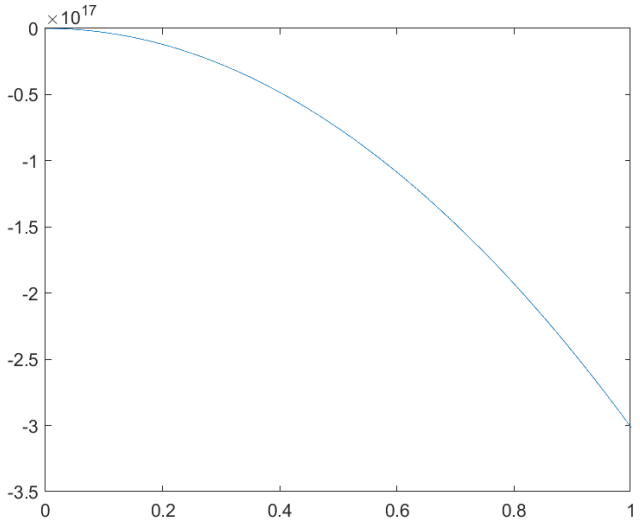

Figure A.7: Simulated plot demonstrating condition $A.5.1$

A.5.2 $||(A_1 - B_1R^{-1}B_2^TP_f)z_f|| \leq b_1||z_f||$ where $b_1 > 0$:

$$\begin{aligned}
&(A_1 - B_1R^{-1}B_2^TP_f)z_f \\
&= (A_1 - B_1R^{-1}B_2^TP_f)(z + A_{2s}^{-1}a_2(e) + A_{2s}^{-1}B_2u_s) \\
&= (A_1 - B_1R^{-1}B_2^TP_f)(z + A_{2s}^{-1}a_2(e) + A_{2s}^{-1}B_2(-R_0^{-1}(s_0(e) + \tfrac{1}{2}B_0^TP_se))) \\
&= (A_1 - B_1R^{-1}B_2^TP_f)(z + A_{2s}^{-1}a_2(e) - A_{2s}^{-1}B_2R_0^{-1}s_0(e) - \tfrac{1}{2}A_{2s}^{-1}B_2R_0^{-1}B_0^TP_se)
\end{aligned} \tag{A.21}$$

It is unclear about the nature of the required expression. In terms of norm estimations,

$$||A_1||z_f||||, \tag{A.22}$$

which results in the consideration of

$$b_1 = ||A_1||. \tag{A.23}$$

By applying values of $||z_f||$ to our simulation parameters, we can observe the required boundedness by the following graph.

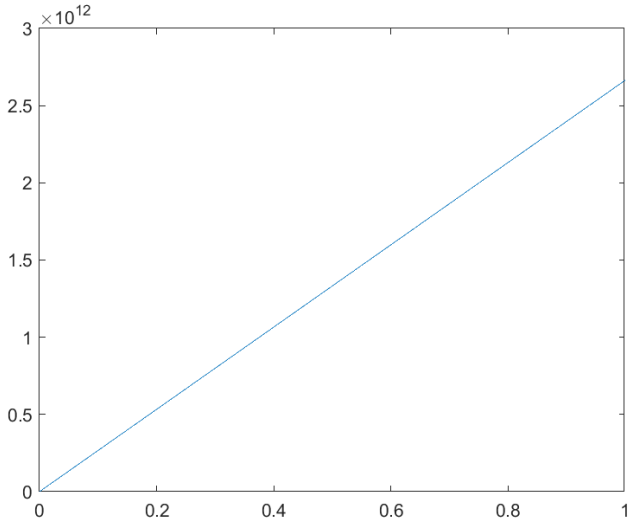

Figure A.8: Simulated plot demonstrating condition $A.5.2$

A.5.3 $||\frac{\partial V_s}{\partial e}(A_1 - B_1R^{-1}B_2^TP_f)z_f|| \leq \beta_1\psi||z_f||$ where $\beta_1 > 0$:

$$
\begin{aligned}
&e^TP_s(A_1 - B_1R^{-1}B_2^TP_f)z_f \\
&= e^TP_s(A_1 - B_1R^{-1}B_2^TP_f)(z + A_{2s}^{-1}a_2(e) + A_{2s}^{-1}B_2u_s) \\
&= e^TP_s(A_1 - B_1R^{-1}B_2^TP_f)(z + A_{2s}^{-1}a_2(e) + A_{2s}^{-1}B_2(-R_0^{-1}(s_0(e) + \tfrac{1}{2}B_0^TP_se))) \\
&= e^TP_s(A_1 - B_1R^{-1}B_2^TP_f)(z + A_{2s}^{-1}a_2(e) - A_{2s}^{-1}B_2R_0^{-1}s_0(e) - \tfrac{1}{2}A_{2s}^{-1}B_2R_0^{-1}B_0^TP_se)
\end{aligned}
\tag{A.24}
$$

It is unclear about the nature of the required expression. In terms of norm estimations,

$$||||e||P_sA_1||z_f||||, \tag{A.25}$$

which results in the consideration of

$$\beta_1 = ||P_sA_1||. \tag{A.26}$$

By applying equivalent values of $||e||$ and $||z_f||$ to our simulation parameters, we can observe the required boundedness by the following graph.

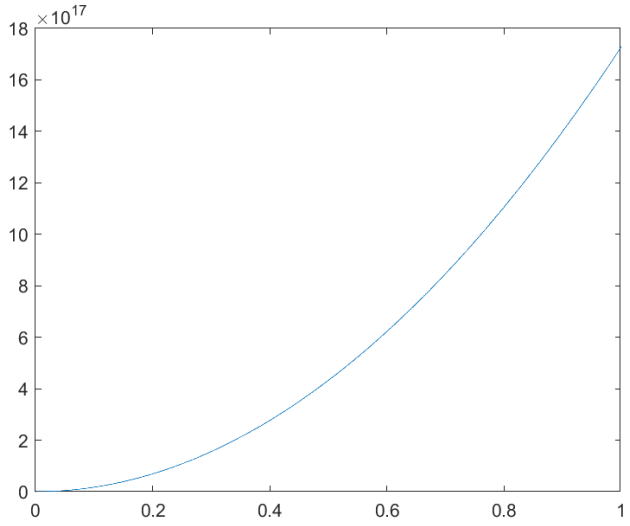

Figure A.9: Simulated plot demonstrating condition $A.5.3$

A.5.4 $||p(e) + s^T(e)z + z^T Q_z z + u_c^T R u_c - p_0(e) - 2s_0^T(e)u_s - u_s^T R_0 u_s|| \leq \delta_1 ||z_f||^2 + \delta_2 \psi ||z_f||$

where $\delta_1 > 0$ **and** $\delta_2 > 0$**:**

By applying norm estimations and equivalent values of $||e||$, $||a_1(e)||$, $||a_2(e)||$, and $||z_f||$ to our simulation parameters, we can observe the required boundedness by the following graph.

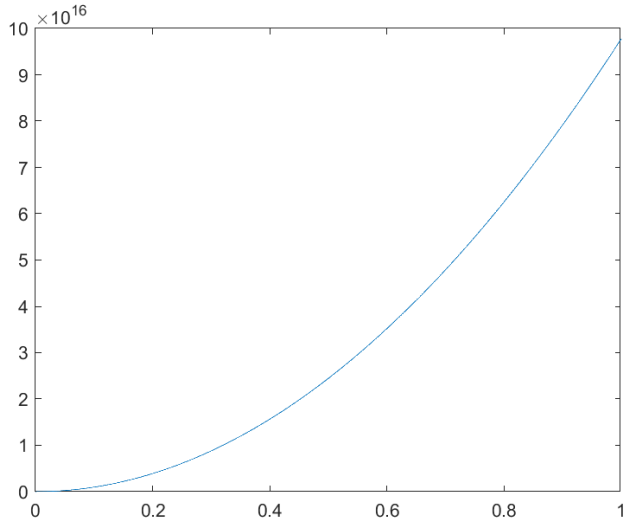

Figure A.10: Simulated plot demonstrating condition $A.5.4$

A.6 $\dot{V}_s < 0$:

$$\dot{V}_s = \frac{\partial V_s}{\partial e_s}\dot{e}_s + \dot{e}_s^T \frac{\partial V_s}{\partial e_s}^T = e_s^T P_s \dot{e}_s + \dot{e}_s^T P_s e_s$$
$$= e^T P_s(a_0(e) + B_0 u_s) + (a_0^T(e) + u_s^T B_0^T) P_s e$$
$$= e^T P_s(a_0(e) + B_0(-R_0^{-1}s_0(e) - \tfrac{1}{2}R_0^{-1}B_0^T P_s e))) + (a_0^T(e) + (-s_0(e)^T R_0^{-T} - \tfrac{1}{2}e^T P_s B_0 R_0^{-T})B_0^T)P_s e$$
$$= e^T P_s a_0(e) - e^T P_s B_0 R_0^{-1} s_0(e) - \tfrac{1}{2}e^T P_s B_0 R_0^{-1} B_0^T P_s e$$
$$+ a_0^T(e) P_s e - s_0(e)^T R_0^{-T} B_0^T P_s e - \tfrac{1}{2}e^T P_s B_0 R_0^{-T} B_0^T P_s e \tag{A.27}$$

By applying norm estimations and equivalent values of $||e||$, $||a_1(e)||$, and $||a_2(e)||$ to our simulation parameters, we can observe the required boundedness by the following graph.

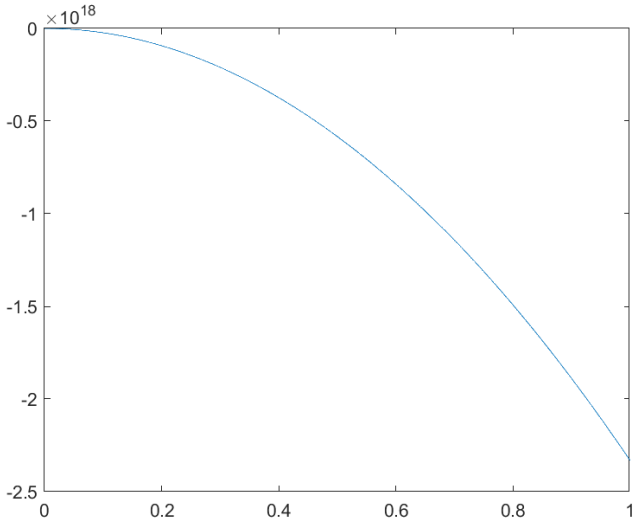

Figure A.11: Simulated plot demonstrating stability of $\dot{V}_s$

Appendix B

Theorem 4.2.2 Verification

Assumption 4.2.1 is verified by applying our simulation parameters into (4.11) as norm estimations for

$$\begin{aligned} &k_1 \tfrac{\partial V_s}{\partial e_s} \tfrac{\partial V_s}{\partial e_s}^T \leq -\tfrac{\partial V_s}{\partial e_s}\bar{a}_0 \leq k_2 \tfrac{\partial V_s}{\partial e_s} \tfrac{\partial V_s}{\partial e_s}^T, \\ &k_3 \bar{a}_0^T \bar{a}_0 \leq -\tfrac{\partial V_s}{\partial e_s}\bar{a}_0 \leq k_4 \bar{a}_0^T \bar{a}_0, \end{aligned} \tag{B.1}$$

$$s_0(e_s) = B_2^T A_{2s}^{-T} Q_z A_{2s}^{-1} a_2(e_s),$$

$$a_0(e_s) = a_1(e_s) - A_1 A_{2s}^{-1} a_2(e_s)$$

$$\begin{aligned} \bar{a}_0(e_s) &= a_0(e_s) - B_0 R_0^{-1}(s_0 + \tfrac{1}{2} B_0^T \tfrac{\partial V_s}{\partial e_s}^T) \\ &= a_1(e_s) - N_1 a_2(e_s) - N_2 e_s \end{aligned}$$

$$\begin{aligned} &k_1 ||e_s|| P_s P_s ||e_s|| \\ &\leq -||e_s|| P_s ||a_1(e_s)|| + ||e_s|| P_s N_1 ||a_2(e_s)|| + ||e_s|| P_s N_2 ||e_s|| \\ &\leq k_2 ||e_s|| P_s P_s ||e_s|| \end{aligned} \tag{B.2}$$

$$\begin{aligned} &k_3(||a_1(e_s)|| - ||a_2(e_s)|| N_1^T - ||e_s|| N_2^T)(||a_1(e_s)|| - N_1||a_2(e_s)|| - N_2||e_s||) \\ &\leq -||e_s|| P_s ||a_1(e_s)|| + ||e_s|| P_s N_1 ||a_2(e_s)|| + ||e_s|| P_s N_2 ||e_s|| \\ &\leq k_4(||a_1(e_s)|| - ||a_2(e_s)|| N_1^T - ||e_s|| N_2^T)(||a_1(e_s)|| - N_1||a_2(e_s)|| - N_2||e_s||) \end{aligned} \tag{B.3}$$

where

$$N_1 = A_1 A_{2s}^{-1} + B_0 R_0^{-1} B_2^T A_{2s}^{-T} Q_z A_{2s}^{-1}; \qquad N_2 = \frac{1}{2} B_0 R_0^{-1} B_0^T P_s.$$

By applying norm estimations and equivalent values of $||e_s||$, $||a_1(e_s)||$, and $||a_2(e_s)||$ to our simulation parameters, we can observe the required boundedness by the following graph.

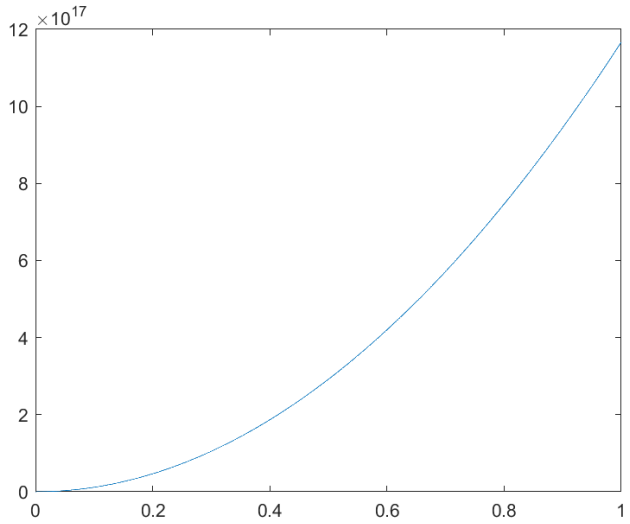

Figure B.1: Simulated plot demonstrating stability of Assumption 4.2.1

Assumption 4.2.2 is verified by applying our simulation parameters into (4.17) for

$$\text{rank} \begin{bmatrix} L_1 & L_2 \end{bmatrix} = 6,$$

where

$$L_1 = \begin{bmatrix} 0 & 2.67 \times 10^3 I & -1.07 \times 10^7 I \\ 2.67 \times 10^3 I & -1.07 \times 10^7 I & -1.33 \times 10^{15} I \end{bmatrix}, \tag{B.4}$$

$$L_2 = \begin{bmatrix} -1.33 \times 10^{15} I & 1.07 \times 10^{19} I & 6.67 \times 10^{26} I \\ 1.07 \times 10^{19} I & 6.67 \times 10^{26} I & -8.00 \times 10^{30} I \end{bmatrix}.$$